

8-2012

Polarization Properties of Maxwell-Gauss Laser Beams

Jessica Patricia Conry
University of Arkansas, Fayetteville

Follow this and additional works at: <http://scholarworks.uark.edu/etd>

 Part of the [Atomic, Molecular and Optical Physics Commons](#), and the [Optics Commons](#)

Recommended Citation

Conry, Jessica Patricia, "Polarization Properties of Maxwell-Gauss Laser Beams" (2012). *Theses and Dissertations*. 491.
<http://scholarworks.uark.edu/etd/491>

This Dissertation is brought to you for free and open access by ScholarWorks@UARK. It has been accepted for inclusion in Theses and Dissertations by an authorized administrator of ScholarWorks@UARK. For more information, please contact scholar@uark.edu, ccmiddle@uark.edu.

POLARIZATION PROPERTIES OF MAXWELL-GAUSS LASER BEAMS

POLARIZATION PROPERTIES OF MAXWELL-GAUSS LASER BEAMS

A dissertation submitted in partial fulfillment
of the requirements for the degree of
Doctor of Philosophy in Physics

By

Jessica P. Conry
Henderson State University
Bachelor of Science in Physics, 2006
University of Arkansas
Master of Science in Physics, 2011

August 2012
University of Arkansas

Abstract

Laser beams are wave-like optical disturbances. They are characterized by a dominant direction of propagation and a finite extent transverse to the direction of propagation. Many characteristics of laser beams can be described in terms of a scalar function multiplied by a constant vector, which can be real (for linear polarization) or complex (for elliptical polarization). The scalar function is a solution to the paraxial scalar wave equation. This scalar description, however, fails to describe the polarization and focusing characteristics of laser beams correctly. For a correct accounting of these characteristics, the electric and magnetic fields associated with laser beams must satisfy not only the wave equation but also the Maxwell's equations. We show that, due to the finite transverse size of laser beams, Maxwell's equations require that the electric field (as well as the magnetic field) associated with laser beams will possess all three nonzero Cartesian components even in free space. Each component can be expressed in terms of the scalar solutions of the paraxial wave equation. We construct three-component solutions giving expressions for the dominant, cross, and longitudinal-polarization components, for linearly polarized Hermite-Gauss and Laguerre-Gauss beams. Such a description correctly accounts for focusing as well as polarization properties of laser beams. We demonstrate the validity of this description experimentally by generating two families of laser beams and verify the existence of cross-polarization field components and their evolution in propagation.

We generate experimental higher-order Hermite-Gauss laser beams intracavity via a pair of crossed fibers. Laguerre-Gauss laser beams were generated by converting Hermite-Gauss beams into Laguerre-Gauss beams of the same order by using a pair of cylindrical lenses to manipulate Guoy's phase of the beams. Intensity profiles of the dominant and cross-polarization components of linearly polarized Hermite-Gauss and Laguerre-Gauss beams are measured and their evolution as the beam propagates away from its focal region was studied. The transverse profiles of the cross-

polarization components of these beams undergo an evolution with propagation. The theoretically expected and experimentally observed intensity profiles are in reasonable agreement confirming the field structure of laser beams derived in this thesis.

This dissertation is approved for
recommendation to the
Graduate Council

Dissertation Director:

Surendra Singh, Ph.D.

Dissertation Committee:

Reeta Vyas, Ph.D.

Min Xiao, Ph.D.

Julia Kennefick, Ph.D.

Hameed Naseem, Ph.D.

Dissertation Duplication Release

I hereby authorize the University of Arkansas Libraries to duplicate this dissertation when needed for research and/or scholarship.

Agreed

Jessica P. Conry

Acknowledgements

Thank you to Dr. Singh for all your advice and guidance through this entire process. Furthermore, thank you to Dr. Vyas for your additional guidance. A special thanks needs to be said for Dr. Gupta and Dr. Salamo for the use of their lasers, I could not have finished with out their use. I would also like to thank my family; Mom, Dad, Jen, Rob, Ethan, Emma, Meagan, Nick, and Missy. You have all been here supporting me through this trial, I love you all. I would also like to thank “Tosh” for being a great friend, crying and eating chocolate cake with me when necessary. Finally, I want to thank Matthew for constantly pulling me out of the black holes and time warps I seem to fall into. I love you very much, here is to forever!

Contents

List of Figures

List of Tables

1	Introduction	1
1.1	Applications	2
1.2	Solution Families	3
1.3	Mode Generation	6
1.3.1	Present Research	6
1.3.2	Other Methods	7
1.4	Longitudinal Field Observation	10
1.4.1	Direct measurement via photoresist	10
1.4.2	Probing	11
1.5	Other polarizations	11
1.6	Experiment	12
2	Paraxial Beam Solutions to Maxwell's Equations	13
2.1	Beam Solutions to Maxwell's Equations	13
2.1.1	Hermite-Gauss solutions of the scalar wave equation	14
2.1.2	Laguerre-Gauss solutions of the scalar wave equation	21
2.1.3	Vector Solutions	28
2.2	Poynting vector	43
2.3	Chapter summary	46

3	Linearly Polarized Hermite-Gauss Laser Beams	47
3.1	Generation of higher-order Hermite-Gauss laser beams	47
3.2	Hermite-Gaussian setup	49
3.3	Hermite-Gauss intensity profiles	55
3.4	Discussion and analysis of results	59
3.4.1	Experimental and theoretical difference analysis (figure of merit)	60
3.4.2	Beam power	63
3.5	Chapter summary	68
4	Linearly Polarized Laguerre-Gauss Laser Beams	69
4.1	Relation between Hermite-Gauss and Laguerre-Gauss beams	69
4.1.1	Mode converter	70
4.2	Experimental arrangement	80
4.2.1	Alignment considerations	82
4.3	Intensity profiles	83
4.4	Results and Discussion	89
4.4.1	Rotation of the cross-polarization profiles	89
4.4.2	Figure of merit of observed intensity profiles	93
4.4.3	Beam growth	93
4.5	Chapter summary	94
5	Conclusions	96
5.1	Summary	96
5.2	Future work	99
	Bibliography	102

A	subtract.m	107
B	figureofmerit.m	111
C	LGrot.m	113

List of Figures

1.1	Example of HG, LG, and IG beams of the same order. From left to right: HG_{02} , LG_{20} , and IG_{20}	5
1.2	Astigmatic mode converter: two appropriately separated identical cylindrical lenses to convert a Hermite-Gaussian mode into a Laguerre-Gaussian mode of the same order.	6
1.3	Variable phase mode converter consisting of two astigmatic mode converters (AMC) and two dove prisms that are rotated to change phase. The astigmatic mode converters consisting of two cylindrical lenses are depicted as cylinders.	8
2.1	Intensity of the fundamental Gaussian beam. The radius $w(z)$ of the spot size of the beam is defined as the distance from the center of the beam to the location where the intensity drops to $1/e^2$ of its maximum value (I_{max}). Here, $r = \sqrt{x^2 + y^2}$. 22	22
2.2	Beam waist and first Rayleigh range locations.	22
2.3	Gouy phase shift and beam shape for a gaussian beam.	27
2.4	Intensity profile for the dominant, cross-polarization, and longitudinal components (left to right) for the fundamental Hermite-Gauss beam.	33
2.5	Evolution of intensity profile for the dominant, cross-polarization, and longitudinal components (top to bottom) for a linearly polarized $HG_{0,2}$ beam at $z = 0$, $z = \frac{1}{2}z_R$, $z = z_R$, and $z = 5z_R$ (left to right).	33
2.6	Evolution of intensity profile for the dominant, cross-polarization, and longitudinal components (top to bottom)for a linearly polarized $HG_{2,0}$ beam at $z = 0$, $z = \frac{1}{2}z_R$, $z = z_R$, and $z = 5z_R$ (left to right).	34
2.7	Evolution of intensity profile for the dominant, cross-polarization, and longitudinal components (top to bottom) for a linearly polarized $HG_{1,1}$ beam at $z = 0$, $z = \frac{1}{2}z_R$, $z = z_R$, and $z = 5z_R$ (left to right).	35
2.8	$\cos \theta(z)$ and $\sin \theta(z)$ verses z/z_R	35
2.9	Intensity profiles for several orders for $z \gg z_R$	36
2.10	Intensity profile for the dominant, cross-polarization, and longitudinal components (left to right) for a linearly polarized fundamental Laguerre-Gauss beam.	42

2.11	Evolution of intensity profile for the dominant, cross-polarization, and longitudinal components (top to bottom) for a linearly polarized LG_{10} beam at $z = 0$, $z = \frac{1}{2}z_R$, $z = z_R$, and $z = 10z_R$ (left to right).	43
2.12	Evolution of intensity profile for the dominant, cross-polarization, and longitudinal components (top to bottom) for a linearly polarized LG_{11} beam at $z = 0$, $z = \frac{1}{2}z_R$, $z = z_R$, and $z = 10z_R$ (left to right)	44
2.13	The energy flow of a Gauss beam near its focus propagating to the right. Line segments represent local trajectories of the Poynting vector, curves perpendicular to them represent the curved wave front.	45
3.1	Intensity distribution and beam profiles for HG_{00} , HG_{10} , and HG_{20} modes in demonstration of higher-order mode generation	48
3.2	Intensity distribution demonstrating HG_{11} generation	48
3.3	Diagram of modified laser cavity	50
3.4	Hermite-Gauss Experimental setup	51
3.5	Modification of the beam waist location and spot size by the output coupler on exit from the laser cavity.	51
3.6	Dominant (I_1) and cross-polarization (I_2) components of the fundamental Gaussian beam (HG_{00}) and HG_{10} at $z = 0$, $z = 0.5z_R$, $z = z_R$, $z = 2z_R$, and $z = 4z_R$.	56
3.7	Dominant (I_1) and cross-polarization (I_2) components of HG_{20} and HG_{11} at $z = 0$, $z = 0.5z_R$, $z = z_R$, $z = 2z_R$, and $z = 4z_R$.	57
3.8	Dominant (I_1) and cross-polarization (I_2) components of HG_{30} and HG_{21} at $z = 0$, $z = 0.5z_R$, $z = z_R$, $z = 2z_R$, and $z = 4z_R$.	58
3.9	Img_s for the fundamental mode at $z = 0$, $z = z_R$, $z = 4z_R$	61
3.10	Experimental (squares) and theoretical (line) beam diameter (number of pixels) with propagation for the dominant-polarization component of a fundamental Gaussian beam	63
3.11	Experimental (squares) and theoretical (line) beam diameter (number of pixels) with propagation for cross-polarization component of a fundamental Gaussian beam	64
3.12	Experimental (squares) and theoretical (line) profile diameter (number of pixels) in the x -direction with propagation for the cross-polarization component of a HG_{20} beam in the x -direction.	64

3.13	Experimental (squares) and theoretical (line) profile diameter (number of pixels) in the y -direction with propagation for the cross-polarization component of a HG_{20} beam.	65
3.14	Beam power after the first polarizer verses the power after the second polarizer for the polarizers parallel to each other.	66
3.15	Beam power after the first polarizer verses the power after the second polarizer for the polarizers perpendicular to each other.	66
3.16	Beam power after the second polarizer with its axis parallel to the first verses the power after the second polarizer with its axis perpendicular to the first.	67
4.1	Beam shape near waist	72
4.2	Pictorial example of the decomposition of the diagonal HG_{02} mode.	72
4.3	Pictorial example of the decomposition of the LG_{02} mode.	72
4.4	Beam shape between the two cylindrical lenses of mode converter	73
4.5	Astigmatic mode converter used in this research for Hermite-Gauss to Laguerre-Gauss mode conversion.	78
4.6	Laguerre-Gauss Experimental setup	80
4.7	Dominant (I_1) and cross-polarization (I_2) intensity profiles for LG beams with $\ell = \pm 1$ and $p = 0$, at $z = 0$, $z = \frac{1}{2}z_R$, $z = z_R$, and $z = 4z_R$. The dominant-polarization intensity profile for $\ell = - \ell $ is the same as the $\ell = + \ell $ profile.	84
4.8	Dominant (I_1) and cross-polarization (I_2) intensity profiles for LG beams with $\ell = \pm 2$ and $p = 0$, at $z = 0$, $z = \frac{1}{2}z_R$, $z = z_R$, and $z = 4z_R$. The dominant-polarization intensity profile for $\ell = - \ell $ is the same as the $\ell = + \ell $ profile.	85
4.9	Dominant (I_1) and cross-polarization (I_2) intensity profiles for LG beams with $(\ell, p) = (0, 1)$, and $(\ell, p) = (\pm 3, 0)$ at $z = 0$, $z = \frac{1}{2}z_R$, $z = z_R$, and $z = 4z_R$. The dominant-polarization intensity profile for $\ell = - \ell $ is the same as the $\ell = + \ell $ profile.	86
4.10	Dominant (I_1) and cross-polarization (I_2) intensity profiles for an LG beam with $\ell = -1$ and $p = 1$, at $z = 0$, $z = \frac{1}{2}z_R$, $z = z_R$, and $z = 4z_R$. The dominant-polarization intensity profile for $\ell = - \ell $ is the same as the $\ell = + \ell $ profile.	87
4.11	Dominant (I_1) and cross-polarization (I_2) intensity profiles for LG with $\ell = \pm 4$ and $p = 0$, at $z = 0$, $z = \frac{1}{2}z_R$, $z = z_R$, and $z = 4z_R$. The dominant-polarization intensity profile for $\ell = - \ell $ is the same as the $\ell = + \ell $ profile.	88

4.12	Define angle of rotation, δ	89
4.13	Angle of rotation, δ , of the cross-polarization component with propagation distance z/z_R . Where $\diamond \equiv LG_{10}$ experiment, $\circ \equiv LG_{20}$ experiment, $\square \equiv LG_{30}$ experiment, $\cdots \equiv LG_{10}$ theory, $- \cdot - \equiv LG_{20}$ theory, and solid line $\equiv LG_{30}$ theory.	91
4.14	Angle of rotation, δ , at $z = z_R$ as a function of l for $p = 0$	92
4.15	Beam size growth with propagation for the cross-polarization component of LG_{10} . The diamonds are experimental results and theoretically expected results are drawn as a continuous curve.	94
4.16	Beam size growth with propagation for the cross-polarization component of LG_{30} . The squares are experimental results and theoretically expected results are drawn as a continuous curve.	95

List of Tables

2.1	Intensity components for a HG_{mn} wave polarized in the x-direction	32
3.1	Figure of merit values for the Hermite-Gauss intensity profiles.	61
4.1	The coefficients $b(n,m,k)$	71
4.2	Values corresponding to Fig. 4.6.	81
4.3	Figure of merit (FM).	93

Chapter 1

Introduction

In the physical science community, the term polarization of light or any other type of electromagnetic radiation refers to the direction of the electric field associated with the electromagnetic radiation. Before the advent of lasers most directed electromagnetic disturbances were modeled in terms of plane waves which, of course, have a definite direction of propagation. For such a field, the direction of the electric field can be specified in terms of constant vectors. This is no longer the case when one is dealing with electromagnetic beams which are electromagnetic disturbances with a finite transverse size. A consequence of this is that the direction of the electric field is not constant in space, similar to the field of a spherical wave. Typically, laser beams are described in terms of a single component electric field that is written as the product of a constant unit vector and a scalar function, which must satisfy the paraxial scalar wave equation. While this description describes many characteristics of laser beams it fails to properly describe their polarization and propagation characteristics. This is true even for linearly polarized laser beams. As will be shown, the result is that there are three nonzero components of the electric field; in addition to the component of the field in direction of (dominant) polarization the field will also have a cross-polarization and longitudinal polarization component.

In the past few decades, special cases of the cross and longitudinal components of the field have been investigated [1–12]. Recently, there has been an increase in interest in the generation and characteristics of different types of laser beams [12–20]. This chapter serves as a brief introduction to this research and present a survey of related work in the field.

1.1 Applications

To fully appreciate the propagation and polarization characteristics of laser beams. Here, a few applications of Gaussian laser beams are discussed. This is by no means a complete list but is meant to illustrate the significance of laser beam propagation and polarization characteristics on their applications.

Particle acceleration

The basic principle behind accelerating particles is the force exerted by the longitudinal electric field component possessed by polarized laser beams [1]. This field, as we will show in the following chapter, depends inversely on the spot size of the beam. Therefore, the more tightly focused the beam, the stronger the longitudinal component [21–25]. A lens wave guide setup is suggested by Scully [26] and Scully and Zubairy [24] that would create a sufficiently intense longitudinal electric field to accelerate a beam of charged particles. Proof of principle for this type of laser linear accelerator is reported by Bochove et. al. using a asymmetric radially polarized Hermite-Gaussian laser beam [27]. This type of laser linear accelerator injects a beam of electrons in the laser beam leading to an increase in energy on the order of GeV/m [28].

Bahari and Shahriari report charged particle acceleration using a similar method by using two orthogonal Hermite-Gaussian modes [29]. They suggest that, unlike the conclusion reached by Scully and Zubairy [24], the change in energy of the accelerated electrons does not depend linearly on the radius of the beam but there is an ideal beam size for electron acceleration. They calculated optimal laser beam parameters, including polarization, beam radius, and intensity, for laser linear accelerators.

Orbital angular momentum

As first suggested in 1909 by Poynting [30] and demonstrated by Beth [31], nearly thirty years later, laser beams that are circularly polarized have $\pm\hbar$ spin angular momentum per photon for left or right circular polarization, respectively. Laguerre-Gaussian beams possess an interesting property that Hermite-Gaussian beams do not: each photon in a LG beam carries $l\hbar$ orbital angular momentum (OAM) and therefore $(l \pm 1)\hbar$ total angular momentum for a circularly polarized beam [16, 32–34]. It is important to note here that even a *linearly* polarized LG beam can carry orbital angular momentum [32].

Not only is the study of the orbital angular momentum possessed by light, in itself, fundamentally interesting but OAM is the basis for many other applications. For example, more information can be carried by a beam with orbital angular momentum per than by the spin of the beam alone [35]. Thus being able to control OAM could lead to better optical communication methods [36–38]. Additionally, a better understanding leads to improvement of microscopic particle manipulation methods, such in optical tweezers [39–44].

1.2 Solution Families

Laser beams can be modeled by the paraxial wave equation (PWE). In Chapter 2 we examine two complete sets of solutions to the PWE. The most common coordinate systems used to construct beam like solutions to the PWE are Cartesian and circular cylindrical, which give the Hermite-Gaussian (HG) and Laguerre-Gaussian families of beam solutions, respectively. Both families of solutions have been studied comprehensively [17–20] and they are of practical importance since lasers tend to operate in these modes due to the fact that corresponding symmetries are realized in of stable cavities [45, 46].

For several years HG and LG beams were the only known sets of solutions to the wave equa-

tion. Recently, there has been an upsurge of interest in other stable beam solutions. Several new solutions have been theoretically proposed and experimentally observed. These include: Hermite-Laguerre-Gaussian beams [47, 48], Spiral beams [49, 50], Airy-Gaussian beams [51, 52], and Hypergeometric beams [53]. Another, particularly interesting family of complete solutions to the PWE, the one with elliptical symmetry, is known as Ince-Gaussian (IG) beams [43, 54, 55]. IG beams are the continuous “connection” between HG and LG beams [54]. Like the Hermite and Laguerre-Gaussian families of solutions, the Ince-Gaussian family forms a complete set of solutions with elliptic symmetry and are eigenmodes of stable resonators (i.e. are natural resonating modes of stable resonators) [54, 55].

While the Hermite and Laguerre-Gaussian solutions are discussed in detail in the following chapters Ince-Gaussian beams are discussed only here. At this time, little is known about Ince polynomials and, according to Bandres et. al. [54], have not received the attention that they deserve. A particularly interesting property of IG beams is that they represent a continuous set of modes between Hermite and Laguerre-Gaussian beams. HG and LG beams are special extreme cases of IG beams [54]. The IG beam solution is similar to that of HG and LG beams (see Chapter 2 sections 1.1 and 1.2), save that the Hermite and Laguerre polynomials are replaced by Ince polynomials. The radius of curvature of the wave front is the same for IG beams as that of a fundamental Gaussian beam. Therefore, the propagation of IG beams through optical elements can be described in terms of the well know ABCD matrix formalization [45, 54]. Additionally, the beam diameter depends on propagation distance and the magnitude of the intensity varies in the same way as the intensity of a fundamental Gaussian beam.

Schwarz et. al were the first to report experimental generation of Ince-Gaussian beams in a stable resonating cavity [56]. They report that by breaking the symmetry of a solid state, diode pumped laser, high order IG beams with high quality can be produced. By using two different output couplers with differing radii of curvature, adjusting the pump power, and changing the symmetry by translating the output coupler, different orders and degrees of IG beams are produced. Additional

cavity modifications, such as crossed fibers in the cavity can be introduced to change the output mode [43, 56, 57].

Ince-Gaussian beams can also be generated using a pair of carefully aligned and specifically placed cylindrical lenses [43]. This pair of cylindrical lenses is known as an astigmatic mode converter (AMC) which will be discussed in Chapter 2 in detail. The number of hyperbolic and nodal lines (or, in this case, the order of a HG mode) will be determined by the degree of alignment of the laser cavity and or with the use of a pair of crossed fibers inside the cavity, forcing non-fundamental mode operation. The structure of the corresponding mode changes as the angle between the mode axis and the mode converter changes, altering the ellipticity of the mode [43].

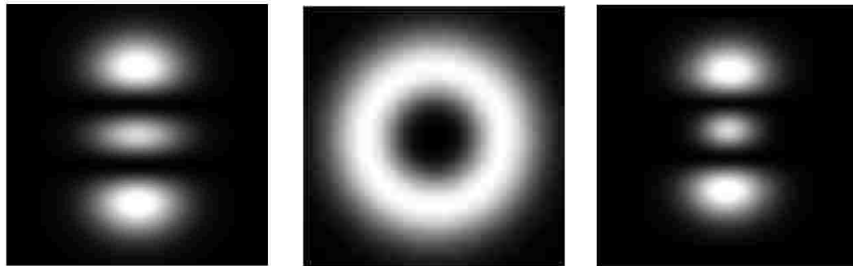


Figure 1.1: Example of HG, LG, and IG beams of the same order. From left to right: HG_{02} , LG_{20} , and IG_{20} .

Figure 1.1 gives an example of second order HG, LG, and IG beams. If the HG beam, depicted on the far left, was sent through an AMC with its axis parallel to the mode converter axis the output of the AMC would be the same HG beam. If the same beam was sent through the mode converter with its axis 45° to the AMC the output would be the LG mode given in the middle. On the other hand, if the beam was sent into the mode converter with its axis at a small angle to the mode converter axis then the output would be similar to the IG beam given on the right.

1.3 Mode Generation

1.3.1 Present Research

Chapters 3 and 4 discuss how HG and LG beams are generated for this study. For this research we chose to generate Hermite-Gaussian beams by inserting a pair of crossed fibers in the laser cavity [15]. There are other ways to generate these beams. This method was chosen due to its effectiveness and simplicity. Additionally, the crossed fibers method did not require acquisition of any new equipment. Laguerre-Gaussian modes are generated by sending the HG modes generated from the laser through an astigmatic mode converter [32]. This type of mode converter consists of two cylindrical lenses and two spherical lenses, with proper alignment and separation the mode converter will convert a Hermite-Gaussian beam into a Laguerre-Gaussian beam of the same order. Figure 1.2 depicts this type of mode converter. This method of generation for LG beams was chosen because the components of the converter were readily available and the high purity of modes that can be generated. The quality of mode generated by the astigmatic mode converter is limited by the quality of the input HG beam [58] and proper alignment and placement of the mode converter.

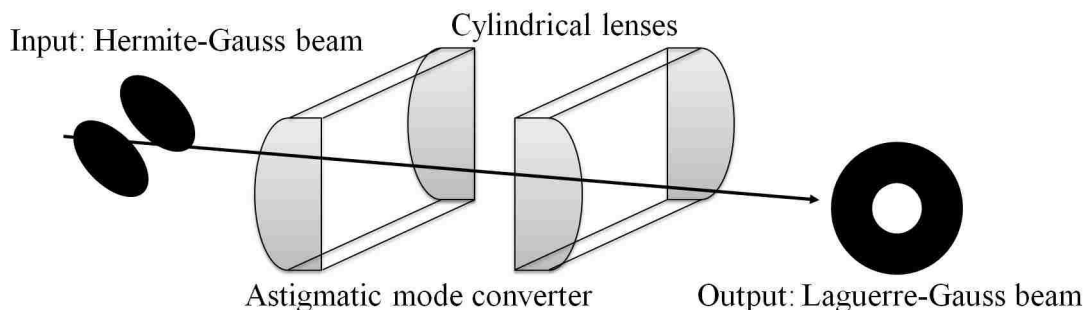


Figure 1.2: Astigmatic mode converter: two appropriately separated identical cylindrical lenses to convert a Hermite-Gaussian mode into a Laguerre-Gaussian mode of the same order.

1.3.2 Other Methods

While the present investigation uses the above mentioned methods for higher-order Hermite-Gaussian and Laguerre-Gaussian mode generation, there are other notable methods that will be mentioned in this section.

Generalization of an astigmatic mode converter: variable phase mode converter

O’Neil and Courtial advocate that the cylindrical lens mode converter briefly described above is a specific arrangement of the general variable phase mode converter (VPMC) [59]. The basis of the VPMC is the matrix formulation given by Allen et. al. [60], which describes phase and intensity structure of Laguerre-Gaussian beams as they propagate through an optical system, with Hermite-Gaussian modes as the basis set of orthogonal modes. Allen draws a parallel between how a waveplate treats polarized light and a mode converter converts between mode families: a waveplate introduces a phase shift between two orthogonally polarized light beams and a mode converter introduces a phase shift between orthogonal modes. O’Neil and Courtial generalize Allen’s matrix formulation and additionally write a matrix describing Hermite-Gaussian modes with Laguerre-Gaussian modes as the basis set of orthogonal modes. Analyzing the two formulations (one with HG basis and the other with LG basis) a connection was found between rotation in one set and mode conversion in the other. This connection forms the operating basis of the VPMC. The VPMC consists of two sets of astigmatic mode converters rotated at 90° and two dove prisms (that are rotated to change phase) between the two sets of converters that serve as an image rotator (Fig. 1.3 A) [59]. In addition to the analogy between this mode converter and polarizers that leads to a very intuitive connection between HG and LG modes another advantage, in some applications, in using such a mode converter is that the pattern of conversion is repeated every 180° of rotation of the mode converter (as opposed to every 90° for the astigmatic mode converter).

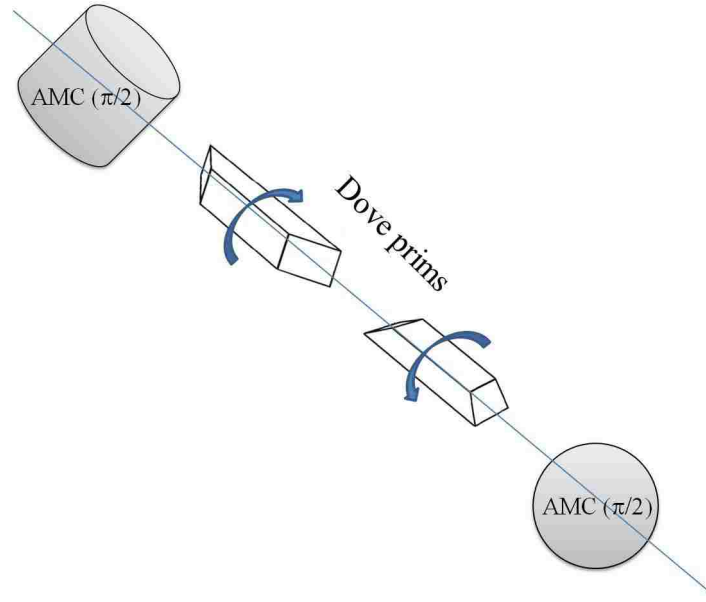


Figure 1.3: Variable phase mode converter consisting of two astigmatic mode converters (AMC) and two dove prisms that are rotated to change phase. The astigmatic mode converters consisting of two cylindrical lenses are depicted as cylinders.

Laguerre-Gaussian modes via holograms

Laguerre-Gaussian beams, of theoretically any order, can also be generated using a hologram. The pattern on the holographic plate is an interference pattern of the mode that is desired and a reference field which is the output of the laser that is to be used to generate the LG beam [61, 62]. There are two general methods for generating Laguerre-Gaussian beams holographically, one dynamic and the other static. The static method involves printing the computer generated interference pattern on a transparency. A reference Gaussian beam is sent through the hologram generating the desired Laguerre-Gaussian beam. The dynamic system uses liquid crystals to display a cross section of the phase pattern of the desired LG mode on silicon (LCOS) [63, 64]. The liquid crystals can be electrically manipulated allowing dynamic control of the mode to be generated. LCOS also has the advantage of being able to actively correct phase distortions leading to a higher quality beam [63].

The Laguerre-Gaussian modes generated via holograms are typically of significantly lower purity than those generated from an astigmatic mode converter or the dynamic method [65]. On the

other hand, to convert a higher order Hermite-Gaussian beam to Laguerre-Gaussian beam with a astigmatic mode converter it is necessary to be able to generate the Hermite-Gaussian beam of the desired order. Generally, it is desired to have a laser beam operating in only the fundamental mode. Thus, lasers are typically designed so that they are forced to operate in the fundamental mode, making it difficult or impossible to force the laser to operate in a higher order mode, making the holography scheme advantageous in such situations.

Spot-defect mirror Laguerre-Gaussian mode generation

The previously discussed methods for Laguerre-Gaussian beam generation all have one thing in common and that could be considered a disadvantage in generating high quality beams, they are all extra-cavity methods. An innovative, and beautifully simple, intracavity method is presented by Ito et. al. [66]. They suppress the operation of lower order modes by replacing the high-reflectivity mirror at the rear of the cavity with one that has a low reflectivity spot defect. A defect on the mirror can be achieved by focusing a high intensity laser pulse at the center of a typical high-reflectivity dielectric mirror. Using a laser to create the spot defect allows for controlled size of the spot. While an aperture can be used inside the laser cavity to suppress higher order modes from oscillating, the spot defect on the mirror works in the opposite manner. The operating principle is rather straight forward, the losses induced by the low reflectivity spot forces the laser to operate in a higher-order Laguerre-Gaussian mode, similar to the cross-fiber method used to generate higher-order Hermite-Gaussian modes. This method can only be used to generate beams with a radial index of zero ($p = 0$), the radial index dictates the number of rings the beam possesses, where the number of rings is $p + 1$. Also, since this method generates standing waves in the azimuthal direction, the LG $+\ell$ and LG $-\ell$ will be generated at the same time. Therefore, the output of the laser will be an interference pattern of the two modes.

The length of the laser cavity and the radii of curvature of the cavity mirrors determine the beam diameter. With increase in order of the beam there is an increase of the relative size of the null in

the center of the beam. Ito et. al. [66] report changing the length of the cavity, keeping the defect on the mirror the same size, to change the ratio of the spot defect to beam radius for mode selection. Kano et. al. [67] describe another approach to change the spot defect size to beam diameter ratio, change the defect spot size, the larger the defect size the higher the order of the mode generated.

1.4 Longitudinal Field Observation

Apart from the aforementioned particle acceleration there are other uses for the longitudinal field component of a laser beam such as single molecule orientation determination [68]. It has been suggested that the direction of the field could also be of use in near-field optical microscopy [69]. The observation of the longitudinal field is beyond the scope of this research. It is, however, a well researched and interesting topic. This section gives a few examples of methods used to observe the longitudinal field.

1.4.1 Direct measurement via photoresist

Hao and Leger report a method to directly measure the longitudinal component of radially polarized beams by recording the profiles in photoresist [70]. A silica substrate was coated with photoresist and placed in the focal plane of a microscope objective, the location of the focus of the beam. This method takes advantage of the fascinating characteristic that a very tightly focused, radially polarized beam's longitudinal component can have a larger intensity than its transverse component [70]. After exposing the photoresist to the beam, the photoresist is developed and the depth of the photoresist is measured. The depth is directly proportional to the intensity of the beam, the profile of the longitudinal component can thus be directly observed.

The method used by Hao and Leger is convenient because the longitudinal component can be measured in a straight forward way but it has disadvantages. First, there is a high cost associated

with acquiring the profiles, the mask required for the photoresist deposition requires electron-beam mask fabrication techniques. Second, since the longitudinal component is only going to be appreciable if the beam is tightly focused, the area recorded in the photoresist will be very small (on the order of the wavelength of the light used) so it is necessary to use something such as an Atomic Force Microscope to measure the surface profile.

1.4.2 Probing

Another arrangement for longitudinal field observation is presented by Novonty et. al. [71], they verify theoretical profiles for the longitudinal-polarization component of a radially polarized Laguerre-Gaussian beam by using a fluorescing molecule as a probe. Single molecules with known dipole orientation are scanned through the focus of the laser. Fluorescence rate of the molecule and laser location data is compiled to generate an image of the field.

Bouhelier et. al. [69] report using the tip of near field optical microscope to scan the longitudinal field. This method scans the focus of the field with a metallic or dielectric tip which scatters the electric field. The field profile can be determined by recording the scattering field as function of the tip position.

1.5 Other polarizations

While this thesis focuses on linearly polarized Hermite and Laguerre-Gaussian beams, it is worth noting here that for other types of polarization, Maxwell's equations will also require three non-zero field components. For example, a right circularly polarized beam will have a small longitudinal component and a smaller left circular polarization component [72]. The experimental arrangement required to generate a circularly polarized beam consists of sending a linearly polarized beam through a quarter wave plate. To observe the cross-polarization component of a circularly

polarized beam would then require another quarter wave plate. The addition of the second quarter wave plate to the already circularly polarized beam is the same as introducing a half wave plate to a linearly polarized beam, i.e. it will simply rotate the linear polarization. The result is that the setup to experimentally observe the cross-polarization component of a circularly polarized beam reproduces the setup used here to generate the cross-polarization profiles of a linearly polarized beam [14]. For beams that are radially and azimuthally polarized the longitudinal and cross polarization components will be more significant when beams do not have circular symmetry about direction of propagation [21, 70, 72].

1.6 Experiment

Chapter 3 describes Hermite-Gaussian laser beams. We compare experimental and theoretical transverse HG intensity profiles for several orders of modes and demonstrate the change in their shape with propagation. Laguerre-Gaussian beams are discussed in Chapter 4 along the same lines as described for HG beams in Chapter 3. Additionally, the rotation of the cross-polarization components of the LG beams is quantitatively verified.

In the final chapter, conclusions and recommendation for further research are given. Included in the appendix are the Maple work sheet used to generate the theoretical transverse intensity profiles and the MATLAB programs used to compare theoretical and experimental profiles and to analyze the rotation of the cross-polarization components of the Laguerre-Gauss beams.

Chapter 2

Paraxial Beam Solutions to Maxwell's Equations

This chapter begins with a discussion of the solutions to the wave equation and the failure of the typically used scalar paraxial wave approximation in describing the polarization and focusing of laser beams. For linearly polarized beams it is typically assumed that the electric field can be written as a constant vector (possibly complex) multiplied by a scalar function. Therefore, only one component to the electric field is necessary. We will show that there must be three nonzero components to the electric field, leading to vector solutions. Solutions to Maxwell's equations in Cartesian and circular cylindrical coordinates, which give rise to the Hermite-Gauss and Laguerre-Gauss beams, respectively, are then discussed. The discussion of an astigmatic mode converter capable of converting Hermite-Gauss beam into a Laguerre-Gauss beam of the same order can be found in Chapter 3.

2.1 Beam Solutions to Maxwell's Equations

Since laser beams are electromagnetic radiation, we naturally start this section with Maxwell's equations in free space:

$$\vec{\nabla} \cdot \vec{E} = 0, \quad (2.1)$$

$$\vec{\nabla} \times \vec{E} = -\frac{\partial \vec{B}}{\partial t}, \quad (2.2)$$

$$\vec{\nabla} \cdot \vec{B} = 0, \quad (2.3)$$

$$\vec{\nabla} \times \vec{B} = \mu_0 \epsilon_0 \frac{\partial \vec{E}}{\partial t}, \quad (2.4)$$

where \vec{E} and \vec{B} are the electric field and magnetic field, respectively. μ_0 and ε_0 are the permeability and permittivity of free space. On taking the curl of Eq. (2.2) we get:

$$\vec{\nabla} \times (\vec{\nabla} \times \vec{E}) = -\frac{\partial}{\partial t} (\vec{\nabla} \times \vec{B}). \quad (2.5)$$

Combining Eq. (2.5) with Eq. (2.4), using the vector identity

$$\vec{\nabla} \times (\vec{\nabla} \times \vec{E}) = \vec{\nabla} (\vec{\nabla} \cdot \vec{E}) - \nabla^2 \vec{E},$$

and Eqs. (2.1) and (2.4) to eliminate $\vec{\nabla} \times \vec{B}$ we find that the equation satisfied by the field is

$$\left[\nabla^2 - \mu_0 \varepsilon_0 \frac{\partial^2}{\partial t^2} \right] \vec{E} = 0. \quad (2.6)$$

Equation (2.6) is known as the *wave equation*. Following the same method we find the same equation for the magnetic field,

$$\left[\nabla^2 - \mu_0 \varepsilon_0 \frac{\partial^2}{\partial t^2} \right] \vec{B} = 0. \quad (2.7)$$

Note that each cartesian component of the electric and magnetic fields satisfies Eqs. (2.6) and (2.7), respectively.

2.1.1 Hermite-Gauss solutions of the scalar wave equation

In many situations it is assumed that there is only one nonzero Cartesian component of the electric field (polarization direction). In this section we will consider solutions in cartesian coordinates. Assuming only one nonzero Cartesian field component, Eq. (2.6) reduces to the *scalar wave equation*,

$$\left[\nabla^2 - \frac{1}{c^2} \frac{\partial^2}{\partial t^2} \right] \psi(\vec{r}, t) = 0, \quad (2.8)$$

where $\psi(\vec{r}, t)$ represents a cartesian component of the field amplitude and

$$c = \frac{1}{\sqrt{\mu_0 \varepsilon_0}} \quad (2.9)$$

is the speed of light in vacuum. Assuming quasimonochromatic waves of angular frequency ω , propagating in the z direction, we seek a solution with a finite transverse extent,

$$\psi(\vec{r}, t) = \psi(\vec{r})e^{i(kz - \omega t)}, \quad (2.10)$$

where $k = \frac{\omega}{c} = \frac{2\pi}{\lambda}$ is the magnitude of the wave vector and λ is the wavelength. The $\psi(\vec{r})$ term describes the transverse variation in the wave amplitude. Since we are in search of a solution with a slow change in the transverse profile $\psi(\vec{r})$ over a few wavelengths we look for fields that satisfy,

$$\frac{1}{k} \left| \frac{\partial \psi(\vec{r})}{\partial z} \right| = \frac{\lambda}{2\pi} \left| \frac{\partial \psi(\vec{r})}{\partial z} \right| \ll |\psi(\vec{r})| \quad (2.11)$$

and

$$\frac{1}{k} \left| \frac{\partial}{\partial z} \left(\frac{\partial \psi(\vec{r})}{\partial z} \right) \right| = \frac{\lambda}{2\pi} \left| \frac{\partial}{\partial z} \left(\frac{\partial \psi(\vec{r})}{\partial z} \right) \right| \ll \left| \frac{\partial \psi(\vec{r})}{\partial z} \right|. \quad (2.12)$$

These equations state what is known as the paraxial approximation. Substituting Eq. (2.10) into Eq. (2.8) gives,

$$\begin{aligned} \left[\nabla^2 - \frac{1}{c^2} \frac{\partial^2}{\partial t^2} \right] \psi(\vec{r}, t) &= \left[\frac{\partial^2}{\partial x^2} + \frac{\partial^2}{\partial y^2} + \frac{\partial^2}{\partial z^2} - \frac{1}{c^2} \frac{\partial^2}{\partial t^2} \right] \psi(\vec{r})e^{i(kz - \omega t)} \\ &= \left[\frac{\partial^2}{\partial x^2} + \frac{\partial^2}{\partial y^2} \right] \psi(\vec{r})e^{i(kz - \omega t)} + \frac{\partial}{\partial z} \left(\frac{\partial \psi(\vec{r})}{\partial z} e^{i(kz - \omega t)} + ik\psi(\vec{r})e^{i(kz - \omega t)} \right) \\ &\quad + \frac{\omega^2}{c^2} \psi(\vec{r})e^{i(kz - \omega t)} \\ &= \left[\frac{\partial^2}{\partial x^2} + \frac{\partial^2}{\partial y^2} \right] \psi(\vec{r})e^{i(kz - \omega t)} + \frac{\partial^2 \psi(\vec{r})}{\partial z^2} e^{i(kz - \omega t)} \\ &\quad + 2ik \frac{\partial \psi(\vec{r})}{\partial z} e^{i(kz - \omega t)} + (ik)^2 \psi(\vec{r})e^{i(kz - \omega t)} + k^2 \psi(\vec{r})e^{i(kz - \omega t)}, \end{aligned}$$

where $\omega^2/c^2 = k^2$ is used. Dropping the second order derivative with respect to z , in accordance with Eq. (2.12), and simplifying we arrive at the *scalar paraxial wave equation*,

$$\left[\frac{\partial^2 \psi(\vec{r})}{\partial x^2} + \frac{\partial^2 \psi(\vec{r})}{\partial y^2} + 2ik \frac{\partial \psi(\vec{r})}{\partial z} \right] = 0. \quad (2.13)$$

The well known solutions in cartesian coordinates to Eq. (2.13) can be realized via separation of variables by assuming a solution as a product of two functions depending on x and z and y and z , respectively [12,45]

$$\psi_{mn}(x, y, z) = \psi_m(x, z) \times \psi_n(y, z). \quad (2.14)$$

We can then write the paraxial wave equation as,

$$\left[\frac{\partial^2 \psi_m(x, z)}{\partial x^2} + 2ik \frac{\partial \psi_m(x, z)}{\partial z} \right] + \left[\frac{\partial^2 \psi_m(y, z)}{\partial y^2} + 2ik \frac{\partial \psi_m(y, z)}{\partial z} \right] = 0. \quad (2.15)$$

Since the x, z and y, z parts of Eq. (2.15) must independently equal zero we can find the solution in one transverse direction and then use it to find the solution in the other coordinate. Focusing only on the x, z dependent solutions we can write the paraxial wave equation as

$$\left[\frac{\partial^2 \psi_m(x, z)}{\partial x^2} + 2ik \frac{\partial \psi_m(x, z)}{\partial z} \right] = 0. \quad (2.16)$$

Since we seek a wave-like solution that will describe laser beams which have a definite direction of propagation and a finite transverse area we assume a general solution of the form [46]

$$\psi_m = h_m \left(\frac{x\sqrt{2}}{w(z)} \right) \cdot e^{i \left(k \frac{x^2}{2q(z)} + P(z) \right)}, \quad (2.17)$$

where h_m , $q(z)$, $w(z)$, and $P(z)$ are to be determined. $w(z)$ is a z dependent function that will be shown to be related to beam size and q is a complex function that will be referred to as the complex

beam parameter. Inserting Eq. (2.16) into Eq. (2.17) yields,

$$\begin{aligned} & \left[\frac{\partial^2 \psi_m(x, z)}{\partial x^2} + 2ik \frac{\partial \psi_m(x, z)}{\partial z} \right] \\ &= \left\{ \frac{2}{w^2(z)} h_m'' + \left[\frac{i2kx\sqrt{2}w(z)}{q(z)} - \frac{2ikx\sqrt{2}}{q^2(z)} \frac{dw(z)}{dz} \right] h_m' + \left[\frac{ik}{q(z)} - 2ki \frac{dP(z)}{dz} \right] h_m \right\} e^{i\left(k\frac{x^2}{2q(z)} + P(z)\right)} \\ &= 0, \end{aligned} \quad (2.18)$$

where the argument of h_m is suppressed for simplicity and we have imposed the requirement

$$\frac{dq}{dz} = 1. \quad (2.19)$$

A single prime on h_m is used to denote a first order derivative with respect to its argument and a double prime to represent a second order derivative with respect to its argument:

$$h_m'(X) = \frac{dh_m(X)}{dX}, \quad (2.20)$$

$$h_m''(X) = \frac{d^2h_m(X)}{dX^2}. \quad (2.21)$$

where

$$X = \frac{x\sqrt{2}}{w(z)}.$$

Upon simplifying the left hand side of Eq. (2.18) we are left with the following differential equation

$$h_m'' + ik \left[\frac{1}{q(z)} - \frac{1}{q^2(z)} \frac{d}{dz} w(z) \right] \frac{\sqrt{2}x}{w(z)} h_m' + \left[\frac{ikw^2(z)}{2q(z)} - kw^2(z) i \frac{dP(z)}{dz} \right] h_m = 0, \quad (2.22)$$

If we choose w and P to satisfy

$$\frac{ikw^2(z)}{2q(z)} - kw^2(z) \frac{dP(z)}{dz} = m \quad (2.23)$$

and

$$\frac{ik}{q(z)} - \frac{1}{q^2(z)} \frac{d}{dz} w(z) = -2, \quad (2.24)$$

Eq. (2.22) becomes:

$$\frac{d^2 h_m(x)}{dx^2} - 2x \frac{dh_m(x)}{dx} + mh_m(x) = 0. \quad (2.25)$$

Equation(2.25) has the form of the Hermite differential equation [73]. This approach then leads to what is often called the *standard Hermite equation* [45]. The function h_m is therefore a Hermite polynomial, H_m . The Hermite polynomial is given by

$$H_m(\mu) = (-1)^m e^{\mu^2} \frac{d^m}{d\mu^m} e^{-\mu^2}. \quad (2.26)$$

A few lower order Hermite polynomials are as follows:

$$H_0(\mu) = 1 \quad (2.27)$$

$$H_1(\mu) = 2\mu \quad (2.28)$$

$$H_2(\mu) = 4\mu^2 - 2 \quad (2.29)$$

$$H_3(\mu) = 8\mu^3 - 12\mu \quad (2.30)$$

$$H_4(\mu) = 16\mu^4 - 48\mu^2 + 12 \quad (2.31)$$

$$H_5(\mu) = 32\mu^5 - 160\mu^3 + 120\mu \quad (2.32)$$

$$(2.33)$$

$P(z)$ must be found so that Eqs. (2.23) and (2.24) are satisfied. Since we required $dq/dz = 1$, q is given by

$$q(z) = q_0 + z, \quad (2.34)$$

where $q_0 = q(0)$. With expectation of q being complex we will write

$$q(z) = z - iz_R, \quad (2.35)$$

where z_R is to be found. Writing q as the denominator of a fraction, as it is in the exponent of Eq. (2.17), we have

$$\frac{1}{q(z)} = \frac{1}{z + \frac{z_R^2}{z}} + \frac{i}{\frac{z^2}{z_R} + z_R}. \quad (2.36)$$

If we introduce the notation

$$R(z) = z + z_R^2/z, \quad (2.37)$$

and

$$w(z) = w_0 \sqrt{1 + (z/z_R)^2}, \quad (2.38)$$

where we write

$$w_0 = \sqrt{\frac{\lambda z_R}{\pi}}, \quad (2.39)$$

we can then rewrite Eq. (2.36) in terms of two the real parameters, w and R as

$$\frac{1}{q(z)} = \frac{1}{R(z)} + \frac{2i}{kw^2(z)}. \quad (2.40)$$

The physical significance of $w(z)$ and $R(z)$ will be discussed after the final solution for the wave is found.

Next, the function $P(z)$ is to be found. Substitute Eqs. (2.38) and (2.40) in Eq. (2.23):

$$\begin{aligned} \frac{dP(z)}{dz} &= i \frac{m}{kw^2(z)} + \frac{1}{2q(z)} \\ &= \frac{im}{kw_0^2 (1 + z^2/z_R^2)} + \frac{1}{2(z - z_R)} \\ &= \frac{imz_R}{2(z_R^2 + z^2)} + \frac{z + iz_R}{2(z_R^2 + z^2)} \\ &= \frac{(m+1)z_R}{2(z_R^2 + z^2)} + \frac{z}{2(z_R^2 + z^2)} \end{aligned} \quad (2.41)$$

Upon integration of Eq. (2.41), from 0 to z , an expression for $P(z)$ is found,

$$P(z) = i \frac{m+1}{2} \arctan\left(\frac{z}{z_R}\right) + \frac{1}{4} \ln\left[1 + \frac{z^2}{z_R^2}\right]. \quad (2.42)$$

To understand the significance of $P(z)$ first consider the exponential of the real part of $P(z)$:

$$e^{\Re[P(z)]} = \exp\left[\frac{1}{4} \ln\left(1 + \left(\frac{z}{z_R}\right)^2\right)\right] = \sqrt{\frac{w_0}{w(z)}}. \quad (2.43)$$

As can be seen from Eq. (2.43) the real part gives an amplitude factor that leads to a decrease in intensity with propagation distance z . Let

$$\theta(z) = \arctan\left(\frac{z}{z_R}\right), \quad (2.44)$$

then the imaginary part of $P(z)$ can be written as

$$\Im[P(z)] = \frac{(m+1)}{2} \theta(z). \quad (2.45)$$

Examining the exponential of the imaginary part of $P(z)$ it can be seen that it gives a phase shift, θ , which is called the *Gouy phase* and will be discussed in more detail in the following section.

Substituting Eqs. (2.40) and (2.42) into Eq. (2.17), the x, z dependent part of a solution to the paraxial wave equation is found:

$$\psi_m(x) = \left(\frac{w_0}{w(z)}\right)^{1/2} H_m\left(\frac{x\sqrt{2}}{w(z)}\right) \cdot e^{(ik\frac{x^2}{2q(z)}) + i(m+1)\theta(z)/2}, \quad (2.46)$$

where A_m is dependent on the total power of the beam and is found in section 1.2. With a similar solution for $\psi(y, z)$, the product of $\psi(x, z)$ and $\psi(y, z)$ gives the well known Hermite-Gaussian

beam solution:

$$\psi_{mn}(\vec{r}) = \frac{w_0}{w(z)} H_m \left(\frac{\sqrt{2}x}{w(z)} \right) H_n \left(\frac{\sqrt{2}y}{w(z)} \right) \times e^{i(m+n+1)\theta(z) + \frac{ik\rho^2}{2q(z)}}, \quad (2.47)$$

where H_m and H_n are Hermite polynomials. $q(z)$ and $w(z)$ are discussed below and z_R is given by

$$z_R = \frac{\pi w_0^2}{\lambda}. \quad (2.48)$$

We can understand the physical significance of Eq. (2.38) by inserting Eq. (2.40) into the exponential of Eq. (2.17):

$$e^{\frac{ik(x^2+y^2)}{2R(z)} - \frac{x^2+y^2}{w(z)}} \quad (2.49)$$

In doing so it is seen that $w(z)$ is a measure of the beam size as a function of propagation distance, z . As required, the beam intensity drops off in a Gaussian manner, as shown in Fig. 2.1. $w(z)$ is located where the intensity of the field goes to $1/e^2$ of its maximum value, this is demonstrated for the fundamental ($n = m = 0$) Gaussian beam in Fig. 2.1. This beam size will be referred to as the *spot size* or *beam radius* in the following sections. The other real parameter, R , is the radius of curvature of the wavefront. w_0 is the minimum spot size of the beam and is at the *beam waist*. z_R , given by Eq. (2.48), is known as the *Rayleigh range* and is the distance from the waist where the spot size increases to $\sqrt{2}$ of its value at the waist. The relative locations of the beam waist and the first Rayleigh range is given in Fig. 2.2.

2.1.2 Laguerre-Gauss solutions of the scalar wave equation

While the Hermite-Gauss mode functions form a complete set of solutions to the wave equation they are not the only set. Laguerre-Gauss beams also form a complete set of solutions to the scalar wave equation in circular cylindrical coordinates. To find the cylindrical solutions we follow a method similar to the one used to find the Hermite-Gauss solutions. We seek solutions to the

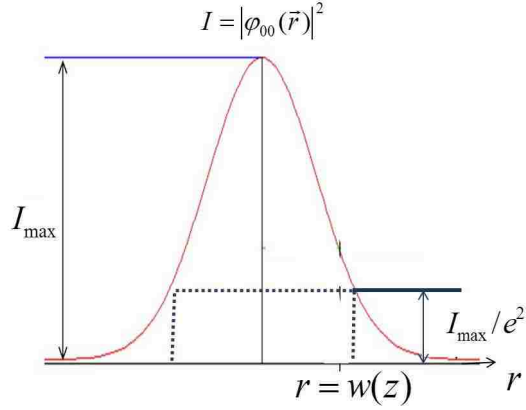


Figure 2.1: Intensity of the fundamental Gaussian beam. The radius $w(z)$ of the spot size of the beam is defined as the distance from the center of the beam to the location where the intensity drops to $1/e^2$ of its maximum value (I_{max}). Here, $r = \sqrt{x^2 + y^2}$.

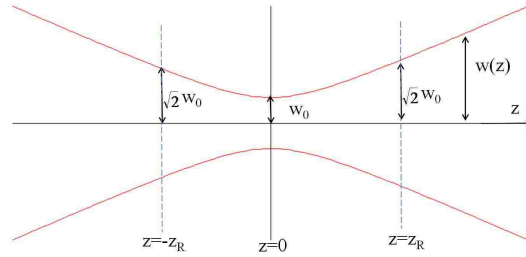


Figure 2.2: Beam waist and first Rayleigh range locations.

scalar wave equation in cylindrical coordinates,

$$\left[\nabla_{\perp}^2 + 2ik \frac{\partial}{\partial z} \right] \psi(r, \phi, z) = 0, \quad (2.50)$$

where $k = 2\pi/\lambda$ is the magnitude of the wave vector and

$$\nabla_{\perp}^2 = \frac{\partial^2}{\partial r^2} + \frac{1}{r} \frac{\partial}{\partial r} + \frac{1}{r^2} \frac{\partial^2}{\partial \phi^2}. \quad (2.51)$$

Motivated by the previously found Hermite-Gauss solutions we start by assuming a solution of the form [46]:

$$\psi_\ell(r, \phi, z) = \left(\frac{\sqrt{2}r}{w(z)} \right)^\ell L \left(\frac{2r^2}{w^2(z)} \right) e^{\frac{ikr^2}{2q(z)} + i\ell\phi - G(z)}, \quad (2.52)$$

We expect the solution to be a power series in r . Due to the periodic nature of cylindrical coordinates in the azimuthal coordinates we must impose a restriction on ℓ to ensure that the ϕ dependence is single valued. We have chosen the ϕ dependence to be $e^{i\ell\phi}$, where ℓ must be an integer, so that this single-valued periodic boundary condition is met. $G(z)$ is a function to be determined and expected to be similar to the phase shift found for the Hermite-Gauss solution. We are now left to find our trial solution by substituting Eq. (2.52) into Eq. (2.50) and endeavor to find the unknown functions L and G . We will start by finding the derivatives of Eq. (2.50):

$$\frac{\partial}{\partial r} \psi_\ell(\vec{r}) = \left(\frac{\sqrt{2}r}{w} \right)^\ell \left[\frac{\ell}{r} L + \frac{4r}{w^2(z)} L' - \frac{ikr}{q(z)} L \right] e^{\frac{ikr^2}{2q(z)} + im\phi - G(z)}, \quad (2.53)$$

$$\begin{aligned} \frac{\partial^2 \psi_\ell(\vec{r})}{\partial r^2} = & \left(\frac{\sqrt{2}r}{w} \right)^\ell \left[\frac{16r^2}{w^4(z)} L'' + \left(\frac{8\ell}{w^2(z)} - \frac{8r^2 ik}{q(z)w^2(z)} + \frac{4}{w^2(z)} \right) L' + \right. \\ & \left. \left(\frac{(ik)^2 r^2}{q^2(z)} - \frac{2\ell ik}{q(z)} - \frac{ik}{q(z)} + \frac{\ell^2}{r^2} - \frac{\ell}{r^2} \right) L \right] e^{\frac{ikr^2}{2q(z)} + i\ell\phi - G(z)}, \end{aligned} \quad (2.54)$$

$$\begin{aligned} \frac{\partial \psi_\ell(\vec{r})}{\partial z} = & \left(\frac{\sqrt{2}r}{w} \right)^\ell \left[-\frac{dw(z)}{dz} \frac{4r^2}{w^3(z)} L \right. \\ & \left. + \left(-\frac{dq(z)}{dz} \frac{r^2 ik}{2q^2(z)} - \frac{dw(z)}{dz} \frac{\ell}{w(z)} - \frac{dG(z)}{dz} \right) L \right] e^{\frac{ikr^2}{2q(z)} + im\phi - G(z)}, \end{aligned} \quad (2.55)$$

and

$$\frac{\partial^2 \psi_\ell(\vec{r})}{\partial \phi^2} = - \left(\frac{\sqrt{2}r}{w(z)} \right)^\ell \ell^2 L e^{\frac{ikr^2}{2q(z)} + i\ell\phi - G(z)}, \quad (2.56)$$

where the argument, $2r^2/w^2(z)$, of L is suppressed. We have used single prime on L to denote a first derivative with respect to its argument and two primes as a second derivative with respect to

its argument. Putting it all together and simplifying we have

$$L \left(\frac{2lik}{q(z)} + \frac{2ik}{q(z)} - \frac{2ik\ell w'(z)}{w^3(z)} - 2ik \frac{dG(z)}{dz} \right) + L \left(\frac{8(m+1)}{w^2} + \frac{dw(z)}{dz} \frac{ik8r^2}{w^3(z)} \right) + L'' \frac{16r^2}{w^4(z)} = 0, \quad (2.57)$$

where we have used $dq(z)/dz = 1$. Rewriting we have:

$$\begin{aligned} & \frac{L''}{L} \frac{16r^2}{w^4(z)} + \frac{L'}{L} \left(\frac{8(\ell+1)}{w^2(z)} + \frac{8ikr^2}{w^2(z)q(z)} - \frac{8ikr^2 w'(z)}{w^3(z)} \right) \\ & = - \left(\frac{2lik}{q(z)} + \frac{2ik}{q(z)} - \frac{dw(z)}{dz} \frac{2ik\ell}{w^3(z)} - 2ik \frac{dG(z)}{dz} \right). \end{aligned} \quad (2.58)$$

Since the right hand side has no r dependence we will equate it to a constant C to put Eq. (2.58)

in a more manageable form:

$$L'' \frac{2r^2}{w^2(z)} + L' \left(1 + \ell + \frac{ikr^2}{q(z)} - \frac{dw(z)}{dz} \frac{ir^2}{w(z)} \right) + L \frac{Cw^2(z)}{2} = 0, \quad (2.59)$$

where

$$C = - \left(\frac{2lik}{q(z)} + \frac{2ik}{q(z)} - \frac{dw(z)}{dz} \frac{2ik\ell}{w^3(z)} - 2ik \frac{dG(z)}{dz} \right). \quad (2.60)$$

Writing

$$\frac{1}{q(z)} = \frac{1}{R(z)} + \frac{i2}{kw^2(z)}, \quad (2.40^*)$$

$$w(z) = w_0 \sqrt{1 + \left(\frac{z}{z_R} \right)^2}, \quad (2.38^*)$$

$$\frac{dw(z)}{dz} = \frac{zw_0}{\sqrt{1 + \left(\frac{z_R}{z} \right)^2}} = \frac{zw_0^2}{w(z)}, \quad (2.61)$$

and letting

$$\nu = \frac{2r^2}{w^2(z)}, \quad (2.62)$$

we are left with:

$$\nu L'' + L'(1 + \ell - \nu) + L \frac{Cw^2(z)}{2} = 0, \quad (2.63)$$

which is in the same form as the associated Laguerre differential equation [73],

$$\xi L'' + (1 + \ell + \xi)L' + pL = 0. \quad (2.64)$$

So we have

$$L\left(\frac{2r^2}{w^2(z)}\right) = L_p^\ell\left(\frac{2r^2}{w^2(z)}\right), \quad (2.65)$$

where L_p^ℓ is the associated Laguerre polynomial. Comparing Eqs. (2.63) and (2.64) we find that C must be

$$C = \frac{2p}{w^2(z)}. \quad (2.66)$$

We are now left to find $G(z)$. Consider Eq. (2.60) and Eq. (2.66) ,

$$-\frac{2ik}{q(z)}(\ell + 1) + \frac{dw(z)}{dz} \frac{2ikm}{w(z)} - 2ik \frac{dG(z)}{dz} = C = \frac{2p}{w^2(z)}. \quad (2.67)$$

Using Eq. (2.61) in Eq. (2.67) and rearranging, we are left with:

$$\frac{dw(z)}{dz} = -\frac{\ell + 1}{q(z)} - \frac{2lz}{kw^2(z)} + \frac{ip}{kw^2(z)}. \quad (2.68)$$

After putting Eq. (2.40) in for $1/q(z)$, Eq. (2.38) for $w(z)$, and simplifying Eq. (2.68) becomes

$$\begin{aligned} \frac{dG(z)}{dz} &= \frac{\ell + 1}{z - iz_R} - \frac{2lz - ip}{z_R \left[z + \left(\frac{z}{z_R}\right)^2 \right]} \\ &= \frac{z}{z_R^2 + z^2} + i(1 + \ell + 2p) \frac{z_R}{z_R^2 + z^2} \end{aligned} \quad (2.69)$$

After integrating both sides with respect to z , from 0 to z , the expression for $G(z)$ is found to be,

$$G(z) = i(\ell + 1 + 2p) \arctan\left(\frac{z}{z_R}\right) + \frac{1}{2} \ln\left(1 + \left(\frac{z}{z_R}\right)^2\right). \quad (2.70)$$

Here, the real part of $G(z)$ corresponds to the expected decrease in intensity with distance z , as the beam increases in diameter with propagation,

$$e^{\Re[G(z)]} = \exp \left[\frac{1}{2} \ln \left(1 + \left(\frac{z}{z_R} \right)^2 \right) \right] = \frac{w_0}{w(z)}, \quad (2.71)$$

where w_0 is the beam radius at its waist, taken to be at $z = 0$. Again, letting

$$\theta(z) = \arctan \left(\frac{z}{z_R} \right), \quad (2.72)$$

we see that the imaginary part of $G(z)$ gives a phase shift θ between a Gaussian beam and a plane wave. This phase shift is the same as the shift mentioned in the Hermite-Gauss derivation and is called the *Gouy phase shift* and will be discussed in the next section. After using Eqs. (2.65), (2.70), and (2.71) in Eq. (2.52) we have the Laguerre-Gauss beam solutions to the wave equation,

$$\psi_{p\ell}(r, \phi, z) = \frac{2w_0}{w(z)} \left(\frac{\sqrt{2}r}{w(z)} \right)^\ell L_p^\ell \left(\frac{2r^2}{w^2(z)} \right) e^{-i(2p+\ell+1)\theta(z) + ikr^2/2q(z) + i\ell\phi}. \quad (2.73)$$

An interesting feature of Laguerre-Gaussian beams is that they carry orbital angular momentum. Recall that the azimuthal dependence on the transverse field is in the form $\exp(i\ell\phi)$. The integer ℓ is known as the *topological charge* or the *azimuthal index* and gives the orbital angular momentum that the beam carries, $\ell\hbar$ per photon [32, 34]. Such LG beams that carry orbital angular momentum are often referred to as optical vortex beams [14, 15]. The sign of ℓ gives the handedness of the orbital angular momentum.

Gouy phase

It is important to discuss the Gouy phase and its physical significance. We shall see that its presence is responsible for the change of the cross-polarized higher-order beams with propagation and is the basis for the mode converter that will be discussed in the next chapter.

The Gouy phase, given by Eq. (2.72), represents the difference in phase shift of a gaussian beam with respect to a plane wave of the same wavelength. This phase was first discovered by Gouy and was then shown to exist for any wave as it passes through its focus [74]. In going through the waist, a fundamental Gaussian beam will experience a phase shift of π , which is demonstrated in Fig. 2.3.

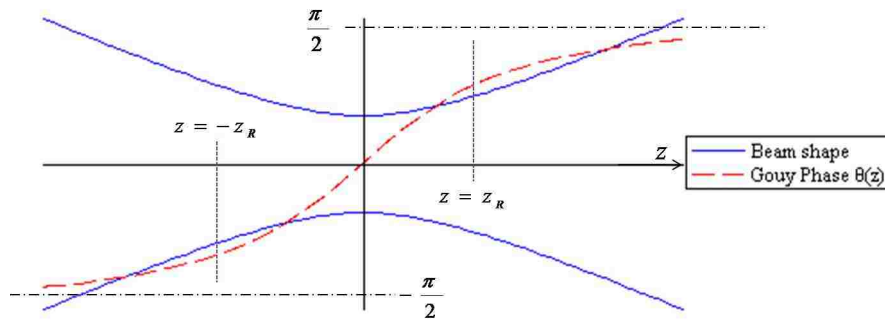


Figure 2.3: Gouy phase shift and beam shape for a gaussian beam.

Failure of the single-component solutions

Lax et. al., describing the failure of the single-component description as “an apparent paradox” in describing optical beams, were among the first to consider more than one component to the field [1]. It is easy to see why the single-component description fails for a beam of finite transverse size if we consider Eq. (2.1). With only one component for the electric field (for say an x -polarized beam) we are left with,

$$\frac{\partial \psi(\vec{r})}{\partial x} = 0. \quad (2.74)$$

The solution to Eq. (2.74) is a constant, $\psi(\vec{r}) = \psi_0$. This implies that for finite transverse size beam there must be more than one component to the field of a Gaussian beam, a dominant, cross, and longitudinal polarization term.

2.1.3 Vector Solutions

We now seek a solution to Maxwell's equations. We follow the treatment given by Erikson and Singh [12]. These solutions must be vectors and wavelike. Considering general electric and magnetic fields for a beam propagating in the z direction with angular frequency, ω , the fields are given by

$$\vec{E}(\vec{r}, t) = [\hat{x}E_1(\vec{r}) + \hat{y}E_2(\vec{r}) + \hat{z}E_3(\vec{r})] e^{i(kz - \omega t)}, \quad (2.75)$$

$$\vec{B}(\vec{r}, t) = [\hat{x}B_1(\vec{r}) + \hat{y}B_2(\vec{r}) + \hat{z}B_3(\vec{r})] e^{i(kz - \omega t)}, \quad (2.76)$$

where k is the wave vector. After inserting Eqs. (2.75) and (2.76) in Maxwell's equations and isolating $\vec{E}(\vec{r})$ and $\vec{B}(\vec{r})$ we arrive at the three components of the electric field. The electric field components for a beam dominantly polarized in the x direction are given by

$$E_1^{(mn)}(\vec{r}) = A_{mn} \psi_{mn}(\vec{r}), \quad (2.77)$$

$$E_2^{(mn)}(\vec{r}) = A_{mn} \left(\frac{1}{2k^2} \right) \frac{\partial^2 \psi_{mn}(\vec{r})}{\partial x \partial y}, \quad (2.78)$$

$$E_3^{(mn)}(\vec{r}) = A_{mn} \left(\frac{i}{k} \right) \frac{\partial \psi_{mn}(\vec{r})}{\partial x}, \quad (2.79)$$

where ψ_{mn} is given by Eqs. (2.46) or (2.73) and A_{mn} is related to the total power of the beam. In writing the previous three equations, only the leading nonzero terms have been kept.

Hermite-Gauss vector solutions

First we will consider Hermite-Gauss beams, therefore $\psi_{mn}(\vec{r})$ is given by Eq. (4.4). A_{mn} is determined by considering the total power of the beam, P_0 :

$$\begin{aligned} P_0 &= \frac{\epsilon_0 c}{2} \iint_{-\infty}^{\infty} |\vec{E}|^2 dx dy \\ &= \frac{\epsilon_0 c \pi w_0^2}{4} |A_{mn}(z)|^2 2^{n+m} m! n!, \end{aligned} \quad (2.80)$$

Solving for A_{mn} ,

$$A_{mn}(z) = \sqrt{\frac{4P_0}{\pi w_0^2 \epsilon_0 c 2^{n+m} m! n!}}. \quad (2.81)$$

Inserting Eq. (2.73) into Eqs. (2.77-2.79) we can derive explicit expressions for all three components of the field. We will start by considering the behavior of the field at the waist, $z = 0$. Once this behavior is determined for $z = 0$ the solution can be generalized for any distance, z . At the waist q and θ are given by,

$$\frac{1}{q(0)} = \frac{1}{R(0)} + \frac{i2}{kw_0^2} = \frac{i2}{kw_0^2} \quad \text{and} \quad \theta(0) = 0.$$

Let $X = \frac{\sqrt{2}x}{w^2(z)}$, $Y = \frac{\sqrt{2}y}{w^2(z)}$, and at the waist the dominant polarization component of the electric field is

$$\begin{aligned} E_1^{(mn)}(x, y, 0) &= A_{mn} \psi_{mn}(x, y, 0) \\ &= A_{mn} \sqrt{\frac{2}{\pi w_0^2}} H_m(X) H_m(Y) e^{-(X^2+Y^2)/2}. \end{aligned} \quad (2.82)$$

Using the definition of the derivative of a Hermite polynomial,

$$\frac{dH_m(x)}{dx} = 2mH_{m-1}(x), \quad (2.83)$$

and Eq. (2.75), we can find the cross polarization term:

$$\begin{aligned}
E_2 &= \left(\frac{A_{mn}}{2k^2} \right) \frac{\partial^2 \psi_{mn}(\vec{r})}{\partial x \partial y} \\
&= \left(\frac{A_{mn}}{2k^2} \right) \frac{\partial}{\partial y} \left[\sqrt{\frac{2}{\pi w_0^2}} \frac{1}{2} \left(2mH_{m-1}(X)H_n(y) - H_{m+1}(X)H_n(Y) \frac{\sqrt{2}}{w_0^2} \right) \right] \\
&= \left(\frac{A_{mn}}{2k^2} \right) \sqrt{\frac{2}{\pi w_0^2}} \frac{1}{w_0^2} \left[(2mH_{m-1}(X) - H_{m+1}(X)) 2nH_{n-1}(Y) \frac{\sqrt{2}}{w^2(z)} \right. \\
&\quad \left. + \left(-\frac{\sqrt{2}}{w_0} 2mH_{m-1}(X) - H_{m+1}(X) \right) H_n(Y) \right] e^{-i(m+m+1)\theta(z) + i\frac{kr^2}{2q}} \\
&= \left(\frac{A_{mn}}{2k^2} \right) \sqrt{\frac{2}{\pi w^2(z)}} \frac{1}{w_0^2} [(2mH_{m-1}(X) - H_{m+1}(X)) (2nH_{n-1}(Y) - H_n(Y))] e^{-\frac{(x^2+y^2)}{2}}.
\end{aligned}$$

Using another property of Hermite polynomials,

$$2xH_m(x) = H_{m+1}(x) + 2mH_{m-1}(x), \quad (2.84)$$

we have the cross-polarization component of $z = 0$

$$\begin{aligned}
E_2(x, y, 0) &= \left(\frac{A_{mn}}{4k^2 w_0^2} \right) \sqrt{\frac{2}{\pi w^2(z)}} [4mnH_{m-1}(X)H_{n-1}(Y) - 2mH_{m-1}(X)H_{n+1}(Y) \\
&\quad - 2nH_{m+1}(X)H_{n-1}(Y) + H_{m+1}(X)H_{n+1}(Y)] e^{-\frac{(x^2+y^2)}{2}} \\
&= \frac{A_{mn}}{4kw_0^2} [4mn\psi_{m-1, n-1}(x, y, 0) - 2m\psi_{m-1, n+1}(x, y, 0) \\
&\quad - 2n\psi_{m+1, n-1}(x, y, 0) + \psi_{m+1, n+1}(x, y, 0)]. \quad (2.85)
\end{aligned}$$

The longitudinal field component can similarly be found:

$$\begin{aligned}
E_3^{(mn)}(x, y, 0) &= \left(\frac{iA_{mn}}{k} \right) \frac{\partial \psi_{mn}(\vec{r})}{\partial x} \\
&= \left(\frac{iA_{mn}}{k} \right) \sqrt{\frac{2}{\pi w_0^2}} \left[-\frac{\sqrt{2}}{w_0} H_m(X)H_n(Y) + \frac{4\sqrt{2}}{w_0^2} mH_{m+1}(X)H_n(Y) \right] e^{-\frac{(x^2+y^2)}{2}},
\end{aligned}$$

where, using Eq. (2.84) we arrive at

$$\begin{aligned}
E_3(x, y, 0) &= \left(\frac{iA_{mn}}{k} \right) \sqrt{\frac{2}{\pi w_0^2}} \frac{1}{2} [2mH_{m-1}(X)H_n(Y) - H_{m+1}(X)H_n(Y)] e^{-\frac{(x^2+y^2)}{2}} \\
&= \left(\frac{iA_{mn}}{\sqrt{2}kw_0} \right) [\psi_{m-1,n}(x, y, 0) - \psi_{m+1,n}(x, y, 0)]. \tag{2.86}
\end{aligned}$$

It has already been shown that $\psi(\vec{r})$ satisfies the scalar wave equation therefore knowing the field at the waist we can write down the field at an arbitrary z :

$$E_1^{(mn)}(\vec{r}) = A_{mn}\psi_{mn}(\vec{r}), \tag{2.87}$$

$$\begin{aligned}
E_2^{(mn)}(\vec{r}) &= \left(\frac{A_{mn}}{4(w_0k)^2} \right) [4mn\psi_{m-1,n-1}(\vec{r}) - 2m\psi_{m-1,n+1}(\vec{r}) \\
&\quad - 2n\psi_{m+1,n-1}(\vec{r}) - \psi_{m+1,n}(\vec{r})], \tag{2.88}
\end{aligned}$$

$$E_3^{(mn)}(\vec{r}) = \left(\frac{iA_{mn}}{\sqrt{2}kw_0} \right) [2m\psi_{m-1,n}(\vec{r}) - 2m\psi_{m+1,n}(\vec{r})]. \tag{2.89}$$

Eqs. (2.87-2.89) are in agreement with Erikson and Singh [12]. Explicit expressions for some low-order modes are given in Table 2.1 and theoretical intensity profiles for them are given in Figs. 2.4-2.7, density plots were generated using Maple. We have introduced $N = m + n$ as the order of the mode.

Table 2.1: Intensity components for a HG_{mn} wave polarized in the x-direction

m, n	I_{xy}^{mn}	I_{yz}^{mn}	I_{zz}^{mn}
$N = 0$			
0, 0	$\left[\frac{2P_0}{\pi w^2(z)} \right] e^{-(X^2+Y^2)}$	$\left[\frac{P_0}{\pi w^2(z)} \right] X^2 Y^2 e^{-(X^2+Y^2)}$	$\frac{2}{(kw_0)^2} \left[\frac{P_0}{\pi w^2(z)} \right] X^2 e^{-(X^2+Y^2)}$
$N = 1$			
0, 1	$\left[\frac{2P_0}{\pi w^2(z)} \right] Y^2 e^{-(X^2+Y^2)}$	$\frac{1}{(kw_0)^4} \left[\frac{2P_0}{\pi w^2(z)} \right] X^2 e^{-(X^2+Y^2)}$ $\times \left[(1-Y^2)^2 \cos^2 \theta + Y^4 \sin^2 \theta \right]$	$\frac{2}{(kw_0)^2} \left[\frac{2P_0}{\pi w^2(z)} \right] X^2 Y^2 e^{-(X^2+Y^2)}$
1, 0	$\left[\frac{2P_0}{\pi w^2(z)} \right] X^2 e^{-(X^2+Y^2)}$	$\frac{1}{(kw_0)^4} \left[\frac{P_0}{\pi w^2(z)} \right] Y^2 e^{-(X^2+Y^2)}$ $\times \left[(1-X^2)^2 \cos^2 \theta + X^4 \sin^2 \theta \right]$	$\frac{2}{(kw_0)^2} \left[\frac{2P_0}{\pi w^2(z)} \right] e^{-(X^2+Y^2)}$ $\times \left[(1-X^2)^2 \cos^2 \theta + X^4 \sin^2 \theta \right]$
$N = 2$			
1, 1	$\left[\frac{4P_0}{\pi w^2(z)} \right] X^2 Y^2 e^{-(X^2+Y^2)}$	$\frac{1}{(kw_0)^4} \left[\frac{P_0}{\pi w^2(z)} \right] e^{-(X^2+Y^2)}$ $\times \left[(1-X^2)^2 \cos^2 \theta + X^4 \sin^2 \theta \right]$ $\times \left[(1-Y^2)^2 \cos^2 \theta + Y^4 \sin^2 \theta \right]$	$\frac{2}{(kw_0)^2} \left[\frac{4P_0}{\pi w^2(z)} \right] Y^2 e^{-(X^2+Y^2)}$ $\times \left[(1-X^2)^2 \cos^2 \theta + X^4 \sin^2 \theta \right]$
2, 0	$\left[\frac{P_0}{\pi w^2(z)} \right] (2X^2 - 1)^2 e^{-(X^2+Y^2)}$	$\frac{1}{(kw_0)^4} \left[\frac{P_0}{\pi w^2(z)} \right] X^2 Y^2 e^{-(X^2+Y^2)}$ $\times \left[(2X^2 - 5)^2 \cos^2 \theta + (2X^2 - 1)^2 \sin^2 \theta \right]$	$\frac{1}{(kw_0)^2} \left[\frac{2P_0}{\pi w^2(z)} \right] X^2 e^{-(X^2+Y^2)}$ $\times \left[(2X^2 - 5)^2 \cos^2 \theta + (2X^2 - 1)^2 \sin^2 \theta \right]$
0, 2	$\left[\frac{P_0}{\pi w^2(z)} \right] (2Y^2 - 1)^2 e^{-(X^2+Y^2)}$	$\frac{1}{(kw_0)^4} \left[\frac{P_0}{\pi w^2(z)} \right] X^2 Y^2 e^{-(X^2+Y^2)}$ $\times \left[(2Y^2 - 5)^2 \cos^2 \theta + (2Y^2 - 1)^2 \sin^2 \theta \right]$	$\frac{1}{(kw_0)^2} \left[\frac{2P_0}{\pi w^2(z)} \right] X^2 (2Y^2 - 1)^2 e^{-(X^2+Y^2)}$
$N = 3$			
1, 2	$\left[\frac{P_0}{2\pi w^2(z)} \right] X^2 (2Y^2 - 1)^2 e^{-(X^2+Y^2)}$	$\frac{1}{(kw_0)^4} \left[\frac{2P_0}{\pi w^2(z)} \right] Y^2 e^{-(X^2+Y^2)}$ $\times \left[(2Y^2 - 1)^2 \cos^2 \theta + Y^4 \sin^2 \theta \right]$	$\frac{1}{(kw_0)^2} \left[\frac{4P_0}{\pi w^2(z)} \right] (2Y^2 - 1)^2 e^{-(X^2+Y^2)}$ $\times \left[(X-1)^2 (X+1)^2 \cos^2 \theta + X^4 \sin^2 \theta \right]$
2, 1	$\left[\frac{P_0}{2\pi w^2(z)} \right] Y^2 (2X^2 - 1)^2 e^{-(X^2+Y^2)}$	$\frac{1}{(kw_0)^4} \left[\frac{2P_0}{\pi w^2(z)} \right] X^2 e^{-(X^2+Y^2)}$ $\times \left[(2X^2 - 1)^2 \cos^2 \theta + Y^4 \sin^2 \theta \right]$	$\frac{1}{(kw_0)^2} \left[\frac{4P_0}{\pi w^2(z)} \right] X^2 Y^2 e^{-(X^2+Y^2)}$ $\times \left[(2X^2 - 5)^2 \cos^2 \theta + (2X^2 - 1)^2 \sin^2 \theta \right]$
3, 0	$\left[\frac{P_0}{3\pi w^2(z)} \right] X^2 (2X^2 - 3)^2 e^{-(X^2+Y^2)}$	$\frac{1}{(kw_0)^4} \left[\frac{2P_0}{12\pi w^2(z)} \right] Y^2 e^{-(X^2+Y^2)}$ $\times \left[(2X^4 - 9X^2 + 3)^2 \cos^2 \theta - 2X^4 (2X^2 - 3)^2 \sin^2 \theta \right]$	$\frac{1}{24(kw_0)^2} \left[\frac{P_0}{\pi w^2(z)} \right] e^{-(X^2+Y^2)}$ $\times \left[(2X^4 - 9X^2 + 3)^2 \cos^2 \theta - 2X^4 (2X^2 - 3)^2 \sin^2 \theta \right]$
0, 3	$\left[\frac{P_0}{3\pi w^2(z)} \right] Y^2 (2X^2 - 3)^2 e^{-(X^2+Y^2)}$	$\frac{1}{(kw_0)^4} \left[\frac{2P_0}{12\pi w^2(z)} \right] X^2 e^{-(X^2+Y^2)}$ $\times \left[(2Y^4 - 9Y^2 + 3)^2 \cos^2 \theta - 2Y^4 (2Y^2 - 3)^2 \sin^2 \theta \right]$	$\frac{1}{12(kw_0)^2} \left[\frac{P_0}{\pi w^2(z)} \right] X^2 Y^2 (2Y^2 - 3)^2 e^{-(X^2+Y^2)}$

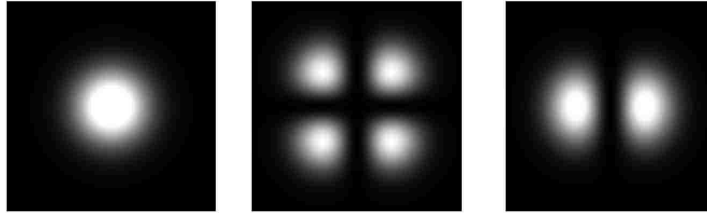


Figure 2.4: Intensity profile for the dominant, cross-polarization, and longitudinal components (left to right) for the fundamental Hermite-Gauss beam.

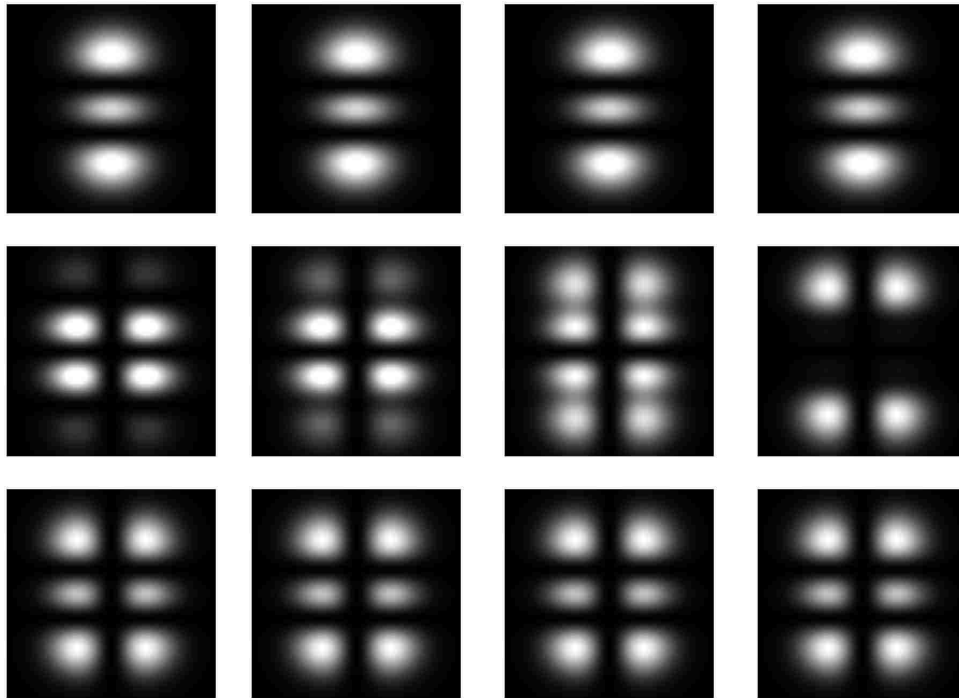


Figure 2.5: Evolution of intensity profile for the dominant, cross-polarization, and longitudinal components (top to bottom) for a linearly polarized $HG_{0,2}$ beam at $z = 0$, $z = \frac{1}{2}z_R$, $z = z_R$, and $z = 5z_R$ (left to right).

It is interesting to note that the dominant polarization component does not change shape with propagation but the cross-polarization component with nonzero n or m evolves with propagation. The longitudinal components also evolves for nonzero m . It is interesting to explore why the beam shape changes and why it evolves to a stable pattern. Recall the Gouy phase, given by Eq. (2.72),

$$\theta(z) = \arctan \frac{z}{z_R}, \quad (2.72^*)$$

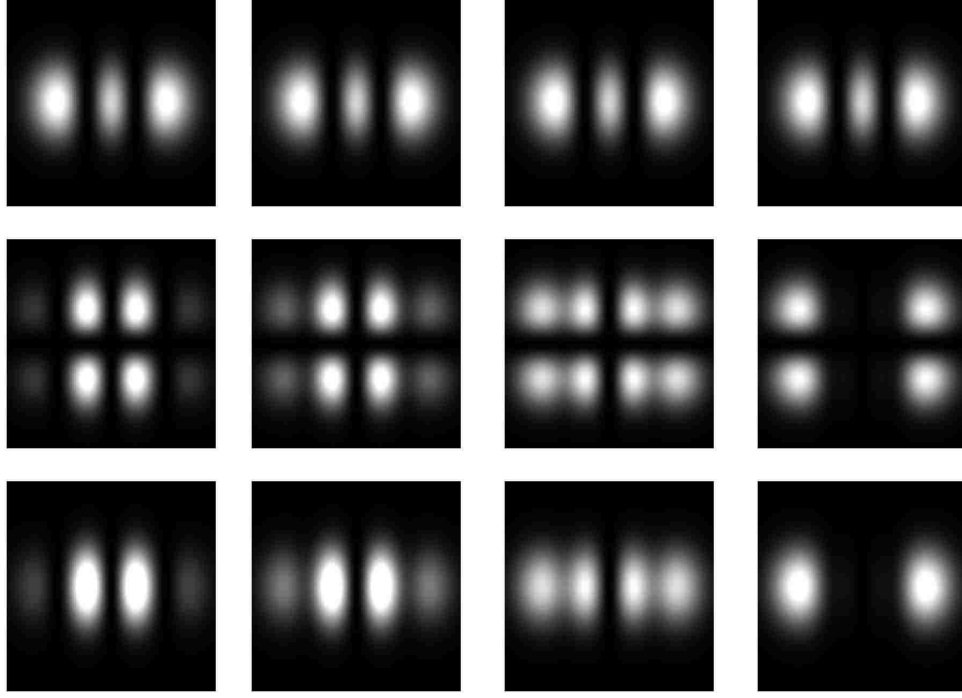


Figure 2.6: Evolution of intensity profile for the dominant, cross-polarization, and longitudinal components (top to bottom) for a linearly polarized $HG_{2,0}$ beam at $z = 0$, $z = \frac{1}{2}z_R$, $z = z_R$, and $z = 5z_R$ (left to right).

and consider, for example, the expression for the intensity profile for the cross-polarization component of the first higher order mode,

$$I_1^{(01)} = \frac{1}{(kw_0)^4} \left[\frac{2P_0}{\pi w^2(z)} \right] X^2 e^{-(X^2+Y^2)} \times [(1 - Y^2)^2 \cos^2 \theta(z) + Y^4 \sin^2 \theta(z)]. \quad (2.90)$$

From this expression, it can be seen that the only z dependence in the intensity profile is in the beam size $w(z)$ and the Gouy phase $\theta(z)$. w will only affect the size of the beam so the change in shape with propagation must be due to the presence of the Gouy phase. A closer look at the z dependence of the sin and cos term, graphed in Fig. 2.8, shows why the change in beam shape becomes less apparent after several Rayleigh ranges. From Fig. (2.8) we see that for $z \ll z_R$ $\sin \theta \approx 0$ and $\cos \theta \approx 1$. On the other hand for $z \gg z_R$ $\sin \theta \approx 1$ and $\cos \theta \approx 0$. The change after $z > 2z_R$ is small and eventually the mode reaches a stable pattern.

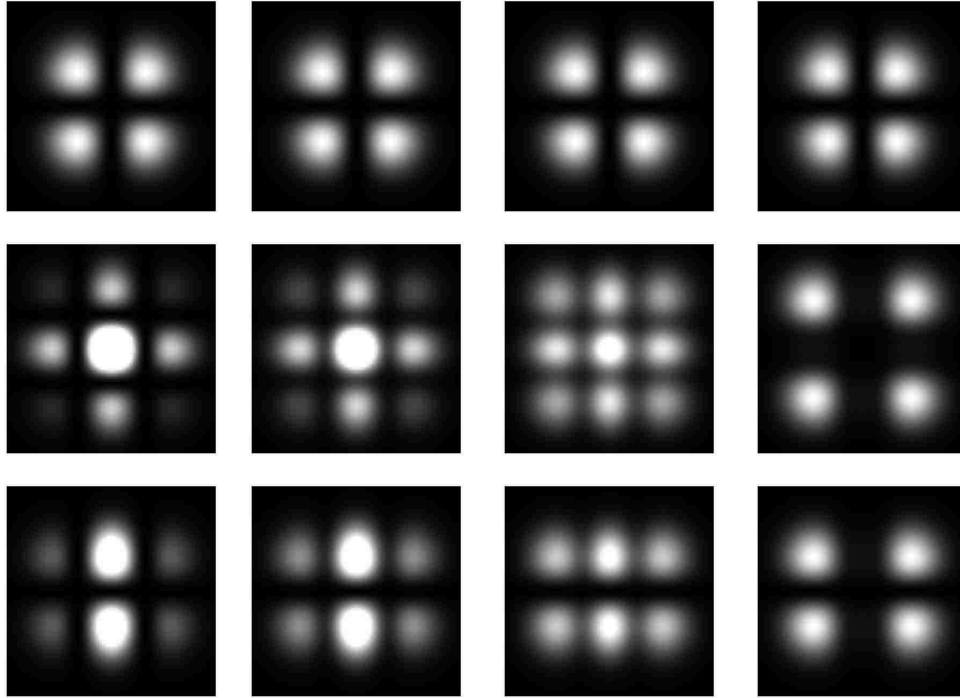


Figure 2.7: Evolution of intensity profile for the dominant, cross-polarization, and longitudinal components (top to bottom) for a linearly polarized $HG_{1,1}$ beam at $z = 0$, $z = \frac{1}{2}z_R$, $z = z_R$, and $z = 5z_R$ (left to right).

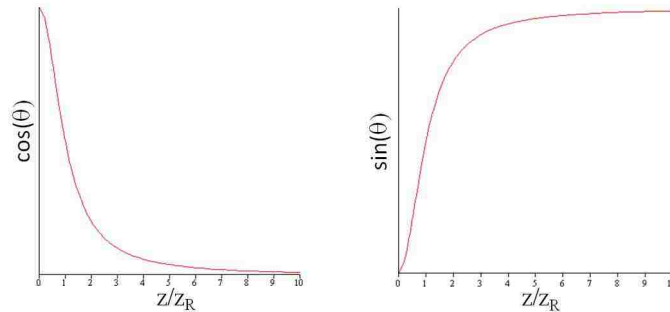


Figure 2.8: $\cos \theta(z)$ and $\sin \theta(z)$ verses z/z_R .

Further investigating the shape that different mode orders evolve to, consider $I_2^{(20)}$ far from the location of the beam waist ($z \gg z_R$) where

$$I_2^{(20)} = \frac{1}{(kw_0)^4} \left[\frac{P_0}{\pi w^2(z)} \right] X^2 Y^2 (2X^2 - 1)^2 e^{-(X^2 + Y^2)}, \quad (2.91)$$

along with $I_2^{(10)}$ and $I_2^{(30)}$

$$I_2^{(10)} = \frac{1}{(kw_0)^4} \left[\frac{P_0}{\pi w^2(z)} \right] Y^2 X^4 e^{-(X^2+Y^2)}, \quad (2.92)$$

$$I_2^{(30)} = \frac{1}{(kw_0)^4} \left[\frac{2P_0}{6\pi w^2(z)} \right] Y^2 X^4 (2X^2 - 3)^2 e^{-(X^2+Y^2)}. \quad (2.93)$$

These are shown graphically as density plots in Fig. 2.9. For an indication of what the structure of the intensity profiles evolves to far from the waist $I_2^{(50)}$ and $I_2^{(20,0)}$ are also graphically shown. Due

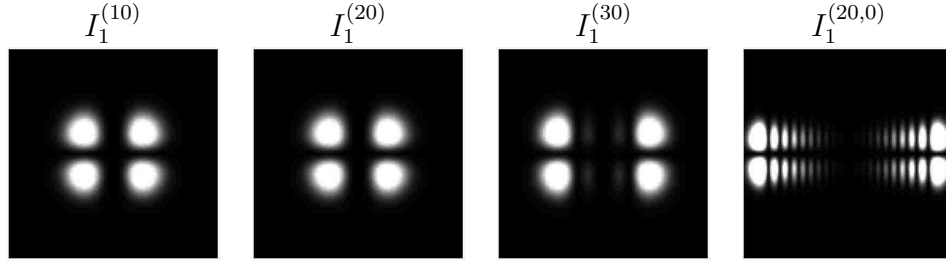


Figure 2.9: Intensity profiles for several orders for $z \gg z_R$

to the restrictions imposed by the radius of the bore of the laser cavity are not able to study modes with $N > 4$ experimentally.

Laguerre-Gauss vector solutions

We now discuss the vector solutions to Maxwell's equations in cylindrical coordinates. Again, a three component wave solution that satisfies Maxwell's equations is sought. It was shown in the previous section that for a beam propagating in the z direction and polarized in the x direction the field components are given by Eqs. (2.77)-(2.79):

$$E_1^{(\ell p)}(\vec{r}) = A_{\ell p} \psi_{\ell p}(\vec{r}), \quad (2.77^*)$$

$$E_2^{(\ell p)}(\vec{r}) = A_{\ell p} \left(\frac{1}{2k^2} \right) \frac{\partial^2 \psi_{\ell p}(\vec{r})}{\partial x \partial y}, \quad (2.78^*)$$

$$E_3^{(\ell p)}(\vec{r}) = A_{\ell p} \left(\frac{i}{k} \right) \frac{\partial \psi_{\ell p}(\vec{r})}{\partial x}. \quad (2.79^*)$$

In this section we are interested in beams in cylindrical coordinates. Therefore the dominant field amplitude is given by Eq. (2.73):

$$\psi_{\ell p}(r, \phi, z) = \frac{2w_0}{w(z)} \left(\frac{\sqrt{2}r}{w(z)} \right)^\ell L_p^\ell \left(\frac{2r^2}{w^2(z)} \right) e^{-i(2p+\ell+1)\theta(z)+ikr^2/2q(z)+i\ell\phi}. \quad (2.73^*)$$

It is necessary to first convert Eqs. (2.77-2.79) into cylindrical coordinates,

$$E_1^{(\ell p)}(r, \phi, z) = A_{\ell p} \psi_{\ell p}(r, \phi, z), \quad (2.94)$$

$$E_2^{(\ell p)}(r, \phi, z) = A_{\ell p} \left(\frac{1}{2k^2} \right) \left[\cos(2\phi) \left(\frac{1}{r} \frac{\partial^2}{\partial \phi r} - \frac{1}{r^2} \frac{\partial}{\partial \phi} \right) + \frac{1}{2} \sin(2\phi) \left(\frac{\partial^2}{\partial r^2} - \frac{1}{r} \frac{\partial}{\partial r} - \frac{1}{r^2} \frac{\partial^2}{\partial \phi^2} \right) \right] \psi_{\ell p}(r, \phi, z), \quad (2.95)$$

$$E_3^{(\ell p)}(r, \phi, z) = A_{\ell p} \left(\frac{i}{k} \right) \left[\cos(\phi) \frac{\partial}{\partial r} - \frac{\sin(\phi)}{r} \frac{\partial}{\partial \phi} \right] \psi_{\ell p}(r, \phi, z). \quad (2.96)$$

The cross polarization component of the electric field, E_2 , will be found first. After rewriting sin and cos in terms of exponentials, taking the required derivatives, and gathering coefficients of the same power we have,

$$E_2^{\ell p}(r, \phi, z) = \left\{ e^{i(\ell-2)\phi} \frac{\xi^{\ell-2}}{4} \left[\ell \xi'^2 L - \frac{\ell}{r} \xi \xi' L + \frac{1}{r} \xi'^2 L + \ell \xi \xi' L' - \frac{4\ell}{w^2(z)} r \xi \xi' L - \frac{4}{w^2(z)} r \xi^2 L' + \frac{4}{w^4(z)} r^2 \xi^2 L + \frac{\ell^2}{r^2} \xi^2 L - \frac{2\ell}{r^2} \xi^2 L + \frac{2\ell^2}{r} \xi \xi' L + \frac{2\ell}{r} \xi^2 L' - \frac{4\ell L \xi^2}{w^2(z)} - \frac{1}{r} \xi^2 L'' + \xi^2 L'' \right] + e^{-i(\ell+2)\phi} \frac{1}{4} \left[-\ell^2 \xi^2 L - \frac{\ell^2}{\xi^2 r^2} L + \ell \xi'^2 L - \frac{2}{\xi^3} \ell \xi' L' + \frac{4r\ell}{\xi^3 w^2(z)} \xi' L + \frac{4r}{\xi^2 w^2(z)} L' - \frac{4r^2}{\xi^2 w^4(z)} L + \frac{\ell}{r \xi^3} \xi' L + \frac{2\ell}{r \xi^2} L' - \frac{\ell}{\xi^2 w^2(z)} L + \frac{1}{r \xi^2} L' - \frac{1}{\xi^2} L'' \right] \right\} e^{-i(2p+\ell+1)\theta+ikr^2/2q(z)}, \quad (2.97)$$

where, for simplicity, $\xi = \sqrt{2}r/w(z)$, $L_p^\ell = L$, and the argument of L , ξ^2 , has been suppressed. L' represents the first derivative of L_p^ℓ with respect to r , and L'' is the second derivative of L_p^ℓ with

respect to r . Evaluating the remaining derivatives

$$\xi' = \frac{d}{dr} \left(\frac{\sqrt{2}r}{w(z)} \right) = \left(\frac{\sqrt{2}}{w(z)} \right), \quad (2.98)$$

and by making use of recursion relations for Laguerre polynomials:

$$\frac{dL_p^\ell(x)}{dx} = -L_{p-1}^{\ell+1}(x), \quad (2.99)$$

$$L' = \frac{d}{dr} L \left(\frac{2r^2}{w^2(z)} \right) = - \left(\frac{4r}{w^2(z)} \right) L_{(p-1)}^{(\ell+1)} \left(\frac{\sqrt{2}r}{w(z)} \right), \quad (2.100)$$

$$L'' = \frac{d^2}{dr^2} L \left(\frac{2r^2}{w^2(z)} \right) = \left(\frac{4r}{w^2(z)} \right)^2 L_{(p-2)}^{(\ell+2)} \left(\frac{\sqrt{2}r}{w(z)} \right) - \left(\frac{4}{w^2(z)} \right) L_{(p-1)}^{(\ell+1)} \left(\frac{\sqrt{2}r}{w(z)} \right) \quad (2.101)$$

which, after taking $z = 0$, we are left with,

$$\begin{aligned} E_2^{\ell p}(r, \phi, 0) = & A_{\ell p} e^{i(\ell-2)\phi} \frac{\xi^{\ell-2}}{w_0^2} \left[\left(-2\ell + 2\ell^2 - 2\xi^2\ell + \frac{1}{2}\xi^4 \right) L_p^\ell \right. \\ & \left. + (\xi^2 - 4\xi^2\ell + 2\xi^4 - \xi^2) L_{p-1}^{\ell+1} + 2\xi^4 L_{p-2}^{\ell+2} \right] \\ & + A_{\ell p} e^{i(\ell+2)\phi} \frac{\xi^{\ell+2}}{w_0^2} \left[-\frac{1}{2} L_p^\ell - 2L_{p-1}^{\ell+1} - 2L_{p-2}^{\ell+2} \right]. \end{aligned} \quad (2.102)$$

Eq. (2.102) can be further simplified using the following recursion relations for Laguerre polynomials:

$$xL_p^\ell(x) = (\ell + p)L_p^{\ell-1} - (p + 1)L_{p+1}^{\ell-1}, \quad (2.103)$$

$$\begin{aligned} x^2L_p^\ell(x) = & (\ell + p)(\ell + p - 1)L_{p-2}^{\ell-2}(x) - 2(\ell + p)(p + 1)L_{p+1}^{\ell-2}(x) \\ & + (p + 1)(p + 2)L_{p+2}^{\ell-2}, \end{aligned} \quad (2.104)$$

$$xL_{p-1}^{\ell+1}(x) = \ell L_p^\ell(x) - (\ell + p)L_p^{\ell-1}, \quad (2.105)$$

$$\begin{aligned}
x^2 L_{p-1}^{\ell+1}(x) &= \ell(\ell+p)L_p^{\ell-1}(x) - \ell(p+1)L_{p+1}^{\ell-1}(x) \\
&\quad - (\ell+p)(\ell+p-1)L_p^{\ell-1}(x) + (\ell+p)(p+1)L_{p+2}^{\ell-1}(x),
\end{aligned} \tag{2.106}$$

$$\begin{aligned}
xL_p^{\ell-1}(x) &= \ell(\ell+p)L_p^{\ell-1}(x) - \ell(p+1)L_{p+1}^{\ell-1}(x) \\
&\quad - (\ell+p)(\ell+p-1)L_p^{\ell-2}(x) + (\ell+p)(p+1)L_{p+1}^{\ell-2}(x),
\end{aligned} \tag{2.107}$$

$$xL_{p-2}^{\ell+2}(x) = -(\ell+p)L_{p-1}^{\ell}(x) + (\ell+1)L_{p-1}^{\ell+1}(x), \tag{2.108}$$

$$x^2 L_{p-2}^{\ell+2}(x) = \ell(\ell+1)L_p^{\ell}(x) - \ell(\ell+p)L_{p-1}^{\ell+1}(x) + (\ell+p)(\ell+p-1)L_p^{\ell-2}(x), \tag{2.109}$$

$$L_p^{\ell} = L_p^{\ell+2} - 2L_{p-1}^{\ell+2} - L_{p-2}^{\ell+2}, \tag{2.110}$$

and

$$L_{p-1}^{\ell+1} = L_{p-1}^{\ell+2} - L_{p-2}^{\ell+1}. \tag{2.111}$$

Letting $x = \xi^2$, we have

$$\begin{aligned}
E_2^{\ell p}(r, \phi, 0) &= A_{\ell p} e^{i(\ell-2)} \frac{\xi^{\ell-2}}{w_0^2} \left[\frac{1}{2}(\ell+p)(\ell+p-1)L_p^{\ell-2}(\xi^2) + (\ell+p)(p+1)L_p^{\ell-2}(\xi^2) + \frac{1}{2}L_{p+2}^{\ell-2}(\xi^2) \right] \\
&\quad - A_{\ell p} e^{i(\ell+2)} \frac{\xi^{\ell+2}}{2w_0^2} [L_p^{\ell+2}(\xi^2) + 2L_{p-1}^{\ell+2}(\xi^2) + L_{p-2}^{\ell+2}(\xi^2)]
\end{aligned} \tag{2.112}$$

$$\begin{aligned}
&= \left(\frac{iA_{p\ell}}{4(kw_0)^2} \right) [-\psi_{\ell+2,p}(r, \phi, 0) - 2\psi_{\ell+2,p-1}(r, \phi, 0) - \psi_{\ell-2,p-2}(r, \phi, 0) \\
&\quad + (p+1)(p+2)\psi_{\ell-2,p+2}(r, \phi, 0) + 2(\ell+p)(p+1)\psi_{\ell-2,p+1}(r, \phi, 0) \\
&\quad + (\ell+p)(\ell+p-1)\psi_{\ell-2,p}(r, \phi, 0)]
\end{aligned} \tag{2.113}$$

The next task is to find the longitudinal polarization component. Starting with the following recursion property of Laguerre polynomials,

$$\frac{dL_p^{\ell}(x)}{dx} = -L_{p-1}^{\ell+1}(x), \tag{2.114}$$

we find the derivative of the Laguerre polynomial,

$$\frac{d}{dr} L_p^\ell \left(\frac{2r^2}{w^2(z)} \right) = -\frac{4r}{w^2(z)} L_{p-1}^{\ell+1} \left(\frac{2r^2}{w^2(z)} \right). \quad (2.115)$$

Taking the rest of the required derivatives we are left with,

$$\begin{aligned} E_3^{\ell p}(r, \phi, z) = & \left(\frac{iA_{\ell p}}{2k} \right) \xi^\ell \left[(e^{i\phi} + e^{-i\phi}) \left(L_p^\ell(\xi^2) - \frac{4r}{w^2(z)} L_{p-1}^{\ell+1}(\xi^2) \right) \right. \\ & \left. + (e^{-i\phi} - e^{i\phi}) i\ell L_p^\ell(\xi^2) \right] e^{ikr^2/2q(z) - i(2p+\ell+1)\theta - i\ell\phi}. \end{aligned} \quad (2.116)$$

Eq. (2.116) can be further simplified by letting $\xi = \sqrt{2}r/w(z)$ and looking at $z = 0$ (ie. $w(0) = w_0$, $\theta(z) = 0$, and $q(0) = -iw_0/2k$):

$$\begin{aligned} E_3^{\ell p}(r, \phi, 0) = & \left(\frac{iA_{\ell p}}{2k} \right) \left[e^{i(\ell+1)\phi} \frac{\xi^\ell}{2rw_0} (-\xi^2 L_p^\ell(\xi^2) - 2\xi^2 L_{p-1}^{\ell+1}(\xi^2)) \right. \\ & \left. + e^{i(\ell-1)\phi} \frac{\xi^\ell}{2rw_0} (-\xi^2 L_p^\ell(\xi^2) (2\ell - \xi^2) - 2\xi^2 L_{p-1}^{\ell+1}(\xi^2)) \right]. \end{aligned} \quad (2.117)$$

Next, taking advantage of the following recursion relations of Laguerre polynomials,

$$L_p^\ell(x) = L_p^{\ell+1}(x) - L_{p-1}^{\ell+1}(x), \quad (2.118)$$

$$xL_{p-1}^{\ell+1}(x) = -(\ell + p)L_p^{\ell-1}(x) + \ell L_p^\ell(x), \quad (2.119)$$

Eq. (2.116) simplifies to,

$$\begin{aligned} E_3^{\ell p}(r, \phi, 0) = & \left(\frac{iA_{\ell p}}{2k} \right) \frac{1}{\sqrt{2}w_0} \left[e^{i(\ell+1)\phi} \xi^{\ell+1} [-L_p^{\ell+p} - L_{p-1}^{\ell+1}] \right. \\ & \left. + e^{i(\ell-1)\phi} \xi^{\ell-1} [(\ell + p)L_p^{\ell-1} + (p + 1)L_{p+1}^{\ell-1}] \right] \\ = & \left(\frac{iA_{\ell p}}{2k} \right) \frac{1}{\sqrt{2}w_0} [-\psi_{\ell+1,p}(r, \phi, 0) - \psi_{\ell+1,p-1}(r, \phi, 0) \\ & + (\ell + p)\psi_{p,\ell-1}(r, \phi, 0) + (p + 1)\psi_{p+1,\ell-1}(r, \phi, 0)]. \end{aligned} \quad (2.120)$$

Where the field components satisfy Maxwell's equations and the paraxial wave equation

$$\left[\nabla_{\perp}^2 + 2ik \frac{\partial}{\partial z} \right] E_i(r, \phi, z) = 0, \quad (2.121)$$

where, E_i , $i = 1, 2, 3$ is given by Eq. (2.75). Having found the field components for $z = 0$ we can now write down the components for arbitrary z using the fact that Eqs. (2.77*), (2.113), and (2.120) satisfy the paraxial wave equation:

$$E_1^{\ell p}(r, \phi, z) = A_{\ell p} \psi_{\ell p}(r, \phi, z) \quad (2.122)$$

$$\begin{aligned} E_2^{\ell p}(r, \phi, z) = & \left(\frac{iA_{\ell p}}{4(kw_0)^2} \right) [-\psi_{\ell+2,p}(r, \phi, z) - 2\psi_{\ell+2,p-1}(r, \phi, z) - \psi_{\ell-2,p-2}(r, \phi, z) \\ & + (p+1)(p+2)\psi_{\ell-2,p+2}(r, \phi, z) + 2(\ell+p)(p+1)\psi_{\ell-2,p+1}(r, \phi, z) \\ & + (\ell+p)(\ell+p-1)\psi_{\ell-2,p}(r, \phi, z)] \end{aligned} \quad (2.123)$$

$$\begin{aligned} E_3^{\ell p}(r, \phi, z) = & \left(\frac{iA_{\ell p}}{\sqrt{2}w_0k} \right) [-\psi_{\ell+1,p}(r, \phi, z) - \psi_{\ell+1,p-1}(r, \phi, z) \\ & + (\ell+p)\psi_{\ell-1,p}(r, \phi, z) + (p+1)\psi_{\ell-1,p+1}(r, \phi, z)]. \end{aligned} \quad (2.124)$$

Eqs. (2.122-2.124) are in agreement with Vyas and Singh [75].

The constant $A_{\ell p}$ can be found by considering the total power of the beam P_0 :

$$P_0 = \int_0^{\infty} \int_0^{2\pi} I(r, \phi, z) r dr d\phi, \quad (2.125)$$

where

$$I = \frac{1}{2} \varepsilon_0 c |E_{\ell p}|^2. \quad (2.126)$$

This gives,

$$\begin{aligned} P_0 = & 2\pi \left(\frac{1}{2} \varepsilon_0 c |A_{\ell p}|^2 \right) \frac{4w_0^2}{w^2(z)} \int_0^{\infty} \left(\frac{\sqrt{2}r}{w(z)} \right)^{2\ell} \left| L_p^{\ell} \left(\frac{2r^2}{w^2(z)} \right) \right|^2 e^{-2r^2/w^2(z)} dr, \\ = & \pi \varepsilon_0 c w_0^2 |A_{\ell p}|^2 \frac{(\ell+p)!}{p!}, \end{aligned} \quad (2.127)$$

which upon solving for the constant $A_{\ell p}$ yields,

$$A_{\ell p} = \sqrt{\frac{P_0 p!}{w_0^2 \pi \epsilon_0 c n (\ell + p)!}}. \quad (2.128)$$

The fundamental Gaussbeam is recovered for $\ell = p = 0$. Figures 2.10, 2.11, and 2.12 show the intensity profiles of the dominant, cross, and longitudinal-polarization components for a few orders of LG beams.

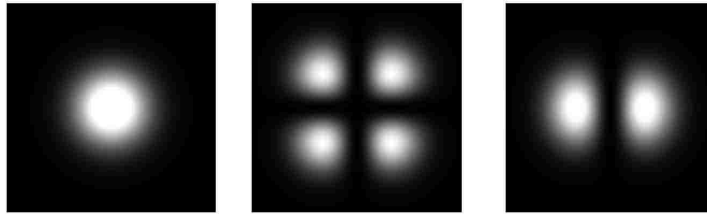


Figure 2.10: Intensity profile for the dominant, cross-polarization, and longitudinal components (left to right) for a linearly polarized fundamental Laguerre-Gauss beam.

Figure 2.10 shows the intensity profiles of the dominant, cross, and longitudinal-polarization components for a linearly polarized fundamental Laguerre-Gaussbeam, which is the same as the HG beam. The intensity profiles of all three of the components undergo an increase in size but do not change shape with propagation. The cross-polarization component of the fundamental beam, having a four lobed pattern, is mathematically the same as the HG_{11} mode. With a two lobed pattern, the longitudinal-polarization component is the same as the HG_{10} mode.

The evolution of the dominant, cross, and longitudinal-polarization intensity profiles of a linearly polarized LG_{10} with propagation is shown in Fig. 2.11. The cross-polarization component has a four blade structure that undergoes a rotation as the beam propagates away from its waist. The intensity profile for this component stabilizes to a four lobe pattern that is a linear combination of the cross-polarization components of the HG_{10} and HG_{01} modes far from the waist.

Figure 2.12 gives the intensity profiles of the three polarization components of a linearly polarized LG_{11} beam at different distances from the focus of the beam. Comparing 2.11 and 2.12 it is seen

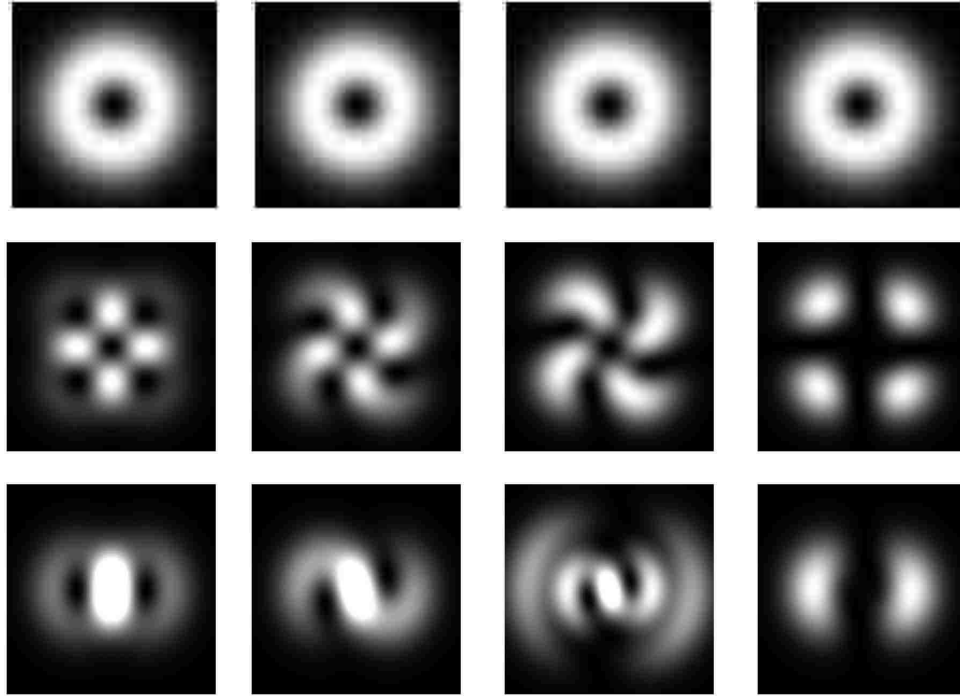


Figure 2.11: Evolution of intensity profile for the dominant, cross-polarization, and longitudinal components (top to bottom) for a linearly polarized LG_{10} beam at $z = 0$, $z = \frac{1}{2}z_R$, $z = z_R$, and $z = 10z_R$ (left to right).

that the evolution of the cross and longitudinal-polarization intensity profiles of the LG_{10} and LG_{11} beams are very similar.

Again notice that, similar to the HG modes, the dominant polarization component does not change shape with propagation while the cross and longitudinal components of higher-order beams undergo an evolution as the beam propagated away from the focus. Once again the evolution of the cross and longitudinal components is due to their dependence on Gouy's phase.

2.2 Poynting vector

Here the significance of the longitudinal-polarization component on the energy flow of Maxwell-Gauss beams is discussed. The energy flow of a electromagnetic beam is described by the Poynting vector. The vectors that describe the energy flow of Gauss laser beams should converge as they ap-

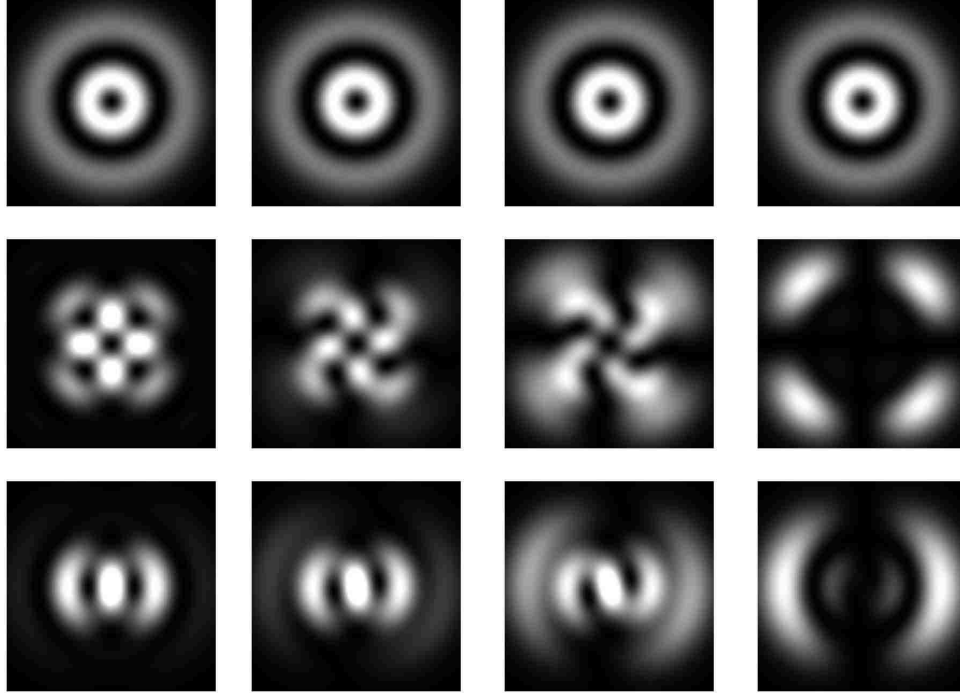


Figure 2.12: Evolution of intensity profile for the dominant, cross-polarization, and longitudinal components (top to bottom) for a linearly polarized LG_{11} beam at $z = 0$, $z = \frac{1}{2}z_R$, $z = z_R$, and $z = 10z_R$ (left to right)

proach the focus of the beam and diverge as they leave the focal region. With out the longitudinal-polarization component of the field the Poynting vector does not possess this property [12]. The Poynting vector averaged over an optical cycle is given by

$$\vec{S}(\vec{r}) = \frac{1}{2}\varepsilon_0 c^2 \Re \left[\vec{E}(\vec{r}) \times \vec{B}^*(\vec{r}) \right], \quad (2.129)$$

where $\vec{E}(\vec{r})$ is given by Eqs. (2.87)-(2.89) and

$$\vec{B}^*(\vec{r}) = \hat{x} \frac{1}{c} E_2 - \hat{y} \frac{1}{c} E_1 - \hat{z} \frac{i}{kc} \frac{\partial E_1}{\partial y}. \quad (2.130)$$

Here, we will assume Cartesian coordinates and work with Hermite-Gauss beams. Hence using the fields given by Eqs. (2.87)-(2.89) and making use of the Hermite recursion relations given in

Eqs.(2.83) and (2.84), Eq. (2.130) becomes

$$\vec{S}(\vec{r}) = \frac{1}{2}\epsilon_0 c^2 |A_{mn}|^2 \psi_{mn}(\vec{r}) \left[\hat{x} \frac{x}{R(z)} + \hat{y} \frac{y}{R(z)} + \hat{z} \right]. \quad (2.131)$$

Here, $R(z)$ is the radius of curvature of the wave front, and is positive for a diverging wave and negative for a converging wave. ψ_{mn} and A_{mn} are given by Eqs. (2.46) and (2.81), respectively. Figure 2.13 shows the Poynting vector of a Gauss beam at different locations as the beam propagates to the right.

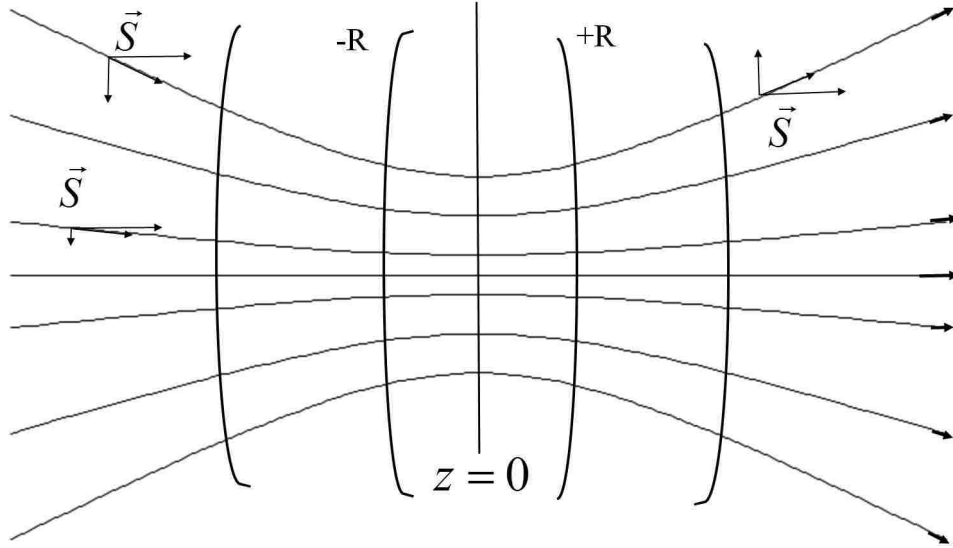


Figure 2.13: The energy flow of a Gauss beam near its focus propagating to the right. Line segments represent local trajectories of the Poynting vector, curves perpendicular to them represent the curved wave front.

If the longitudinal component is not retained in describing the field, the energy flow vector would only point in the z direction. Therefore, in order to properly describe the energy flow of the beam the presence of the longitudinal component is necessary .

2.3 Chapter summary

In this chapter we have discussed the structure of linearly polarized Hermite-Gauss and Laguerre-Gauss laser beams. The need for a three-component vector solution is presented followed by a derivation of said solutions. Theoretical intensity profiles for a few low order of Hermite-Gauss and Laguerre-Gauss beams are given at different distances from the beam's waist. The intensity profiles of the cross-polarization component of both HG and LG beams change shape with propagation for $N = n + m > 0$. The longitudinal-polarization component evolves with propagation for nonzero n or m for the LG beam and when m is nonzero for the HG beam. We have also discussed the importance of the longitudinal-polarization component in properly describing the energy flow of the beam.

Chapter 3

Linearly Polarized Hermite-Gauss Laser Beams

In this chapter we present the experimental setup used to generate and verify the polarization structure of linearly polarized Hermite-Gauss laser beams. In addition to the experimental setup, we present experimentally recorded profiles for linearly polarized Hermite-Gauss laser beams. A comparison between the theoretical and experimental profiles is also carried out in this chapter.

3.1 Generation of higher-order Hermite-Gauss laser beams

Typically, it is not desirable to have the laser operate in higher order modes. However, in general, there can be a mixture of the fundamental mode (HG_{00}) and higher order modes at any time in the cavity. An aperture can be introduced within the laser cavity to force only the fundamental mode to oscillate. Here we desire to generate the fundamental and higher-order modes, one at a time. We do this by taking advantage of the fact that a laser will oscillate in the mode which has minimal loss. The inclusion of non-symmetric elements in the cavity such the Brewster window attached to the laser gain tube forces rectangular symmetry. Higher-order modes can be generated by inserting a wire or a fiber at one of the nodes of the desired modes, as shown in Fig. 3.1 [15]. The top row shows the intensity distribution along the x -direction and the bottom row gives the beam profile. Note that the wire only needs to be at one of the zeros of the mode (in each direction). This same idea can be applied to generate modes with more than one lobe in both coordinates by using a pair of crossed wires, as shown in Fig. 3.2. This method can be used to generate any higher-order mode, the order of the mode is only limited by the radius of the bore of the gain tube as the radius of the beam increases with mode number.

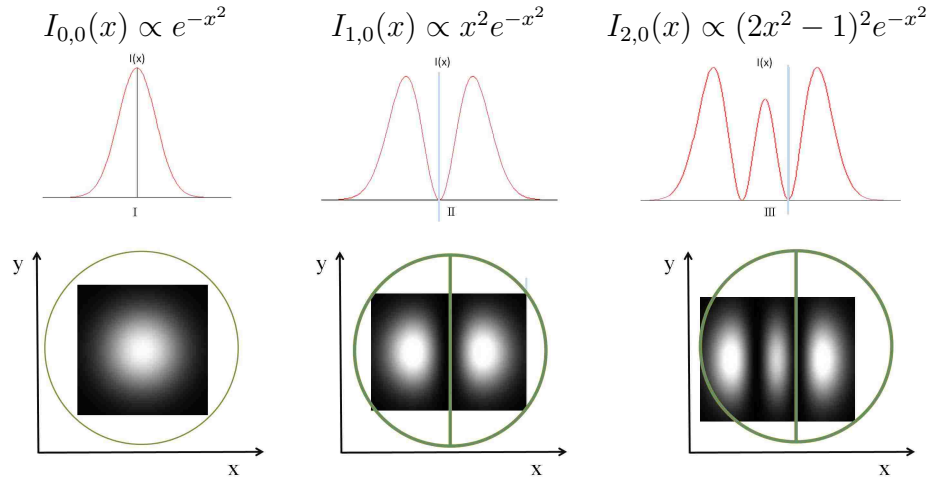


Figure 3.1: Intensity distribution and beam profiles for HG_{00} , HG_{10} , and HG_{20} modes in demonstration of higher-order mode generation

$$I_{11}(x, y) \propto x^2 y^2 e^{-(x^2 + y^2)}$$

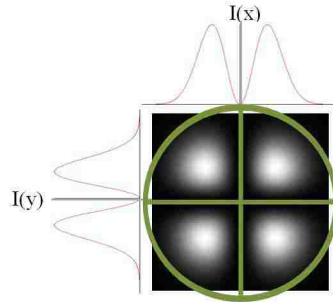


Figure 3.2: Intensity distribution demonstrating HG_{11} generation

Physically, higher order Hermite-Gaussian mode generation can be understood by considering resonating modes of stable resonators. For a mode to be resonant with the cavity boundary conditions must be met, i.e. the distribution of the field must maintain its shape over each pass of the cavity, must undergo a phase shift in a multiple of 2π , and gain must exceed the loss in each round trip [45]. As stated above, by inserting a fiber at a node of a desired higher-order HG mode the desired mode can be generated. This is obvious for modes with only one node (in each transverse direction) but less so for modes with more than one node in a transverse direction we find that only *one* fiber is required (in each transverse direction), even for modes with more than one node in that direction.

The modes in laser cavities were modeled by Fox and Li by considering round trip propagation of a wave in a laser cavity [76]. Fox and Li calculations are analytical calculations that find the change in the transverse profile of the beam with several round trips in the cavity. The idea here is that with the repeated round trips a set of discrete transverse eigenmodes (field profiles) will be found. These self reproducing modes depend on the shape and curve of the laser mirrors and other losses introduced in the cavity (such as the crossed fibers) these transverse modes are similar to the transverse modes of a waveguide. Once the laser starts oscillating in one of these eigenmodes and the gain medium produces sufficient population inversion, overcoming the losses, then it will be a steady state solution and produce the desired order and family of beam. It can then be understood that, in addition to the typical optical elements, placing a fiber at only one of the nodes in each transverse direction are the necessary and sufficient boundary conditions to force operation in the desired order.

3.2 Hermite-Gaussian setup

A coherent CR-12 super graphite laser head fitted with an Innova-15 plasma tube was used to generate higher order Hermite-gaussian beams. The laser normally operates in the fundamental mode. The laser cavity was modified to facilitate generation of higher-order modes as follows. The cavity was extended by attaching an external frame to the original cavity. The extended cavity provided additional space to insert a pair of fibers described in Section 2. A diagram of the modified cavity and crossed fibers is given in Fig. 3.3. The original high reflectivity mirror was flat and the original output coupler had a radius of curvature of $R = 15\text{m}$, they were replaced by mirrors with a radius of curvature $R = 3\text{m}$ and specifically coated to reflect only 514nm , the new mirrors, with a shorter radius of curvature, were necessary to decrease the beam radius of the fundamental mode so that higher order modes would fit into the bore of the tube (gain volume). The cavity expander and mirror modifications allowed up to $N = 3$ modes to be generated with power output of up to 400mW. In addition to the set of crossed fibers in the cavity to select higher order mode

operation, it was necessary to also include a pair of adjustable apertures to prevent undesirable modes from operating. The frames that hold the fibers and the slit apertures were mounted on micrometer translation stages, to allow their horizontal and vertical position to be adjusted relative to the cavity axis. Micrometer adjustments to the location of the fibers and the slits were necessary since the beam radius was only about half of a millimeter and the distance between nodes is a small fraction of that.

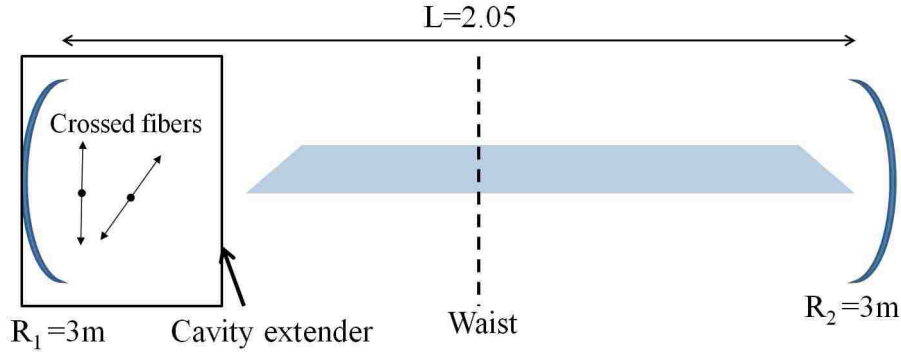


Figure 3.3: Diagram of modified laser cavity

A diagram of the experimental setup is given in Fig. (3.4). Since we have a standing wave cavity the beam size, waist location, and Rayleigh range are calculated as follows [45]. The beam waist inside the cavity is given by

$$w_{01} = \sqrt{\frac{L\lambda}{\pi} \left[\frac{g_1 g_2 (1 - g_1 g_2)}{(g_1 + g_2 - 2g_1 g_2)^2} \right]^{\frac{1}{4}}},$$

where

$$g_1 = 1 - \frac{L}{R_1}, \text{ and } g_2 = 1 - \frac{L}{R_2}. \quad (3.1)$$

In our case, the length of the cavity $L = 2.05$ m and the radius of curvature of the high reflectivity mirror and the output coupler is $R_1 = R_2 = 3$ m, giving us

$$g_1 = g_2 = 0.317.$$

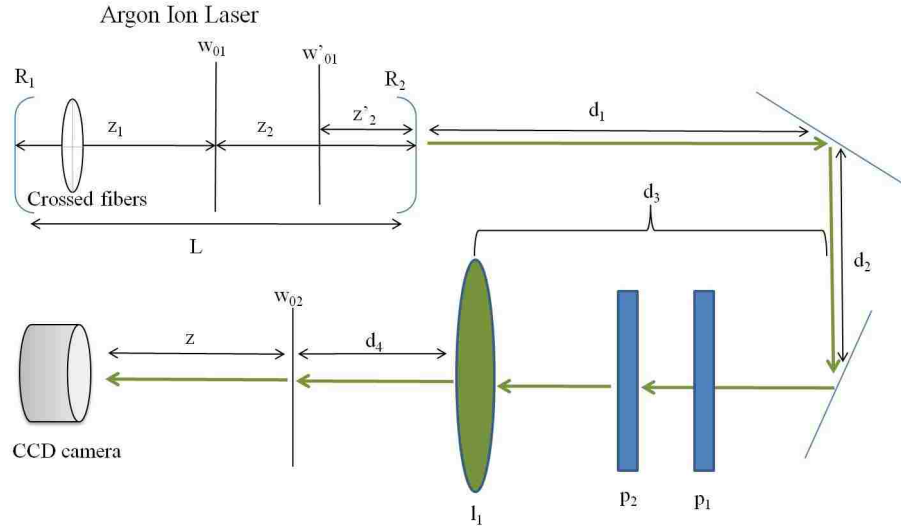


Figure 3.4: Hermite-Gauss Experimental setup

With $\lambda = 514 \text{ nm}$ the radius of the beam at the waist in the cavity is,

$$w_{01} = 0.482 \text{ mm.}$$

The beam waist is located a distance z_2 from the waist:

$$z_2 = \frac{g_1(1 - g_2)}{g_1 + g_2 - 2g_1g_2} L = 1.025 \text{ m.}$$

While the Brewster windows have little effect on the beam waist size and location we should

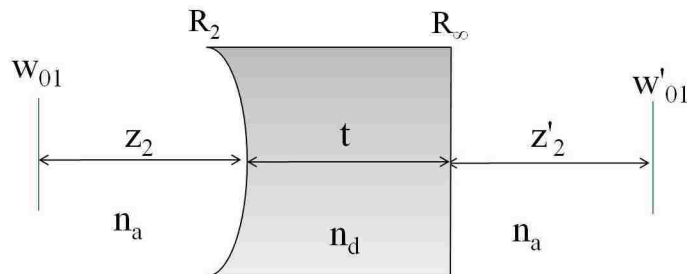


Figure 3.5: Modification of the beam waist location and spot size by the output coupler on exit from the laser cavity.

consider the change in the beam as it exits the cavity. It is necessary to consider the ray matrix of the system shown in Fig. 3.5. The beam is incident on the output coupler (of thickness t) from the left, the radius of curvature of the left side of the output coupler is $R_2 = 3$ m, the right side is plane. Call the distance of the output coupler from the beam waist inside the cavity z_2 and the beam radius w_{01} , and the new beam waist location z'_2 and the spot radius there w'_{01} . The matrix that describes the transformation of the beam exiting the laser cavity is given by:

$$\begin{aligned} \begin{pmatrix} A & B \\ C & D \end{pmatrix} &= \begin{pmatrix} 1 & z'_2 \\ 0 & 1 \end{pmatrix} \begin{pmatrix} 1 & 0 \\ \frac{n_a - n_d}{n_d} \frac{1}{R_\infty} & \frac{n_a}{n_d} \end{pmatrix} \begin{pmatrix} 0 & t \\ 0 & 1 \end{pmatrix} \begin{pmatrix} 1 & 0 \\ \frac{n_d - n_a}{n_a} \frac{1}{R_2} & \frac{n_d}{n_a} \end{pmatrix} \begin{pmatrix} 1 & z_2 \\ 0 & 1 \end{pmatrix} \\ &= \begin{pmatrix} 1 + \frac{t}{R_2} \left(\frac{n_a}{n_d} - 1 \right) + \frac{z'_2}{R} \left(1 - \frac{n_d}{n_a} \right) & z'_2 + z_2 + t \frac{n_a}{n_d} + \frac{z_2 t}{R_2} \left(\frac{n_a}{n_d} - 1 \right) + \frac{z'_2 z_2}{R_2} \left(1 - \frac{n_d}{n_a} \right) \\ \frac{1}{n_a R_2} (n_a - n_d) & 1 + \frac{z_2}{n_a R_2} (n_a - n_d), \end{pmatrix} \end{aligned} \quad (3.2)$$

where n_a is the index of refraction of air and n_d is the index of refraction of the mirror ($n_d \approx 1.5$). The ABCD matrix gives us the transformation equation,

$$q'_1 = \frac{Aq_1 + B}{Cq_1 + D}, \quad (3.3)$$

where q_1 and q'_1 are the complex beam parameters for at the right and left of the output coupler, respectively. In our case the complex beam parameters q_1 and q'_1 are purely imaginary since we have defined the ABCD matrix so that we go from the original waist at z_2 to the new waist at z'_2 ,

$$q_1 = -\frac{i\pi w_{01}^2}{\lambda} \quad \text{and} \quad q'_1 = -\frac{i\pi w'_{01}{}^2}{\lambda}. \quad (3.4)$$

Combining Eqs. (3.3) and (3.4) we arrive at

$$-iz'_{R1} = \frac{-iz_{R1}A + B}{-iz_{R1}C + D}. \quad (3.5)$$

Equating the real and imaginary parts of Eq. (3.5) we obtain

$$\Re(q'_1) = 0 = \frac{z_{R1}^2 AC + BD}{(z_{R1} C)^2 + D^2} \quad (3.6)$$

$$\Im(q'_1) = -z'_{R1} = \frac{z_{R1} (AD - BC)}{(z_{R1} C)^2 + D^2}. \quad (3.7)$$

After inserting $A, B, C, D, z_{R1} = \pi w_{01}^2/\lambda$, and $z'_{R1} = \pi w'_{01}{}^2/\lambda$ into Eq. (3.7) and inserting the given values we get the new beams waist

$$w'_{01} = 0.55 \text{ mm},$$

were $\lambda = 514 \text{ nm}$, $w_{01} = 0.482 \text{ mm}$, $n_a = 1$, and $n_d = 1.5$ is used. Similarly, from Eq. (3.6) we find the location of the beam waist to be

$$z'_2 = -73.7 \text{ cm},$$

which means that the new waist lies to the left of the output coupler mirror.

After leaving the laser cavity, the beam is sent through a pair of linear polarizers. The transmission axis of the first polarizer is always parallel to the direction of the dominant polarization component of the beam coming from the laser. The transmission axis of second polarizer was oriented to be parallel to the transmission axis of the first polarizer to observe the intensity profile of the dominant component. To observe the intensity profile of the cross-polarization component, the transmission axes of the second polarizer was aligned perpendicular to the axis of the first polarizer. The purpose of the first polarizer was two-fold; it reduces the unpolarized background fluorescence by at least 50% and it defines a reference for the proper orientation for the second polarizer.

Upon leaving the polarizers, the beam is then sent through a lens of focal length

$f = 54.6$ cm. The beam waist size and location after propagation through the lens are given by [45]:

$$w_{02} = \sqrt{\frac{w_{01}'^2}{z_{R1}'^2/f^2 + (1 - D/f)^2}} \quad (3.8)$$

where, with $\lambda = 514$ nm,

$$z_{R1}' = \frac{\pi w_{01}'^2}{\lambda} = 1.44 \text{ m},$$

and D , is the distance of the lens from the incident beam waist. Refereing to Fig. 3.4 we find that D is given by

$$D = z_2' + d_1 + d_2 + d_3 = 73.7 \text{ cm} + 50 \text{ cm} + 17 \text{ cm} + 29 \text{ cm} = 1.70 \text{ m}.$$

This give the new beam waist size,

$$w_{02} = 0.137 \text{ mm}$$

and the waist location

$$d_4 = f \left(1 - \frac{1 - D/f}{z_{R1}'/f^2 + (1 - D/f)^2} \right) = 61.7 \text{ cm}.$$

The Rayleigh range of the beam after propagation through l_1 is given by

$$z_{R2} = \frac{\pi w_{02}^2}{\lambda} = 11.5 \text{ cm}.$$

The laser was operated at an output of a few mW for acquisition of the dominant-polarization profiles and about 100mW for recording the cross-polarization component profiles. The CCD camera was placed at varying distances from the beams waist to acquire beam profiles for both the dominant and cross polarization components. Possible methods for observing the longitudinal component were discussed in the introduction. Experimental profiles for the dominant and cross polarization profiles are given in the next section.

3.3 Hermite-Gauss intensity profiles

The profiles for the dominant direction of polarization (x -component) and the fundamental mode profiles (HG_{00}) are not expected to change with propagation, but simply increase in size. On the other hand, it is expected that the cross polarization profiles for higher order modes will change shape with propagation as the beam propagates. As mentioned in section 1.1.1 the Gouy phase is responsible for this change in shape. It can be seen from the experimental profiles, after several Rayleigh ranges the profiles continue to increase in size but the shape seems to stabilize.

The following figures give beam profiles for HG beams up to $N = n + m = 3$. In each set the top row shows the theoretical profiles and the row below shows the experimentally obtained profiles. The experimental images are all shown at 50% of the original size as recorded by the CCD. The theoretical images were scaled to fit the experimental profiles. In doing such scaling the information associated with the absolute beam size with propagation is lost but it allows for a direct comparison of the images and gives a greater appreciation for the alteration the beam undergoes with propagation. In a subsequent section a direct comparison of the experimental and theoretical beam size is made.

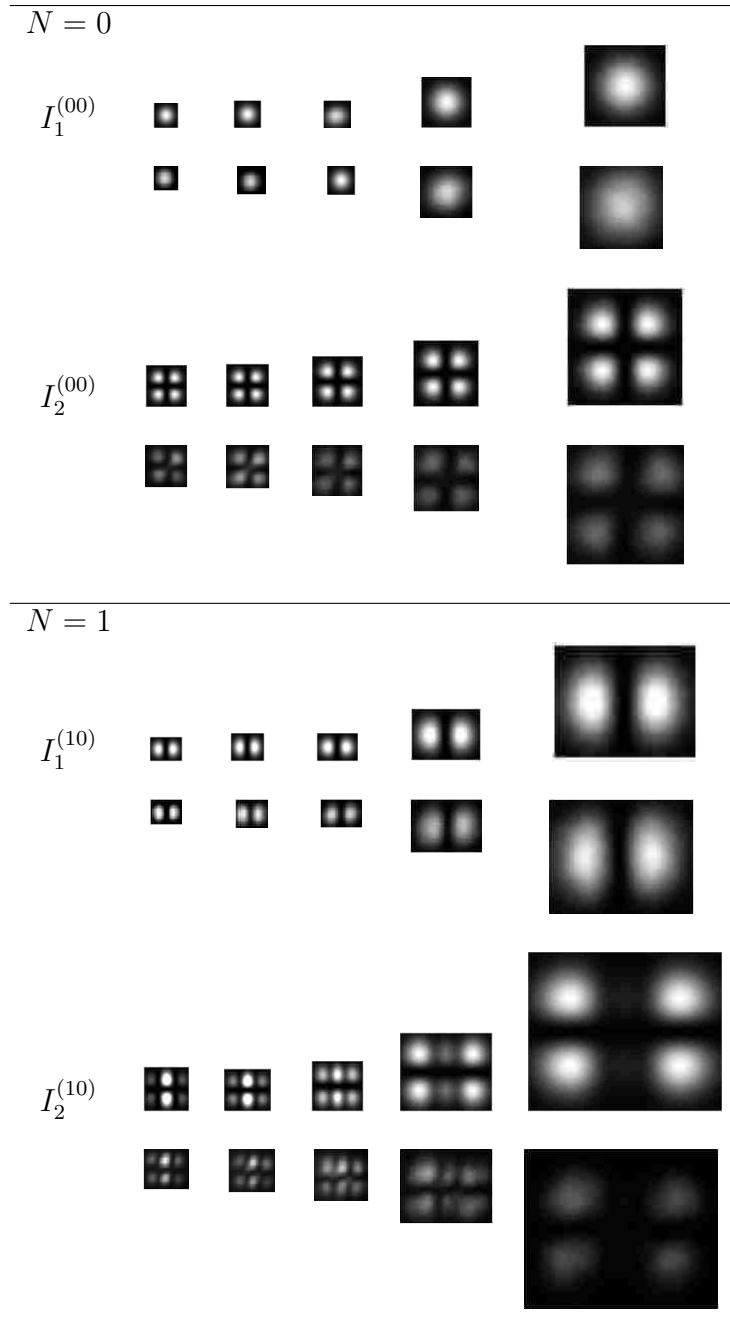


Figure 3.6: Dominant (I_1) and cross-polarization (I_2) components of the fundamental Gaussian beam (HG_{00}) and HG_{10} at $z = 0$, $z = 0.5z_R$, $z = z_R$, $z = z_{2R}$, and $z = 4z_R$.

$N = 2$

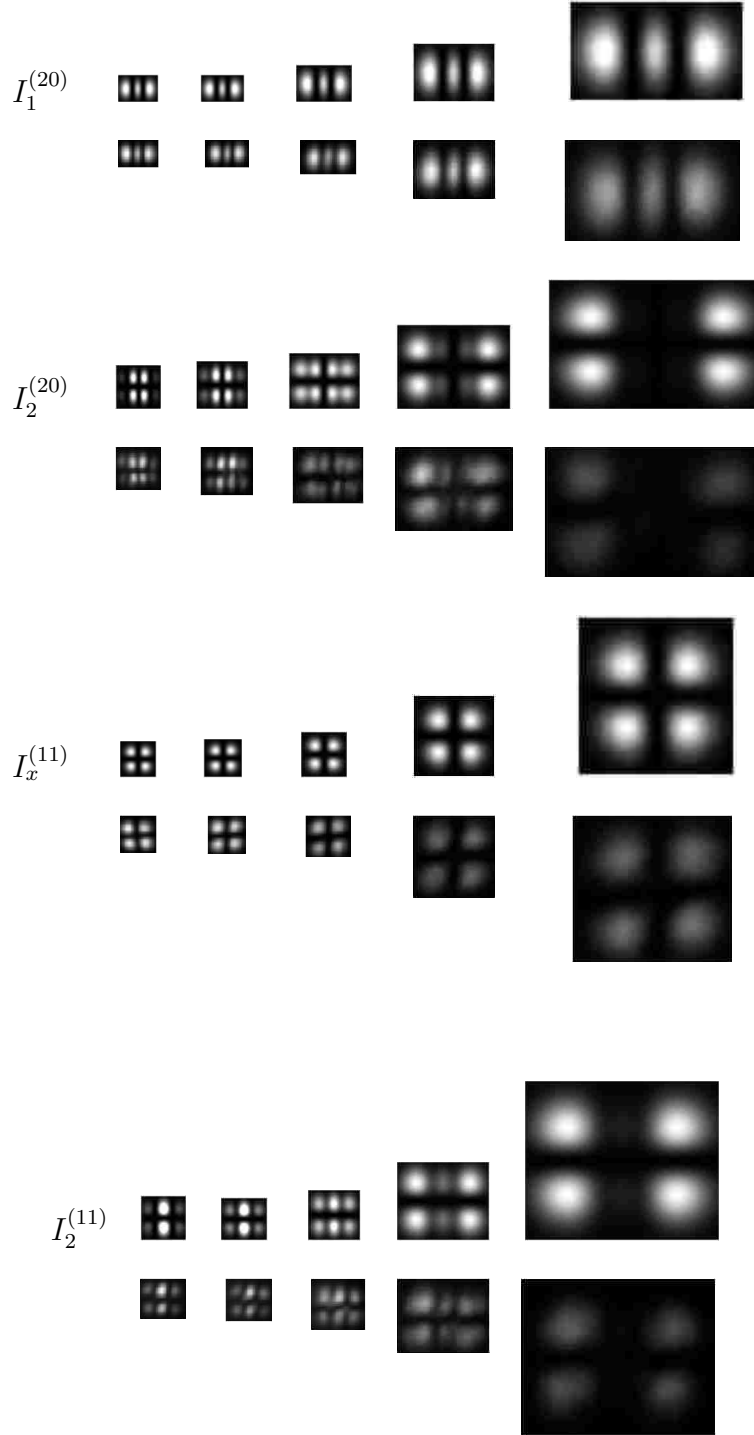


Figure 3.7: Dominant (I_1) and cross-polarization (I_2) components of HG_{20} and HG_{11} at $z = 0$, $z = 0.5z_R$, $z = z_R$, $z = 2z_R$, and $z = 4z_R$.

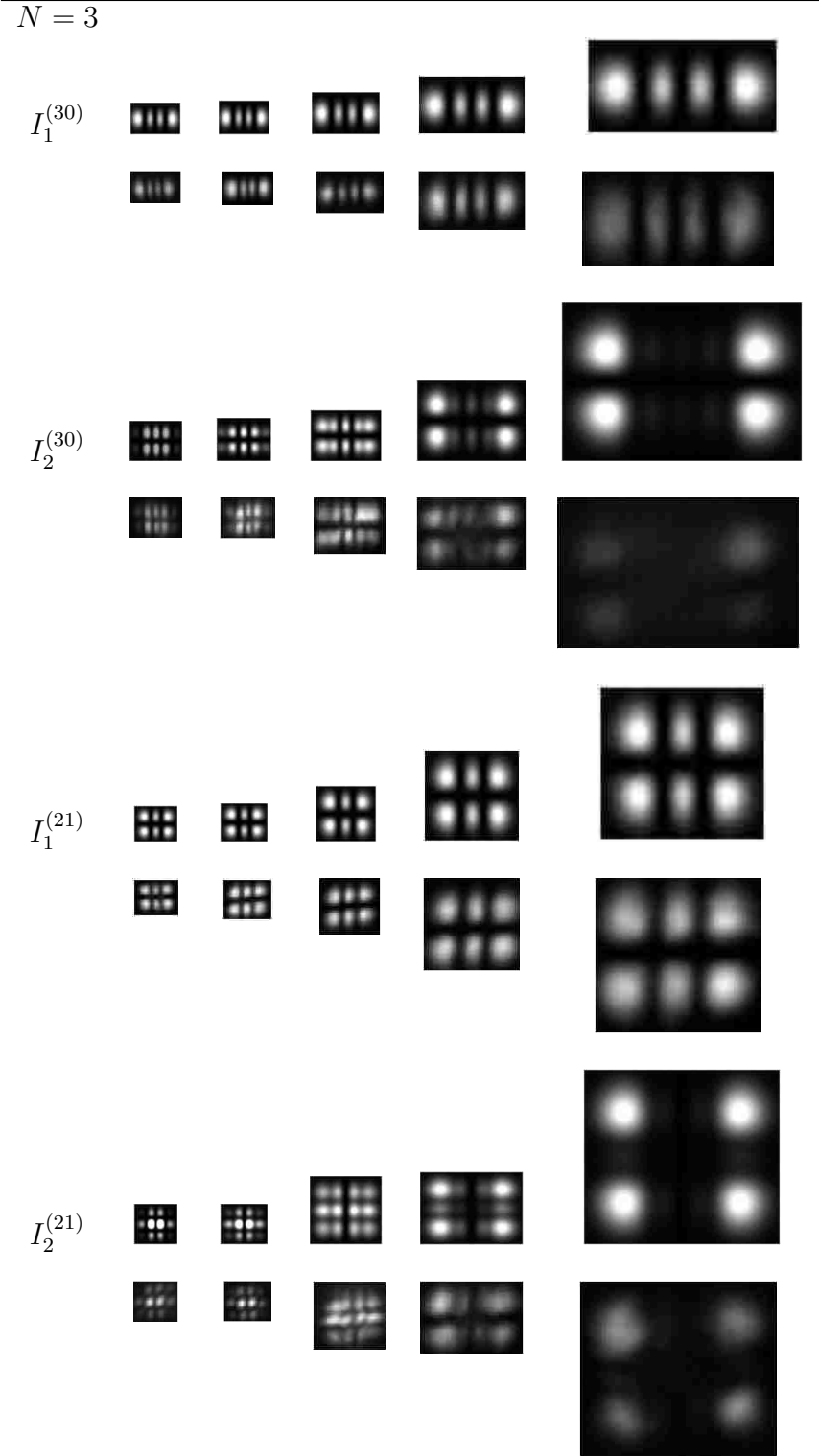


Figure 3.8: Dominant (I_1) and cross-polarization (I_2) components of HG_{30} and HG_{21} at $z = 0$, $z = 0.5z_R$, $z = z_R$, $z = 2z_R$, and $z = 4z_R$.

3.4 Discussion and analysis of results

Both the dominant and cross-polarization component beam profiles of the fundamental HG mode ($N=0$), apart from the increase in beam size, do not change shape with propagation. The change in size with propagation can be thought of as a change in scale of the beam. The increase in the beam spot size is directly due to the distance dependent beam waist size, $w(z)$, given in Chapter 2 Eq. (2.38).

The intensity profiles of the cross-polarization for beams with $N > 0$ have a more interesting evolution with propagation. The dominant-polarization component of higher order modes only undergoes scale change as the fundamental beam. The evolution of the cross-polarization component of the higher-order mode intensity profiles is more substantial. The structure of the cross-polarization component intensity profiles is a function of propagation distance. The change in structure of the cross-polarization components is due to the propagation dependence of the Gouy phase. For instance, consider the dominant and cross-polarization component intensity profiles for $m = 2$ and $n = 0$:

$$I_1^{(20)}(\vec{r}) = \left[\frac{P_0}{\pi w^2(z)} \right] (2X^2 - 1)^2 e^{-(X^2+Y^2)}, \quad (3.9)$$

$$I_2^{(20)}(\vec{r}) = \frac{1}{(kw_0)^4} \left[\frac{P_0}{\pi w^2(z)} \right] X^2 Y^2 \left[(2X^2 - 5)^2 \cos^2 \theta(z) + (2X^2 - 1)^2 \sin^2 \theta \right] e^{-(X^2+Y^2)}, \quad (3.10)$$

where X and Y are scaled transverse coordinates as described in Chapter 2, P_0 is the total power of the beam, k is the magnitude of the wave vector, and $w(z)$ is the radius of the beam. One can see from Eq. (3.9) that the only z dependence is in the beam radius, $w(z)$, which leads to the above described scale change of the beam. On the other hand, in addition to the z dependence present in $w(z)$ in the cross-polarization term, there is an additional z -dependent Gouy phase, $\theta(z)$. This dependence of Gouy phase is responsible for the change in structure of the cross-polarization intensity profiles of higher-order HG beams. As predicted by theory and discussed in Chapter 2 Section 1.3, after a propagation distance of several Rayleigh ranges the intensity profile settles to a

stable structure.

3.4.1 Experimental and theoretical difference analysis (figure of merit)

In order to quantitatively analyze the experimentally attained beam profiles the following difference analysis method was devised and implemented in Matlab (see appendix for code):

1. Crop the experimental Img_e and theoretical images Img_t to a rectangular region of interest that encloses the beam profile.
2. Scale the intensity of the theoretical image to be in the same range as the experimental image. This is accomplished with the *imadjust* command.
3. Resize the theoretical image to be the same number of pixels as the experimental. This is done with the *imresize* command.
4. Once the set of images are the same size they are subtracted from each other,

$$Img_s = |Img_e - Img_t|.$$

5. Since the experimental images have varying intensity ranges and size, due to the fact that as the laser beam propagates it spreads and thus also decreases in intensity, we calculated a figure of merit as follows. We count the number (N_j) of each integer value (j) in Img_s . As an example let

$$Img_s = \begin{pmatrix} 0 & 0 & 0 & 0 & 1 \\ 0 & 0 & 2 & 0 & 1 \\ 0 & 3 & 0 & 2 & 1 \\ 1 & 1 & 2 & 1 & 0 \\ 0 & 3 & 1 & 0 & 1 \end{pmatrix}, \quad (3.11)$$

then $N_1 = 8$, $N_2 = 3$, and $N_3 = 2$.

Then the sum of the products $N_j \times j$ is calculated and divided by the product of the total number of pixels in Img_s (TP) and the maximum pixel value in the experimental image, $max(Img_e)$

$$FM = \frac{1}{max(Img_e) \times TP} \sum_{j=1}^{max_j} j \times N_j. \quad (3.12)$$

FM gives a quantitative figure of merit that characterizes how good the match is between the experimental and theoretical images for each mode and longitudinal distance from the beam's waist. $FM = 1$ indicates the worst possible match and $FM = 0$ a perfect match.

To give a visual appreciation for what results in the subtraction of the theoretical and experimental images, Img_s for a few orders is given in Fig. 3.9. The dark regions in Fig. 3.9 correspond to low intensity pixels, i.e. areas of a good match. The lighter regions correspond to high intensity values, or a poor match. Table 3.1 gives the total weighted difference fractions for all experiment-theory image sets given in Fig. 3.3.

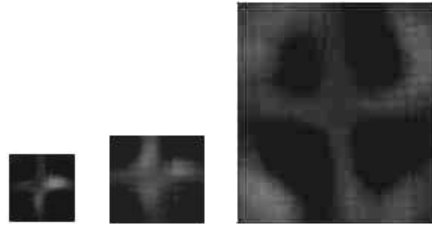


Figure 3.9: Img_s for the fundamental mode at $z = 0$, $z = z_R$, $z = 4z_R$

z/z_R	HG_{00}	HG_{01}	HG_{02}	HG_{03}	HG_{11}	HG_{12}
0	0.055	0.071	0.138	0.098	0.120	0.110
0.5	0.078	0.046	0.051	0.127	0.038	0.037
1	0.088	0.054	0.062	0.072	0.076	0.073
2	0.087	0.051	0.056	0.048	0.034	0.039
4	0.073	0.016	0.054	0.033	0.013	0.011

Table 3.1: Figure of merit values for the Hermite-Gauss intensity profiles.

The left most profile in Fig. 3.9 is the difference of the experimental and theoretical intensity profiles of the fundamental Gaussian beam at its waist. The figure of merit for this set of images is $FM = 0.055$. The difference of the experimental and theoretical intensity profiles of the same beam at $z = z_R$ and $z = 4z_R$ are the middle and right most images in Fig. 3.9 and have figures of merit of $FM = 0.088$ and $FM = 0.073$, respectively. From the three images and these difference values one can get a sense of the effect the size and intensity ranges can have on the figure of merit and the necessity to weight the difference values so that the goodness match of all the images can be compared.

From the figure of merit values it is seen that the of the experimental and theoretical cross-polarization intensity profiles are in reasonable agreement.

Profile size

Since the theoretical intensity profiles presented in Fig. 3.3 are scaled so that they are the same size as the experimental profiles, we will address here the absolute beam size of profiles that the CCD records. Figures 3.10-3.13 give the size of the beam with propagation distance a both the theoretically expected and the experimentally observed growth. The experimental pixel data was found using MatLab by first converting the image to binary with threshold such that all pixels that are within a factor of 0.135 ($\approx 1/e^2$) of the maximum intensity will become 1 and the rest 0. The number of nonzero pixels across the profile in each of the transverse directions is then counted, giving a measured beam size in pixels. The theoretical beam growth is determined using the propagation distance dependent beam size Eq. 2.38,

$$w(z) = w_0 \sqrt{1 + \left(\frac{z}{z_R}\right)^2}. \quad (2.38^*)$$

See Figs. 3.10 and 3.11 for the growth of the cross and dominant-polarization component profiles for the fundamental mode (HG_{00}) and Fig. 3.13 for the growth in the transverse directions for the

HG_{20} mode. The theoretical beam size is scaled so that $w(0)$ is the measured diameter (number of pixels) of the beam at its waist. Unless otherwise stated the diameter is measured across the profile along the x -axis. The fundamental mode (HG_{00}) beam size at the waist is $2w_0 = 0.28$ mm, which corresponds to about 50 pixels.

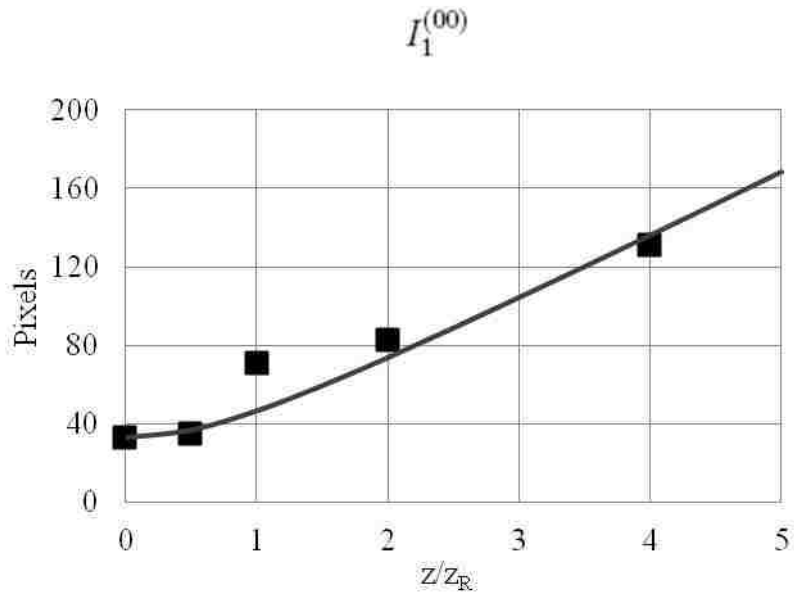


Figure 3.10: Experimental (squares) and theoretical (line) beam diameter (number of pixels) with propagation for the dominant-polarization component of a fundamental Gaussian beam

As can be seen from the plots of the experimental pixel count and the theoretical size in Figs. 3.10-3.13, the growth of the experimentally acquired beam profiles are in good agreement with the theoretically expected growth.

3.4.2 Beam power

According to Eqs. (2.87) and (2.88), the power ratio of the dominant polarization and the cross-polarization component is

$$\frac{P_2}{P_1} = \frac{1}{16(w_0 k)^4}, \quad (3.13)$$

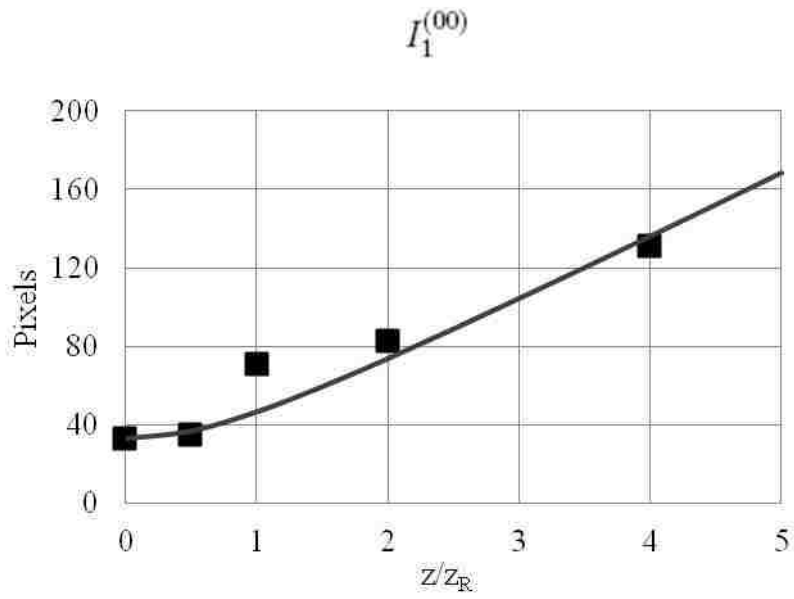


Figure 3.11: Experimental (squares) and theoretical (line) beam diameter (number of pixels) with propagation for cross-polarization component of a fundamental Gaussian beam

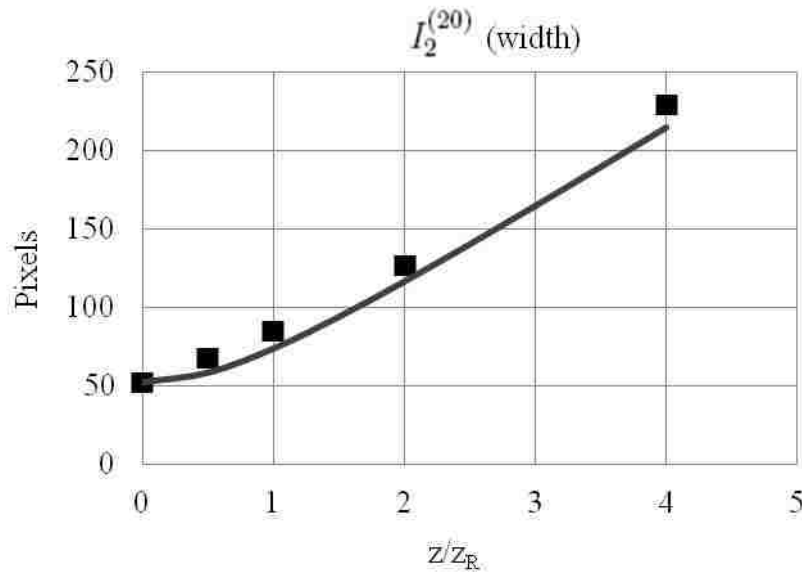


Figure 3.12: Experimental (squares) and theoretical (line) profile diameter (number of pixels) in the x -direction with propagation for the cross-polarization component of a HG_{20} beam in the x -direction.

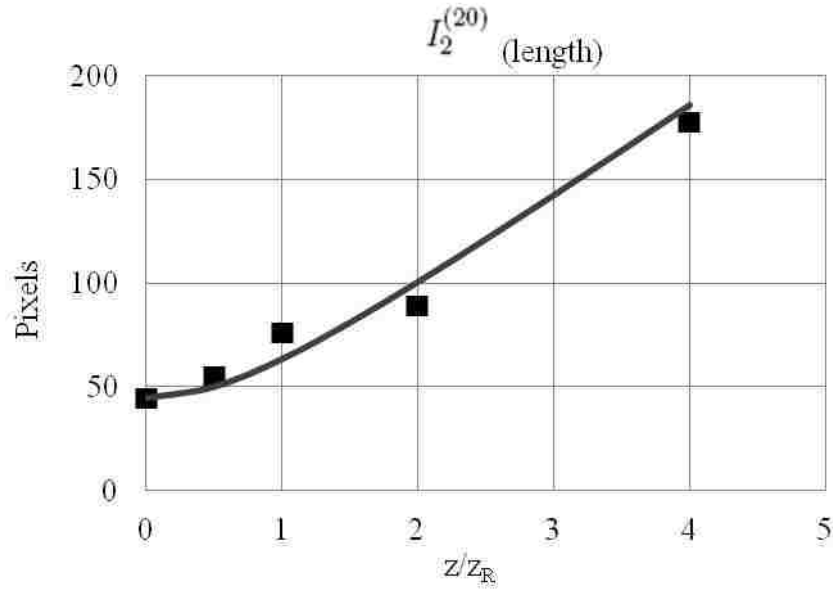


Figure 3.13: Experimental (squares) and theoretical (line) profile diameter (number of pixels) in the y -direction with propagation for the cross-polarization component of a HG_{20} beam.

where $k = 2\pi/\lambda$ with $\lambda = 514\text{nm}$. Therefore, a beam with a spot size of $w_0 = 0.14\text{ mm}$, the power ratio of the beam prior to the second polarizer and after the polarizer should be $P_2/P_1 \approx 10^{-14}$. Here we present measured power data. The power is measured after the first polarizer (P_1), whose axis is parallel to the polarization axis of the beam emitted from the laser, and after the second polarizer (P_2) with its axis both perpendicular and parallel to the first polarizer, see Fig. 3.4.2.

The slope of the best fit line of the data in Fig. 3.14, found using a linear least squares regression, gives the power ratio P_2/P_1 with polarizers parallel is found to be about 0.5. The slope of the best fit line of the data in Fig. 3.4.2 gives the ratio of the power of P_2 parallel to P_1 and P_2 perpendicular to P_1 is on the order of 10^{-5} . The beam profiles for the cross polarization component are still observed, as expected from theory, because after the second polarizer the other term (I_1^{nm}) is 10^{-14} smaller than the, now dominant, term (I_2^{nm}).

The extinction ratio, which is the ratio of the power of a plane-polarized beam transmitted through a

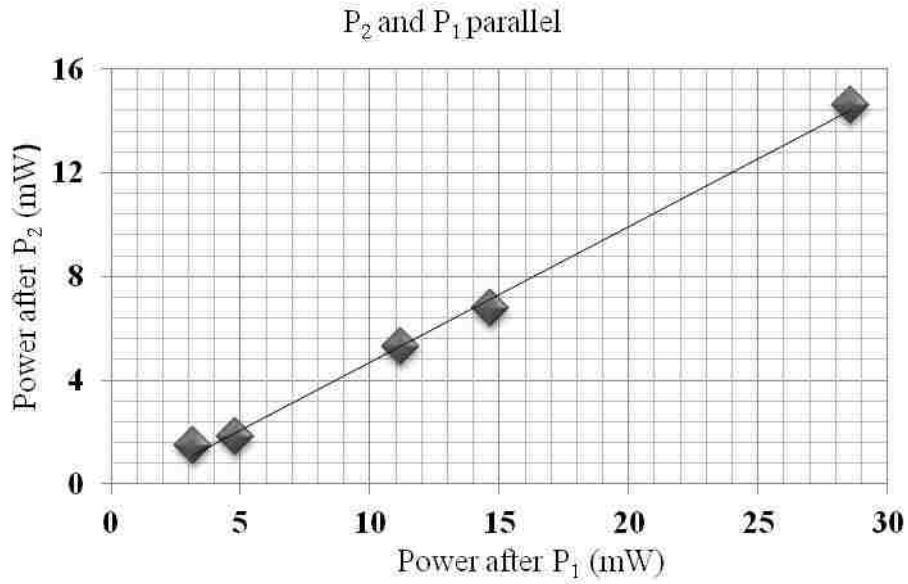


Figure 3.14: Beam power after the first polarizer versus the power after the second polarizer for the polarizers parallel to each other.

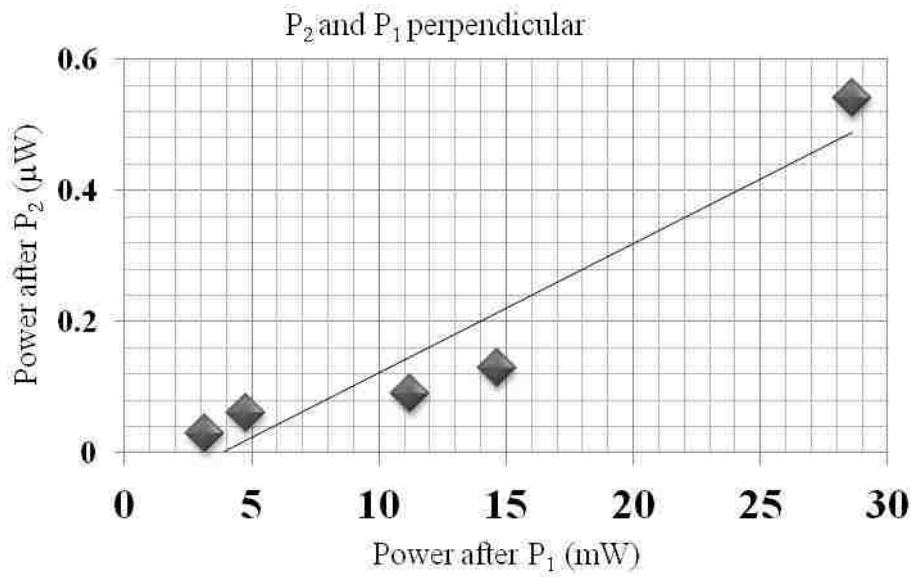


Figure 3.15: Beam power after the first polarizer versus the power after the second polarizer for the polarizers perpendicular to each other.

polarizer with with polarizer's axis parallel to the dominant direction of polarization as compared with the transmitted power when the polarizer's axis is perpendicular the dominant direction of

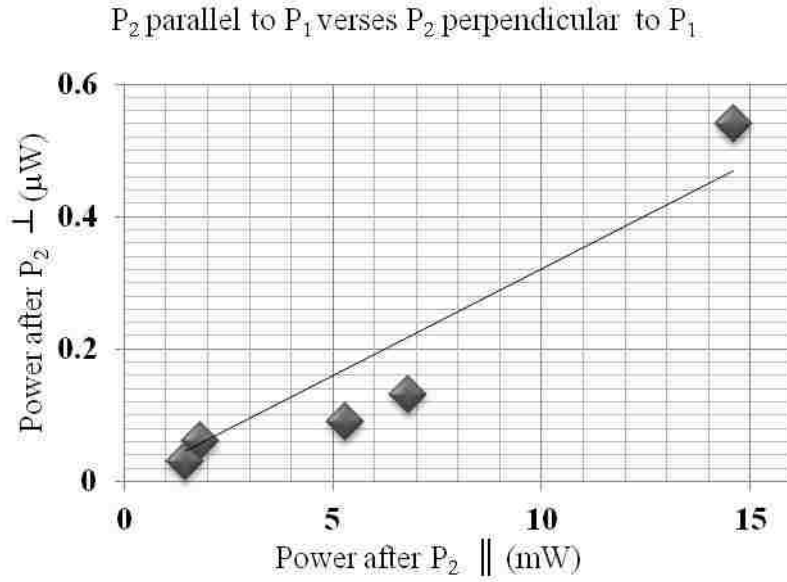


Figure 3.16: Beam power after the second polarizer with its axis parallel to the first verses the power after the second polarizer with its axis perpendicular to the first.

polarization, specified by the manufacturer of the polarizers is 10^{-4} . We are not limited by this specification. Careful alignment led to an order of magnitude decrease in the extinction ratio (10^{-5}) but is still nine orders of magnitude larger than the expected power ratio of the dominant and cross-polarization terms. Despite the relatively large observed power of the cross-polarization component of the beam, compared to the expected power, the experimentally observed intensity profiles are in agreement with the expected profiles. This discrepancy can be explained by considering that the polarizers are only suitable for a certain range of wavelengths, i.e. the UV radiation will not be polarized. Additionally, the fluorescence from the laser is unpolarized therefore the first polarizer only blocks half of the incident fluorescence. The fluorescence does not have a definite shape so while it contributes to the total power of the beam it has no effect on the shape of the intensity profile.

3.5 Chapter summary

In summary, in this chapter we have discussed the generation of higher-order Hermite-Gaussian laser beams. We have presented the theoretical and experimental intensity profiles for the dominant and cross-polarization components of HG beams up to $N = 3$, the transverse profile of the cross-polarization component undergoes an observable evolution with propagation that stabilizes after a few Rayleigh ranges. We have presented a method to quantify the shape congruence of the two. The comparison of the expected and observed beam evolution with propagation are in reasonable agreement.

Chapter 4

Linearly Polarized Laguerre-Gauss Laser Beams

This chapter gives the method used to generate Laguerre-Gauss laser beams. A discussion of the working principles of the mode converter used to transform Hermite-Gauss modes into Laguerre-Gauss modes is given. Additionally, the experimental setup and experimentally recorded profiles and their comparison with theoretical beam profiles are also presented in this chapter.

4.1 Relation between Hermite-Gauss and Laguerre-Gauss beams

We begin by discussing the mathematical connection between Hermite-Gauss and Laguerre-Gauss beams which will give insight into the working of the mode converter used in the experiment to generate Laguerre-Gauss beams. We note that Laguerre-Gauss and Hermite-Gauss beams both form a complete set of solutions to the paraxial wave equation. Therefore, we should be able to write one set of modes as a superposition of the other set of modes. In particular, we can write the Laguerre modes in terms of Hermite modes with appropriate real coefficients and phase factors. This relation between the Laguerre-Gauss modes and Hermite-Gauss modes is given by [32,77,78]

$$E_{nm}^{LG}(x, y, z) = \sum_{k=0}^N i^k b(n, m, k) E_{N-k,k}^{HG}(x, y, z), \quad (4.1)$$

where $b(n, m, k)$ are real coefficients given by

$$b(n, m, k) = \left(\frac{(N-k)!k!}{2^N n!m!} \right)^{1/2} \frac{1}{k!} \frac{d^k}{dt^k} [(1-t)^n (1+t)^m] |_{t=0}. \quad (4.2)$$

$$E_{nm}^{LG} = \frac{2w_0}{w(z)} \left(\frac{\sqrt{2}r}{w(z)} \right)^{|n-m|} L_{\min(m,n)}^{|n-m|} \left(\frac{2r^2}{w^2(z)} \right) e^{-i(m+n+1)\theta(z) + ikr^2/2q(z) + i|n-m|\phi}, \quad (4.3)$$

where $r = \sqrt{x^2 + y^2}$ and

$$E_{nm}^{HG}(x, y, z) = \frac{w_0}{w(z)} H_m \left(\frac{\sqrt{2}x}{w(z)} \right) H_n \left(\frac{\sqrt{2}y}{w(z)} \right) \times e^{i(m+n+1)\theta(z) + \frac{ik(x^2+y^2)}{2q(z)}}. \quad (4.4)$$

Here the index $N = n+m$ is introduced and is referred to as the order of the mode. The coefficients $b(n, m, k)$ for $N = 1$ to 4 are given in Table 4.1.

We also use the relation expressing the Hermite-Gauss modes rotated at 45° with respect to the x, y (a diagonal mode) in terms of Hermite-Gauss modes with respect to the x, y [32, 73],

$$E_{nm}^{HG} \left(\frac{x+y}{\sqrt{2}}, \frac{x-y}{\sqrt{2}}, z \right) = \sum_{k=0}^N b(n, m, k) E_{N-k,k}^{HG}(x, y, z), \quad (4.5)$$

where $b(n, m, k)$ are the same real coefficients as in Eq. (4.1) and given by Eq. (4.2). It is seen that the diagonal Hermite modes form the same set as the Laguerre modes with one key difference; the expression in Eq. (4.5) does not have, the i^k term that appears in Eq. (4.1). A mode decomposition for HG_{02} is shown visually in Fig. 4.2. Eqs. (4.1) and (4.5) suggest that to generate a Laguerre-Gauss it is necessary to merely decompose a Hermite-Gauss mode into its components and introduce a phase difference of i^k between successive terms. This phase difference in successive terms can be realized by taking advantage of the Gouy phase.

4.1.1 Mode converter

In this section, we will discuss the mode converter that is used in the experiment to convert Hermite-Gauss modes into Laguerre-Gauss modes of the same order. The principle of the mode converter is based on the Gouy phase possessed by Gauss beams. The Gouy phase was introduced in section 2.1. This type of mode converter has been widely used in literature: [15, 32, 65, 79, 80].

	n	m	$k = 0$	1	2	3	4
$N = 0$	0	0	1				
$N = 1$	0	1	$\frac{1}{\sqrt{2}}$	$\frac{1}{\sqrt{2}}$			
	1	0	$\frac{1}{\sqrt{2}}$	$-\frac{1}{\sqrt{2}}$			
$N = 2$	0	2	$\frac{1}{2}$	$\frac{1}{\sqrt{2}}$	$\frac{1}{2}$		
	1	1	$\frac{1}{\sqrt{2}}$	0	$-\frac{1}{\sqrt{2}}$		
	2	0	$\frac{1}{2}$	$-\frac{1}{\sqrt{2}}$	$\frac{1}{2}$		
$N = 3$	0	3	$\frac{1}{\sqrt{8}}$	$\sqrt{\frac{3}{8}}$	$\sqrt{\frac{3}{8}}$	$\frac{1}{\sqrt{8}}$	
	1	2	$\sqrt{\frac{3}{8}}$	$\frac{1}{\sqrt{8}}$	$-\frac{1}{\sqrt{8}}$	$-\sqrt{\frac{3}{8}}$	
	2	1	$\sqrt{\frac{3}{8}}$	$-\frac{1}{\sqrt{8}}$	$-\frac{1}{\sqrt{8}}$	$\sqrt{\frac{3}{8}}$	
	3	0	$\frac{1}{\sqrt{8}}$	$-\sqrt{\frac{3}{8}}$	$\sqrt{\frac{3}{8}}$	$-\frac{1}{\sqrt{8}}$	
$N = 4$	0	4	$\frac{1}{4}$	$\frac{1}{2}$	$\frac{\sqrt{6}}{4}$	$\frac{1}{2}$	$\frac{1}{4}$
	1	3	$\frac{1}{2}$	$\frac{1}{2}$	0	$-\frac{1}{2}$	$-\frac{1}{2}$
	2	2	$\frac{\sqrt{6}}{4}$	0	$-\frac{1}{2}$	0	$\frac{\sqrt{6}}{4}$
	3	1	$\frac{1}{2}$	$-\frac{1}{2}$	0	$\frac{1}{2}$	$-\frac{1}{2}$
	4	0	$\frac{1}{4}$	$-\frac{1}{2}$	$\frac{\sqrt{6}}{4}$	$-\frac{1}{2}$	$\frac{1}{4}$

Table 4.1: The coefficients $b(n,m,k)$

The mode converter can be understood by considering Fig. 4.1. This figure shows the shape of the beam as it passes through its waist. It possesses the typical Gauss profile and has the same shape in both the x and y directions.

As noted above we require a i^k phase difference between the successive components of Hermite modes, rotated at 45° , to be introduced so that a Laguerre mode can be generated. Consider a lower

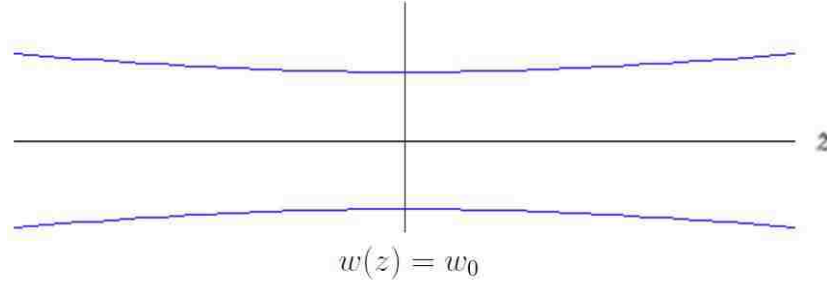


Figure 4.1: Beam shape near waist

order mode, HG_{02} mode rotated at 45° to the (x, y) axis. The diagonal mode can be written as

$$\begin{aligned}
 E_{02}^{HG}\left(\frac{x+y}{\sqrt{2}}, \frac{x-y}{\sqrt{2}}, z\right) &= \sum_{k=0}^2 b(0, 2, k) E_{2-k, k}^{HG_1}(x, y, z) \\
 &= \frac{1}{2} E_{20}^{HG} + \frac{1}{\sqrt{2}} E_{11}^{HG} + \frac{1}{2} E_{02}^{HG}.
 \end{aligned} \tag{4.6}$$

This decomposition is represented pictorially in Fig. 4.2. The decomposition of the Laguerre-

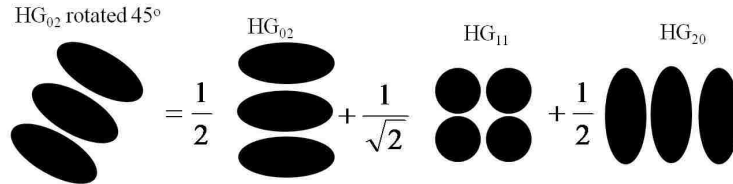


Figure 4.2: Pictorial example of the decomposition of the diagonal HG_{02} mode.

Gauss mode of the same order is represented pictorially in Fig. 4.3. Mathematically, the decom-

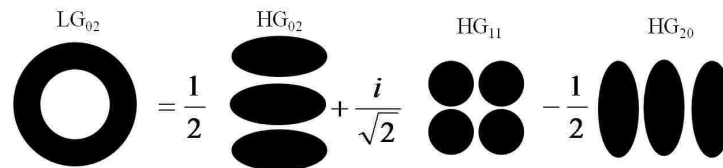


Figure 4.3: Pictorial example of the decomposition of the LG_{02} mode.

position of LG_{02} is given by,

$$\begin{aligned}
 E_{02}^{LG}\left(\frac{x+y}{\sqrt{2}}, \frac{x-y}{\sqrt{2}}, z\right) &= \sum_{k=0}^2 b(0, 2, k) E_{2-k, k}^{HG_1}(x, y, z) \\
 &= \frac{1}{2} E_{20}^{HG_1} + \frac{i}{\sqrt{2}} E_{11}^{HG_1} - \frac{1}{2} E_{02}^{HG_1}.
 \end{aligned} \tag{4.7}$$

From Figs. 4.2 and 4.3, the diagonal HG_{02} mode is a superposition of the same modes for a LG_{02} beam without a phase difference of i^k between terms. Our task now is to find a solution to the problem of introducing this i^k phase between successive terms in a diagonal Hermite-Gauss mode so that a Laguerre-Gauss mode is generated.

A phase difference can be introduced if the Rayleigh range in the y direction (z_{Ry}) is changed over a localized region while the Rayleigh range in the x direction (z_{Rx}) is unchanged. This local astigmatism is introduced by placing a pair of cylindrical lenses in the beam path. The first lens must be placed such that the Rayleigh range in one transverse direction of the beam changes but the waist location and Rayleigh range in the other transverse direction does not. If the first lens is placed a distance d from the beam waist the second lens must be located a distance $2d$ from the first lens on the other side of the waist so that the astigmatism is removed outside the lens set. This is shown in Fig. (4.4). Note that the cylindrical lenses cause the astigmatism only between the two lenses (localized astigmatism).

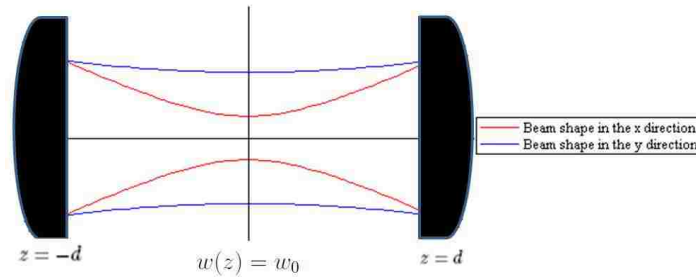


Figure 4.4: Beam shape between the two cylindrical lenses of mode converter

We are now left to find the proper cylindrical lens separation, d , location of the lens set, and the Rayleigh range of the incoming beam such that there is astigmatism only between the lenses. We start by assuming the transverse shape of the beam to be circular at the cylindrical lenses, $z = \pm d$ [32, 46, 79]:

$$w_x(\pm d) = w_y(\pm d). \quad (4.8)$$

With the equation for the beam size, $w(z)$,

$$w^2(z) = \frac{2(z_R^2 + z^2)}{kz_R}, \quad (4.9)$$

we have

$$\frac{z_{R_x}^2 + d^2}{z_{R_x}} = \frac{z_{R_y}^2 + d^2}{z_{R_y}}. \quad (4.10)$$

To find z_{R_x} and z_{R_y} we need an additional relationship between the two. This relationship can be found by considering the radius of curvature of the beam. The radius of curvature of the beam before and after the first cylindrical lens of focal length f_c is related by

$$\frac{1}{f_c} = \frac{1}{R_1} - \frac{1}{R_2}, \quad (4.11)$$

where R_1 is the radius of curvature of the beam prior to the propagating through the first cylindrical lens and R_2 is the radius of curvature after the lens. The lens, being cylindrical, will only change the radius of curvature in the y direction leaving the radius of curvature in the x direction ($R_x(-d)$ and $R_x(d)$) unchanged, additionally the radius of curvature in the x and y directions will be the same before the first cylindrical lens. Therefore

$$R_y(-d) = R_x(-d) \quad (4.12)$$

and

$$R_x(-d) = R_x(d). \quad (4.13)$$

Combining with Eq. (4.11) we have

$$\frac{1}{f_c} = \frac{1}{R_y(-d)} - \frac{1}{R_y(d)} = \frac{1}{R_x(d)} - \frac{1}{R_y(d)}, \quad (4.14)$$

where d and $-d$ are as indicated in Fig 4.4. Combining

$$R(z) = \frac{z_R^2 + z^2}{z} \quad (4.15)$$

with Eq. (4.14) we have

$$\frac{1}{f_c} = \frac{d}{z_{R_x}^2 + d^2} - \frac{d}{z_{R_y}^2 + d^2}. \quad (4.16)$$

Solving Eqs. (4.10) and (4.16) for z_{R_x} and z_{R_y} we find

$$z_{R_x} = d \sqrt{\frac{1 - d/f_c}{1 + d/f_c}}, \quad (4.17)$$

and

$$z_{R_y} = d \sqrt{\frac{1 + d/f_c}{1 - d/f_c}}. \quad (4.18)$$

Equations (4.17) and (4.18) give the required Rayleigh ranges in the x and y directions. The next task it to find the proper lens separation and the Rayleigh ranges in terms of the focal length of the cylindrical lens, f_c . First, consider that the Gouy phase, which has two contributions, one for each of the transverse directions [45]:

$$(n + m + 1)\theta(z) = \left(n + \frac{1}{2}\right)\theta_x(z) + \left(m + \frac{1}{2}\right)\theta_y(z), \quad (4.19)$$

where $\theta(z)$ is the Gouy phase and given by Eq. (2.72). θ_x and θ_y are given by

$$\theta_{x,y} = \arctan \left[\frac{z}{z_{R_{x,y}}} \right]. \quad (4.20)$$

As the beam propagates from the first cylindrical lens to the second it will experience a difference

in the Gouy phase given by

$$\begin{aligned}
\Delta\theta &= \left(n + \frac{1}{2}\right) \theta_x(d) + \left(m + \frac{1}{2}\right) \theta_y(d) \\
&\quad - \left(n + \frac{1}{2}\right) \theta_x(-d) - \left(m + \frac{1}{2}\right) \theta_y(-d) \\
&= \left(n + \frac{1}{2}\right) \Delta\theta_x + \left(m + \frac{1}{2}\right) \Delta\theta_y.
\end{aligned} \tag{4.21}$$

Here

$$\Delta\theta_{x,y} = \theta_{x,y}(d) - \theta_{x,y}(-d) = 2 \arctan \left(\frac{d}{z_{R_{x,y}}} \right). \tag{4.22}$$

The phase difference between successive terms in the series for diagonal modes Eq. (4.5) is given by:

$$\begin{aligned}
\Theta &= (N + 1)(\Delta\theta_x + \Delta\theta_y)/2 + (N - 2k)(\Delta\theta_x + \Delta\theta_y)/2 \\
&\quad - (N + 1)(\Delta\theta_x + \Delta\theta_y)/2 - (N - 2(k + 1))(\Delta\theta_x + \Delta\theta_y)/2 \\
&= (\Delta\theta_x - \Delta\theta_y) \\
&= 2 \left[\arctan \left(\frac{d}{z_{Rx}} \right) - \arctan \left(\frac{d}{z_{Ry}} \right) \right]
\end{aligned} \tag{4.23}$$

Since a phase difference of i between successive terms is required, and the phase term as given in Eq. (4.4) is

$$e^{-i(m+n+1)\theta(z)} = e^{-i(N+1)\theta(z)}, \tag{4.24}$$

it is necessary for $\Theta = \pi/2$:

$$\Theta = 2 \left[\arctan \left(\sqrt{\frac{1 + d/f_c}{1 - d/f_c}} \right) - \arctan \left(\sqrt{\frac{1 - d/f_c}{1 + d/f_c}} \right) \right] = \pi/2, \tag{4.25}$$

where we have used Eqs. (4.17) and (4.18). Let

$$\eta = \sqrt{\frac{1 - d/f_c}{1 + d/f_c}}, \tag{4.26}$$

and we can rewrite Θ as

$$\Theta = \left[\arctan \left(\frac{1}{\eta} \right) - \arctan (\eta) \right] = \frac{\pi}{4}. \quad (4.27)$$

Taking the *tan* of both sides:

$$\tan \left\{ \left[\arctan \left(\frac{1}{\eta} \right) - \arctan (\eta) \right] \right\} = \tan \left(\frac{\pi}{4} \right),$$

or

$$\frac{\tan \left[\arctan \left(\frac{1}{\eta} \right) \right] - \tan \left[\arctan (\eta) \right]}{1 + \tan \left[\arctan \left(\frac{1}{\eta} \right) \right] \tan \left[\arctan (\eta) \right]} = 1$$

$$\frac{1}{\eta} - \eta = 2. \quad (4.28)$$

Solving for η we find

$$\eta = -1 \pm \sqrt{2}, \quad (4.29)$$

where only the positive solution is physically meaningful. Putting Eq. (4.26) in for η we have

$$\sqrt{\frac{1 + d/f_c}{1 - d/f_c}} = \sqrt{2} - 1. \quad (4.30)$$

Solving for Eq. (4.30) d , we find the required lens separation is given by

$$d = \frac{f_c}{\sqrt{2}}. \quad (4.31)$$

Combining Eqs. (4.18) and (4.31) we find that the Rayleigh range in terms of the focal length of the cylindrical lens is given by

$$z_{Ry} = f_c \left(1 + \frac{1}{\sqrt{2}} \right). \quad (4.32)$$

A spherical lens will be used so that the beam will have the Rayleigh range given in Eq. (4.32). Here we will find the proper placement and focal length of such a lens following the method used by Kogelnik and Li [46]. Let the original beam waist be located a distance d_1 to the left of the lens and the beam waist after the lens, w_{02} be a distance d_2 to the right, as shown in Fig. (4.5).

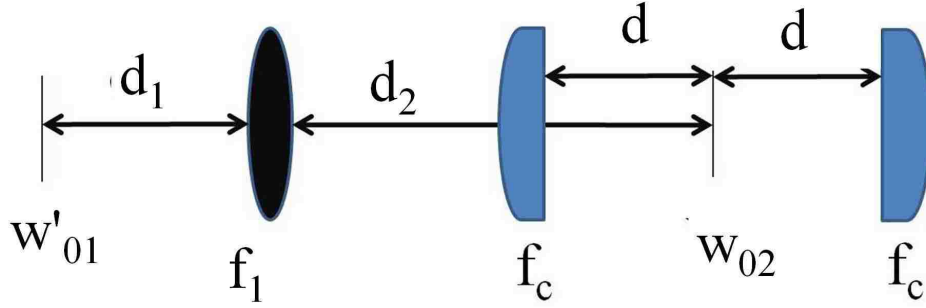


Figure 4.5: Astigmatic mode converter used in this research for Hermite-Gauss to Laguerre-Gauss mode conversion.

The ABCD matrix for the above described system is given by [45],

$$\begin{pmatrix} A & B \\ C & D \end{pmatrix} = \begin{pmatrix} 1 & d_2 \\ 0 & 1 \end{pmatrix} \begin{pmatrix} 1 & 0 \\ -\frac{1}{f_1} & 1 \end{pmatrix} \begin{pmatrix} 1 & d_1 \\ 0 & 1 \end{pmatrix} \quad (4.33)$$

$$= \begin{pmatrix} 1 - \frac{d_2}{f_1} & d_1 + d_2 - \frac{d_1 d_2}{f_1} \\ -\frac{1}{f_1} & 1 - \frac{d_1}{f_1} \end{pmatrix} \quad (4.34)$$

Using the ABCD law:

$$q_2 = \frac{q_1 A + B}{q_1 C + D}. \quad (4.35)$$

The q 's will be purely imaginary and given by $q_1 = i\pi w'_{01}/\lambda$ and $q_2 = i\pi w_{02}/\lambda$. We have

$$\frac{i\pi w_{02}^2}{\lambda} = \frac{1 - \frac{d_2}{f_1} (i\pi w'_{01}/\lambda) + d_1 + d_2 + d_1 d_2 / f_1}{(-i\pi w'_{01}/\lambda) 1 + 1 - d_1 / f_1}, \quad (4.36)$$

and by equating the real and imaginary parts we have

$$\frac{\pi w_{01}^2}{\lambda} \left(1 - \frac{d_1}{f_1}\right) = \left(1 - \frac{d_2}{f_1}\right) \frac{\pi w_{01}'^2}{\lambda},$$

or

$$\frac{w_{01}'}{w_{02}} = \frac{(d_1 - f_1)}{(d_2 - f_1)}, \quad (4.37)$$

and

$$\frac{\pi^2}{\lambda^2 f_1} w_{01}'^2 w_{02}^2 = d_1 + d_2 - \frac{d_1 d_2}{f_1}$$

or, with $f_0 = \pi w_{01}' w_{02} / \lambda$,

$$f_1^2 - f_0^2 = (d_1 - f_1)(d_2 - f_1). \quad (4.38)$$

Simplifying we arrive at

$$d_1 = f_1 \pm \frac{w_{01}'}{w_{02}} \sqrt{f_1^2 - f_0^2} \quad (4.39)$$

$$d_2 = f_1 \pm \frac{w_{02}}{w_{01}'} \sqrt{f_1^2 - f_0^2}, \quad (4.40)$$

giving the proper lens placement of the mode matching lens. Here we must choose either both plus or minus signs but it is desirable to have positive d_1 and d_2 . By placing the spherical lens a distance d_1 from the original beam waist and the cylindrical lens a distance d_2 from the center of the cylindrical lens set, the proper Raleigh range can be achieved, as shown in Fig. 4.5. The separation of the cylindrical lenses is given by Eq. (4.31):

$$d = \frac{f_c}{\sqrt{2}}. \quad (4.41)$$

4.2 Experimental arrangement

We used an *astigmatic mode converter* [15, 32, 79], described in the preceding section, to convert a Hermite-Gauss beam into a Laguerre-Gauss beam of the same order. A schematic of the experimental setup used to generate Laguerre-Gauss modes and observe linearly polarized beam profiles is shown in Fig. 4.6.

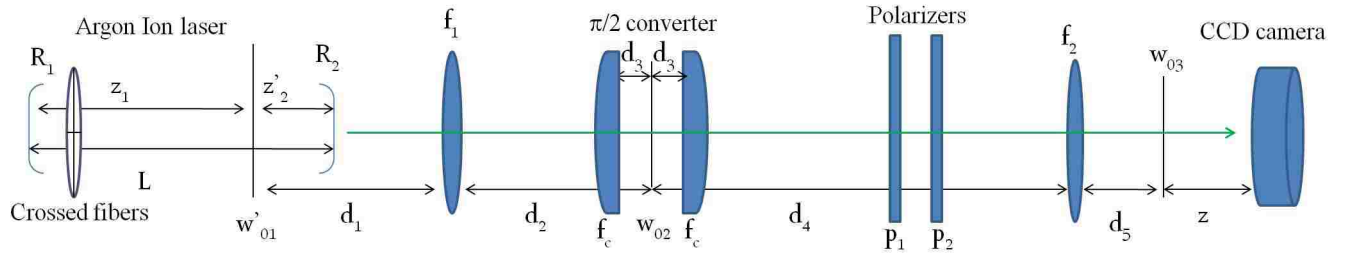


Figure 4.6: Laguerre-Gauss Experimental setup

The beam size and waist location of the beam emitted from the laser is calculated in the same way as for the Hermite-Gauss beam in Chapter 3, section 2. The initial spot size and waist location is different than the value calculated in the previous chapter as a different laser was used to acquire the Laguerre-Gauss profiles due to failure of the original laser. The values corresponding to the distances and focal lengths given in Fig. 4.6 are given in table 4.2. Due to space restrictions on the optics table the focal length of the first lens, f_1 , is chosen such that the cylindrical lenses available could be utilized and an appropriate Rayleigh range could be achieved. As discussed in Chapter 2, the beam profiles of the cross-polarization components are expected to stabilize after several Rayleigh ranges. Therefore, a Rayleigh range is deemed appropriate if a distance $z = 5z_R$ will fit on the table. Accordingly, the focal length of the first lens, f_1 , is chosen for convenience with the stipulation that a reasonable final Rayleigh range, z_{R3} is obtained. The distance d_4 is also chosen for convenience so that several Rayleigh ranges would fit on the table. The location of the beam waist after propagation through the first lens is given by Eq. (4.39) and d_2 is given by Eqs. (4.40).

The cylindrical lenses are separated by a distance

$$2d = \sqrt{2}f_c, \quad (4.42)$$

where f_c is the focal length of the cylindrical lens. The waist size between the cylindrical lenses is given by

$$w_{02} = \sqrt{\frac{\lambda z_{R_2}}{\pi}}, \quad (4.43)$$

where

$$z_{R_2} = \left(1 + \frac{1}{\sqrt{2}}\right) f_c. \quad (4.44)$$

The Rayleigh ranges are given by

$$z_{R_j} = \frac{w_{0j}^2 \pi}{\lambda}, \quad (4.45)$$

where $j = 1, 2, 3$.

$R_1 = 3 \text{ m}$	$R_2 = 3 \text{ m}$	$L = 1.16 \text{ m}$	$w'_{01} = 0.41 \text{ mm}$
$f_1 = 55 \text{ cm}$	$f_2 = 14.5 \text{ cm}$	$f_c = 15 \text{ cm}$	$z'_2 = 70 \text{ cm}$
$d_1 = 90.8 \text{ cm}$	$d_2 = 63.5 \text{ cm}$	$d = 10.6 \text{ cm}$	$d_4 = 18.6 \text{ cm}$
$w_{02} = 0.20 \text{ mm}$	$z_{R_2} = 25.6 \text{ cm}$	$w_{03} = 0.082 \text{ mm}$	$z_{R_3} = 4.1 \text{ cm}$

Table 4.2: Values corresponding to Fig. 4.6.

4.2.1 Alignment considerations

After production of high-quality Hermite-Gauss beams, proper alignment of the $\pi/2$ mode converter is of considerable importance in generating high-quality Laguerre-Gauss beams. Given a pure HG mode, an ideal mode converter can theoretically create LG beams with 100% efficiency [65]. As discussed in the previous chapter, a high quality HG beam is generated intracavity with the inclusion of a fiber or a pair of crossed fibers and a pair of slits to select single higher-order mode operation.

Proper alignment of the astigmatic mode converter is a multi-step procedure. The first alignment is to ensure that the beam is propagating parallel to the optics table. Once this is achieved placement of the lenses can begin. The cylindrical lenses are mounted in lens holders that allow azimuthal rotation as well as linear translation in each of the transverse directions. Normal incidence of the beam at the center of the cylindrical lens is assured if, upon rotation of the lens, the reflection of the beam from the lens rotates in a uniform circular manner centered at the incident beam. This is observed by placing an aperture on the incident side of the lens and rotating the lens, once the center of the lens is placed roughly normal to the beam, fine adjustments are made in the tilt and in the transverse directions until the reflection rotates circularly around the aperture center. Note that after a change in HG mode selection in the laser cavity there is a slight shift in the direction of the laser beam causing minor adjustments be made for each LG mode. Not only must great care be taken to arrange that the beam goes through the center of each lens and at normal incidence to the lenses but also placing the lenses at the proper distances from the waist is paramount. To aid in the later issue, the mode matching lens and the cylindrical lens mounts are placed on translators that allow relatively smooth longitudinal displacement. After placing the lenses in the approximately correct location based on the calculations described in Chapter 2 and the cylindrical lenses have the correct alignment small translational adjustments are made until the highest possible symmetry of the output mode is achieved, as observed on the CCD.

The alignment considerations of the polarizers are the same for the Laguerre-Gauss modes as that of those Hermite-Gauss modes discussed in Chapter 3.

4.3 Intensity profiles

Both the theoretical and experimental beam profiles of the cross and dominant-polarization components of Laguerre-Gauss beams with $p = 0$ and $\ell = 1, 2, 3, 4$ are given in Figs. 4.7, 4.8, 4.9, and 4.11, $(\ell, p) = (0, 1)$ and for $(\ell, p) = (1, 1)$ are given in Figs. ?? and 4.10. I_1 corresponds to the dominant-polarization component intensity profile and I_2 is the cross-polarization component intensity profile. The laser is operated at about 5-10 mW to obtain the dominant-polarization profiles and 150-200 mW to obtain the cross-polarization profiles. The theoretical images are scaled to fit the experimental profiles. As in the case of the HG beam profiles, we discuss the growth of the size of the beam separately from the evolution of the profiles with propagation.

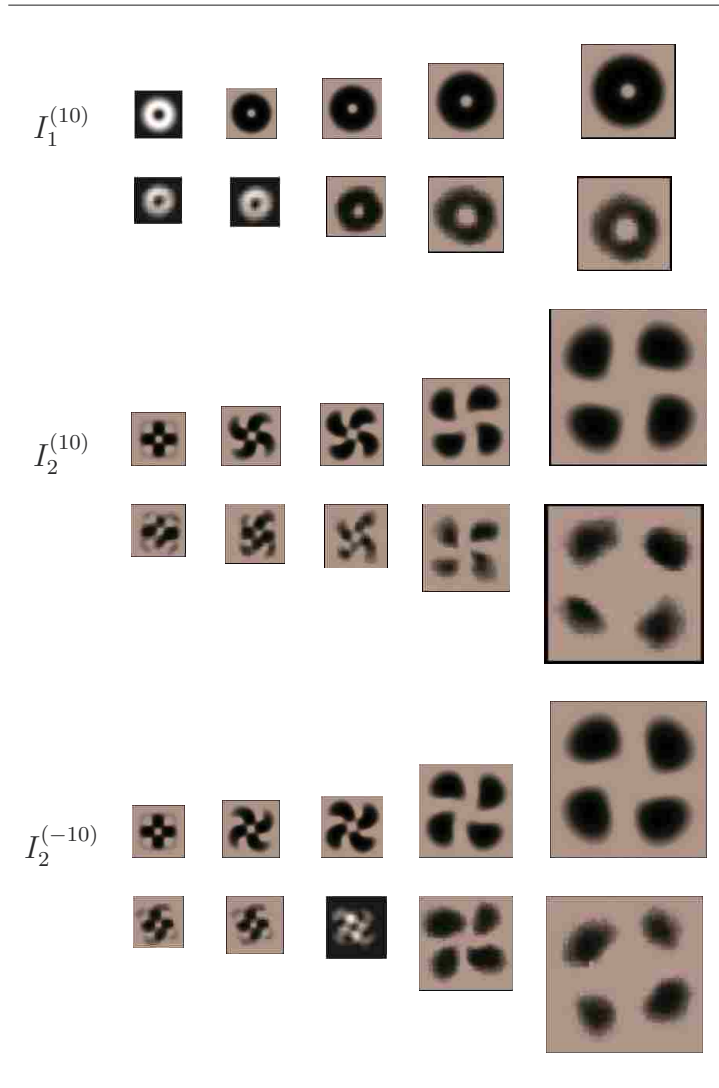


Figure 4.7: Dominant (I_1) and cross-polarization (I_2) intensity profiles for LG beams with $\ell = \pm 1$ and $p = 0$, at $z = 0$, $z = \frac{1}{2}z_R$, $z = z_R$, and $z = 4z_R$. The dominant-polarization intensity profile for $\ell = -|\ell|$ is the same as the $\ell = +|\ell|$ profile.

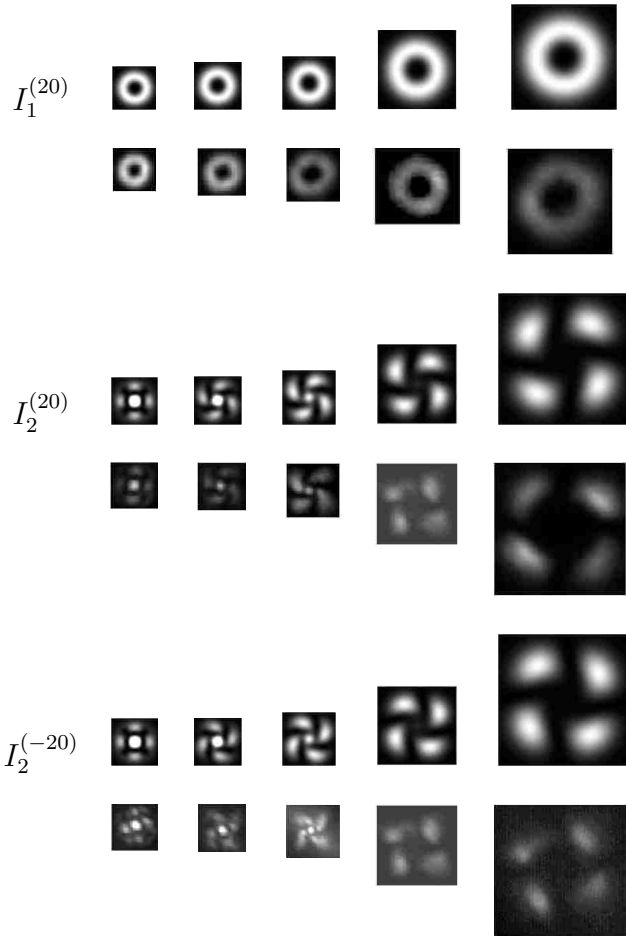


Figure 4.8: Dominant (I_1) and cross-polarization (I_2) intensity profiles for LG beams with $\ell = \pm 2$ and $p = 0$, at $z = 0$, $z = \frac{1}{2}z_R$, $z = z_R$, and $z = 4z_R$. The dominant-polarization intensity profile for $\ell = -|\ell|$ is the same as the $\ell = +|\ell|$ profile.

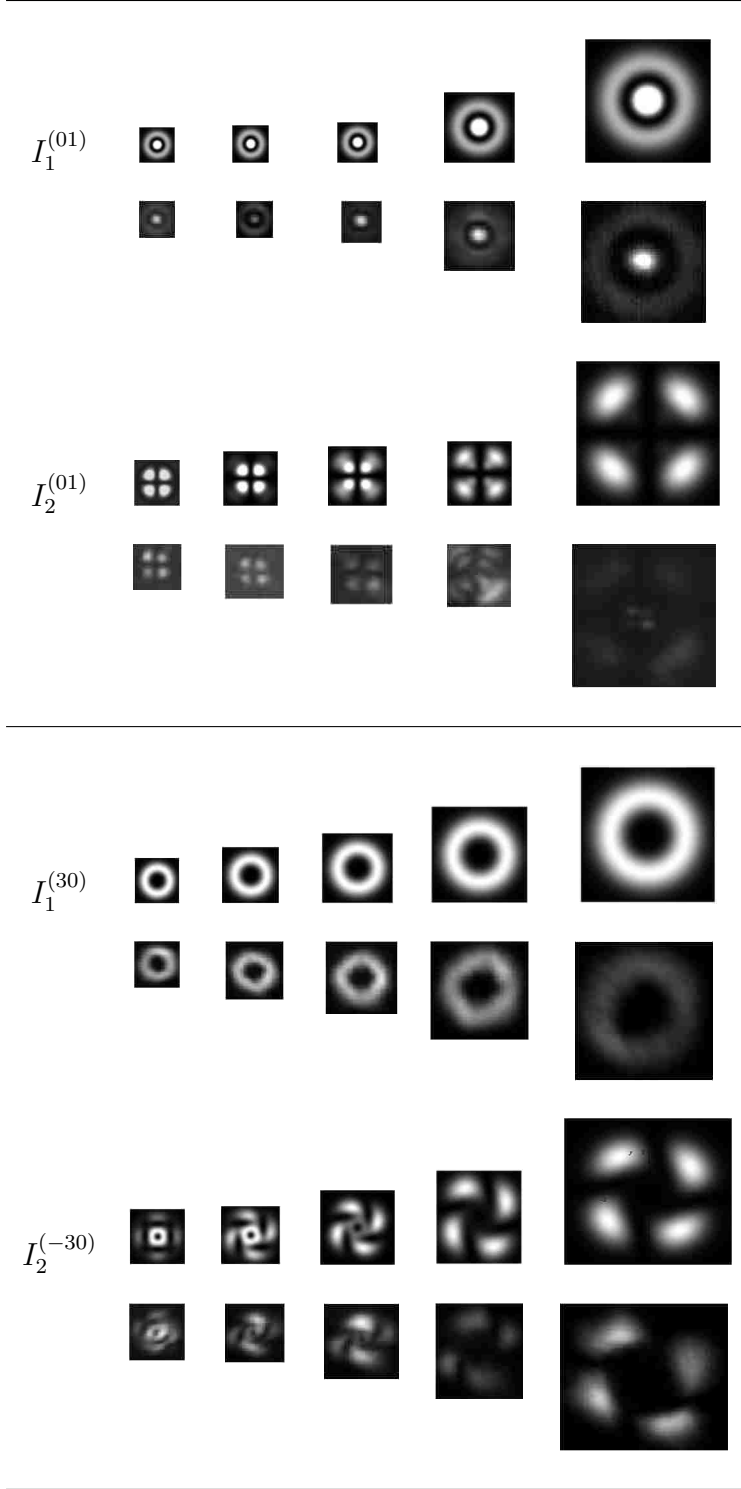


Figure 4.9: Dominant (I_1) and cross-polarization (I_2) intensity profiles for LG beams with $(\ell, p) = (0, 1)$, and $(\ell, p) = (\pm 3, 0)$ at $z = 0$, $z = \frac{1}{2}z_R$, $z = z_R$, and $z = 4z_R$. The dominant-polarization intensity profile for $\ell = -|\ell|$ is the same as the $\ell = +|\ell|$ profile.

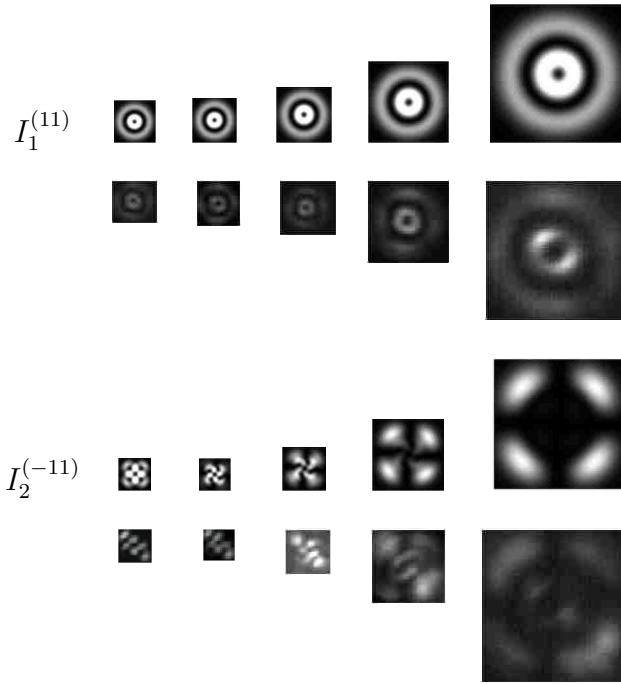


Figure 4.10: Dominant (I_1) and cross-polarization (I_2) intensity profiles for an LG beam with $\ell = -1$ and $p = 1$, at $z = 0$, $z = \frac{1}{2}z_R$, $z = z_R$, and $z = 4z_R$. The dominant-polarization intensity profile for $\ell = -|\ell|$ is the same as the $\ell = +|\ell|$ profile.

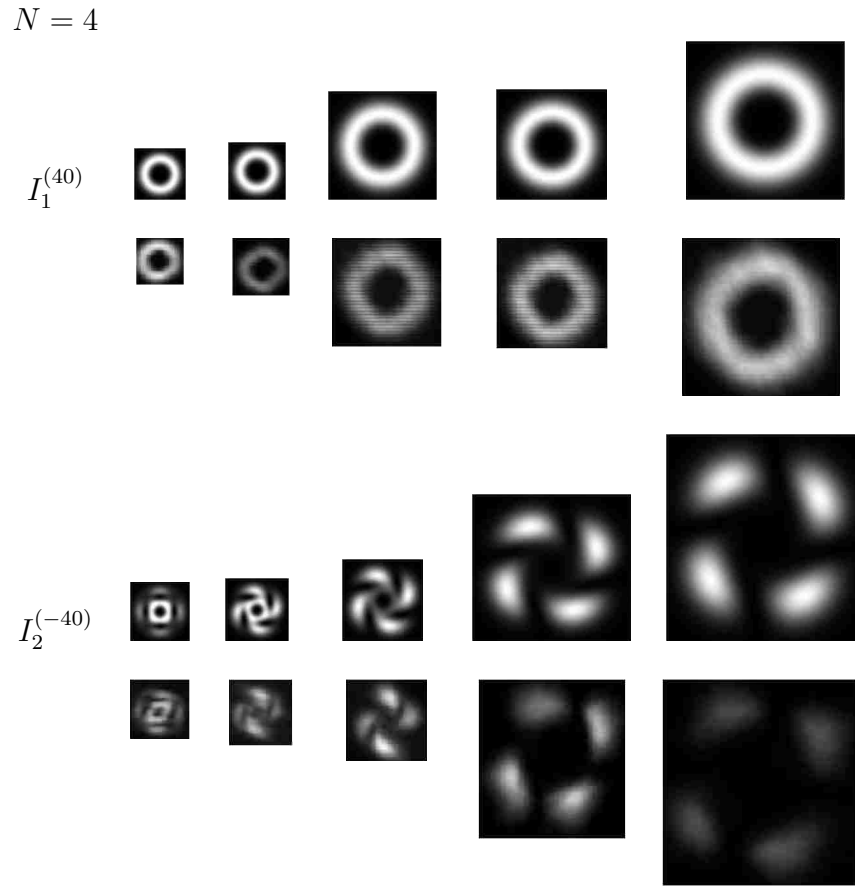


Figure 4.11: Dominant (I_1) and cross-polarization (I_2) intensity profiles for LG with $\ell = \pm 4$ and $p = 0$, at $z = 0$, $z = \frac{1}{2}z_R$, $z = z_R$, and $z = 4z_R$. The dominant-polarization intensity profile for $\ell = -|\ell|$ is the same as the $\ell = +|\ell|$ profile.

The shape of the dominant polarization profiles are not affected by propagation. Conversely, All of the cross-polarization intensity profiles have a four fold symmetry in the near field that rotates as they propagate away from their waist, after several Rayleigh ranges the profiles stabilize to a four lobed patterns.

4.4 Results and Discussion

Here we consider the difference between the theoretical and experimental cross-polarization profiles. Similar to the HG modes, the cross-polarization components of the intensity profiles change shape with propagation while the dominant-polarization profiles only undergo a change in scale. The the cross-polarization components of the LG intensity profiles rotate with propagation. This rotation is analytically examined in this section.

4.4.1 Rotation of the cross-polarization profiles

First, we examine the rotation that the cross-polarization profiles go through during propagation [14]. It should be noted that beams with $\ell = 0$ do not exhibit rotation (Fig. 4.9). We begin the discussion of rotation by introducing δ , the angle of rotation of the cross-polarization profiles. The angle δ is defined as the angle between the radius vector from the center of the beam to the center of a lobe to the horizontal axis, as shown in Fig. 4.12.

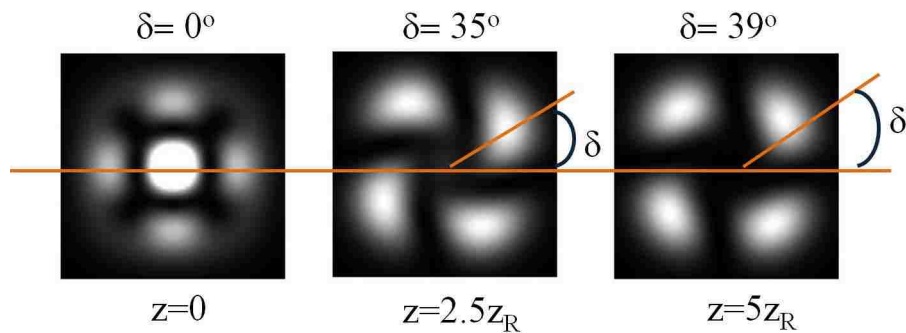


Figure 4.12: Define angle of rotation, δ .

The rotation of the profiles readily be can be observed in Figs. 4.7, 4.8, and 4.10-4.11. The angle of rotation is measured via a Matlab program (see appendix for code, `LG.rotate.m`) for both experimental and theoretical profiles. The procedure for determining δ is as follows,

1. Crop: The edge of the intensity profile is determined and the intensity profile is cropped to the region of interest.
2. Find locations of maximum intensity: The built-in function *find(max)* is used to locate the maximum intensity of the lobes in the theoretical profiles. To find the location of maximum intensity of the lobes in experimental profiles it is necessary to first reduce the noise in the profiles. This is achieved by converting the grey-scale experimental images to binary using the maximum threshold for the conversion that allows the remaining regions of each lobe to remain connected.
3. Centroid of the lobe: The *regionprops* command is then used to find the location of the maximum of each lobe in the experimental profiles.
4. Knowing the location of each of the maxima and the center of the entire profile the angle of rotation is readily calculated.

Note that finding the largest possible threshold for the binary conversion, in the second step, allows for the smallest uncertainty in the locations of maximum intensity. This is seen by considering a theoretical image, the location of the maximum intensities of the blades is well defined. By increasing the threshold level one observes that the location of the center of the blade (of the binary image) approaches the location of the maximum intensity.

A graph of the rotation results are given in Fig. 4.13, experimental data are given as points and the theoretical data is given as a line. Each experimental point is the average of at least six different sets of data. The experimental data is in reasonable agreement with the theoretical data. The change in the Laguerre-Gauss cross-polarization profiles change little after several Rayleigh ranges.

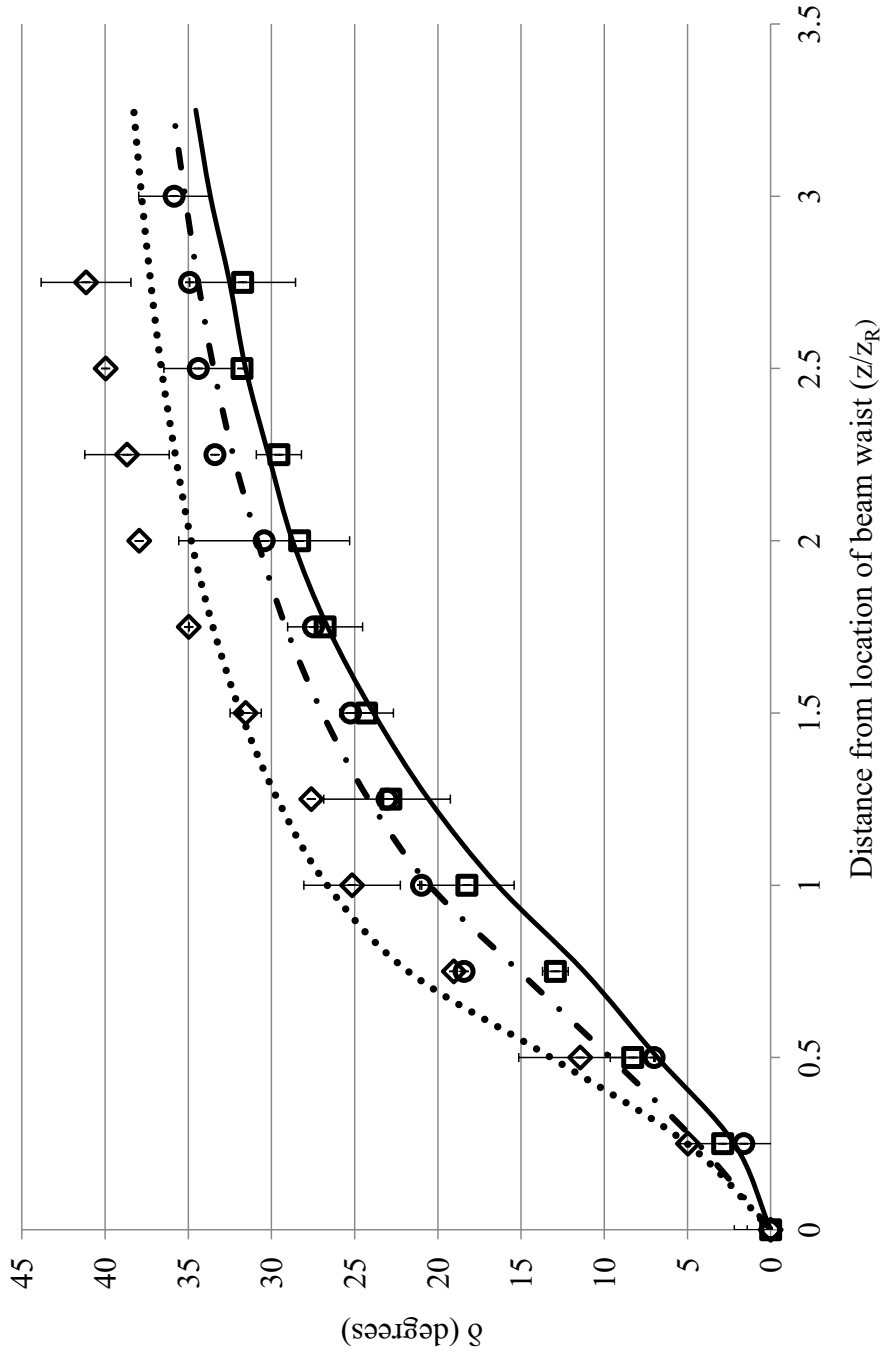


Figure 4.13: Angle of rotation, δ , of the cross-polarization component with propagation distance z/z_R . Where $\diamond \equiv LG_{10}$ experiment, $\circ \equiv LG_{20}$ experiment, $\square \equiv LG_{30}$ experiment, $\dots \equiv LG_{10}$ theory, $-\cdot-\cdot-$ $\equiv LG_{20}$ theory, $- - -$ $\equiv LG_{10}$ theory, and solid line $\equiv LG_{30}$ theory.

It is also interesting to note that the beam profile rotates slower for higher azimuthal index, ℓ . Fig. 4.14 gives the angle of rotation with respect to ℓ , in agreement with Vyas et. al [72]. Once again, the experimental and theoretical data are in reasonable agreement with each other.

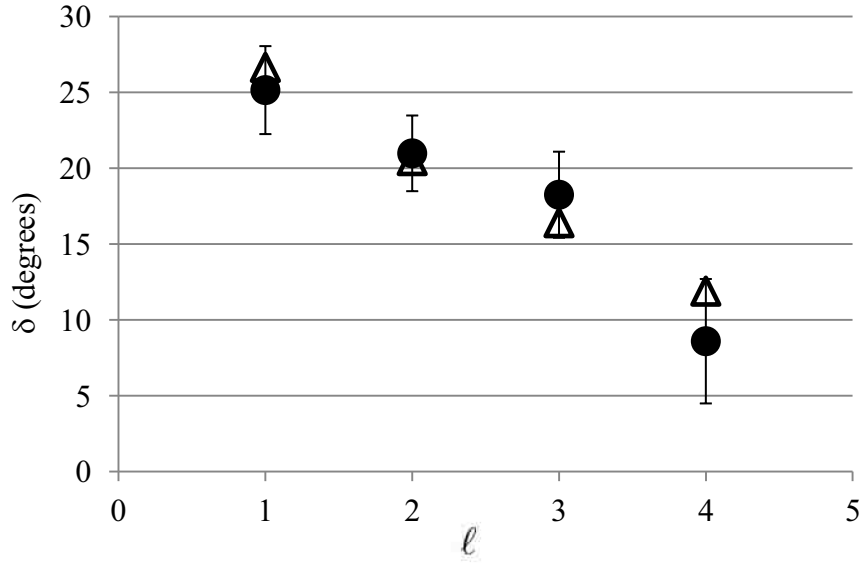


Figure 4.14: Angle of rotation, δ , at $z = z_R$ as a function of l for $p = 0$.

Another very interesting property is evident when the cross-polarization profiles for polarized beams of different topological charge, $\pm\ell$, of the same order, are compared, see the second and third rows Figs. 4.7 and 4.8. The cross-polarization profile for beams with $\ell = -|\ell|$ rotates counter-clockwise with propagation, conversely the beams $\ell = +|\ell|$ rotates in the clockwise direction with propagation. This property can be explained by considering the fact that changing the sign of the topological charge (ℓ), effectively, interchanges the x and y axes, causing the change in direction of rotation. Another way to make this change in chirality conspicuous is to realize that there is two primary ways that one can change the sign of ℓ , the first is to use a dove prism which, when inserted in to the LG beam path, changes the transverse profile of the output beam to the mirror image of the transverse profile of the input beam. Another way to change the sign of ℓ is

to change the HG beam to be converted to the LG beam from HG_{nm} to HG_{mn} , that is rotate the angle between the HG beam and the mode converter axis by 90° . Either of the options described facilitate an *exchange* of x and y coordinates leading to a change in the direction of helicity of the LG beam. There is no visible change of the dominant polarization profiles for different charges of ℓ .

4.4.2 Figure of merit of observed intensity profiles

In order to quantify how closely the experimentally recorded LG profiles match the theoretically expected profiles, the same algorithm as described in Chapter 3 to analyze the HG beam profiles is used. Table 4.3 gives the figure of merit for the cross-polarization components of the LG beam profiles, at different distances from the beam waist.

z/z_R	LG_{10}	LG_{20}	LG_{30}	LG_{40}
0	0.103	0.101	0.109	0.123
0.5	0.077	0.095	0.060	0.068
1	0.068	0.114	0.050	0.070
2	0.102	0.167	0.072	0.001
4	0.064	0.164	0.034	0.016

Table 4.3: Figure of merit (FM).

Again, $FM = 0$ corresponds to perfect agreement and $FM = 1$ no agreement. The results of the difference data indicate that the experimental profiles are in good agreement with the theoretical ones, as is evident in Figs. 4.7-4.11.

4.4.3 Beam growth

The theoretical intensity profiles presented in Figs. 4.7-4.11 are scaled so that they are the same size as the experimental profiles causing beam growth as a function of distance data to be lost. Here we give size of the beam profiles that the CCD records in number of pixels as a function of

distance from the waist. Figures 4.15 and 4.16 give the size of the beam with propagation distance for both the theoretically expected and the experimentally observed growth. The theoretical and experimental spot size data is retrieved by following the same procedure as for the Hermite-Gauss beams described in Chapter 3. Figure 4.15 shows the growth of the dominant-polarization component profile for the LG_{10} mode and Fig. 4.16 for the growth of LG_{30} mode with propagation.

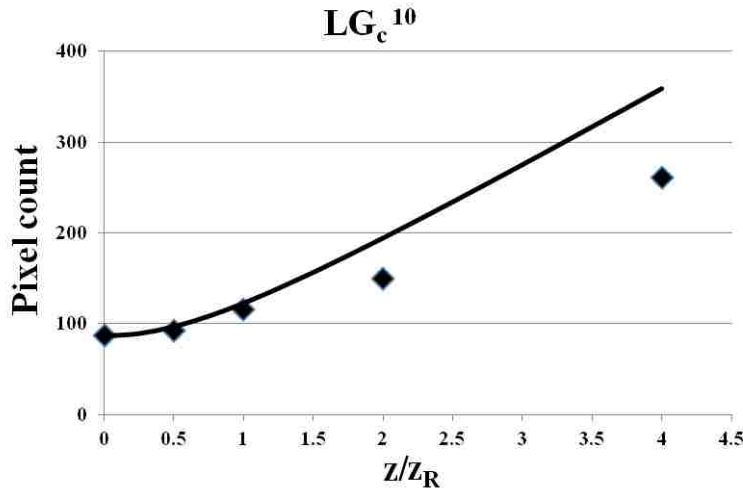


Figure 4.15: Beam size growth with propagation for the cross-polarization component of LG_{10} . The diamonds are experimental results and theoretically expected results are drawn as a continuous curve.

As can be seen from the plots given in Figs. 4.15 and 4.16 the experimentally measured beam growth data is in reasonable agreement with the theoretically expected growth.

4.5 Chapter summary

This chapter discusses the astigmatic mode converter and the principles behind how it converts HG beams to LG beams of the same order and alignment considerations specific to this research. Generation of LG modes and acquisition of the intensity profiles of dominant and cross-polarization components profiles is discussed. Experimental profiles for several orders of LG beams were presented and compared to the theoretical profiles. The two show reasonable agreement. The in-

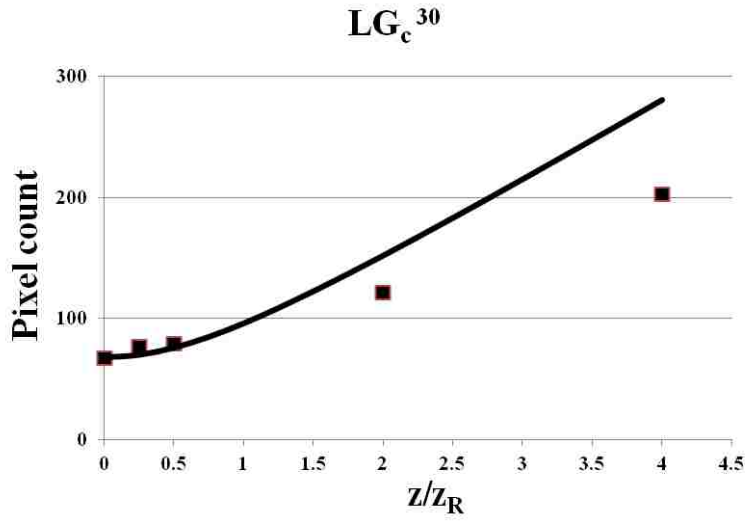


Figure 4.16: Beam size growth with propagation for the cross-polarization component of LG_{30} . The squares are experimental results and theoretically expected results are drawn as a continuous curve.

Interesting rotational behavior of the cross-polarization component of LG beams for nonzero ℓ was discussed. The rotation is found to be slower for larger values of ℓ . The rotation is in opposite directions for different topological charges, $\pm\ell$. The experimental rate of rotation is in good agreement with the theoretical data.

Chapter 5

Conclusions

5.1 Summary

This thesis presents a description of laser beams consistent with Maxwell's equations. Such beams are examples of wave-like electromagnetic disturbance that have a dominant direction of propagation their extent in directions transverse to the direction of propagation is finite. As the beam propagates, it retains the dominant direction of propagation but its transverse extent changes. Laser beams thus have an intermediate status between a plane wave, which has a definite direction of energy flow but infinite extent and a spherical wave where energy flows uniformly in all directions. Since laser beams are electromagnetic radiation, electric and magnetic fields associated with them must satisfy not only the wave equation but also the Maxwell's equations. Only such a description will correctly describe their propagation characteristics including their focusing and polarization properties. Although for many applications it is adequate to describe laser beams in terms of an electric field that can be written as a constant vector multiplied by a scalar function which is a solution of scalar wave equation. This description is termed scalar approximation. It is clear that a scalar description assumes that beam polarization is uniform. Such a description can account for overall energy transport but it cannot account for focusing or defocusing of laser beams as they propagate and, as we have shown in this thesis, it also fails to properly describe the polarization properties of laser beams. We have shown that a correct description of laser beams emerges only when we insist that the electric and magnetic field associated with laser beams satisfy not only the wave equation but also the Maxwell's equations. We show that in order to satisfy Maxwell's equations, the electric field of a linearly polarized laser beam must have three non-zero field com-

ponents. It should be recalled that wave like solutions with more than one electric field components are well known in waveguides. This is a consequence of boundary conditions that must be satisfied by the field components. This thesis shows that even in free-space, with no boundaries present, the correct description of laser beams leads to an electric field that has all three Cartesian components nonzero. This means that beams with uniform polarization do not exist. However, if one particular component of the electric field is dominant and the other two are weak, we can still speak of a beam linearly polarized in the direction of the dominant component. Similarly, we can speak of a left circularly (or right circularly) polarized beam if the beam has a dominant left circular polarization component and a weaker longitudinal and cross-polarization (right circular in this case) components. Since a circularly polarized wave can be considered to be a coherent super-position of two orthogonal linearly polarized wave, we have confined our attention to linear polarization in this thesis. We have considered two families of laser beams - linearly polarized Hermite-Gauss (HG) and Laguerre-Gauss (LG) beams - and derived expressions for the electric field components of these beams.

Theoretical derivation leading to the expressions for the field components of linearly polarized HG and LG beams was given in Chapter 2. The chapter begins by introducing the conventionally used scalar description of laser beams in the paraxial approximation. It uses paraxial scalar wave equation to derive the expressions for Hermite-Gauss and Laguerre-Gauss beams. Problems with the scalar solution for describing laser beams are then pointed out motivating the search for a correct description. This search begins by assuming a three-component electric field and linear polarization (one dominant component). Maxwell's equations are then solved with this assumption in both Cartesian and circular cylindrical coordinates giving the three components of linearly polarized Hermite-Gauss and Laguerre-Gauss beams, respectively. Only the electric components are explicitly given. The components of the magnetic associated with these beams can be calculated using the Maxwell's equations.

In Chapter 3, we describe the generation of HG beams by an Ar-ion laser and experimental verifi-

cation of the polarization structure of HG beams. In particular, the transverse intensity distribution of the dominant and cross-polarization components of Hermite-Gauss beams of several orders were experimentally verified. Higher order HG beams are generated from an argon-ion laser by inserting a pair of crossed fibers into the laser cavity. By carefully placing the fibers relative to the axis of the laser cavity, we were able to generate several higher order HG modes. The output from the laser was passed through a pair of linear polarizers. Light transmitted by the polarizers was recorded by a CCD camera. It was found that unlike the intensity profiles of the dominant polarization component, the intensity profiles of the cross polarization component, for all but the fundamental mode, undergo an evolution with propagation. Experimentally recorded HG beam profiles were found to be in agreement with the theoretically calculated profiles both in shape and in their evolution with propagation.

Chapter 4 describes experiments with Laguerre-Gauss beam similar to those carried out with HG beams. Different order LG beams were generated by converting HG beams of the same order from the laser, via a pair of identical cylindrical lenses separated by a distance equal to $\sqrt{2}$ times the focal length (astigmatic mode converter). This allows us to manipulate the Guoy's phase of incident HG beams turning them into LG modes. The LG cross-polarization component was found to have the interesting property that the intensity profile has noticeable rotation with propagation over a distance of few Rayleigh ranges. The rotation of the intensity profile for beams with opposite topological charge ℓ is in opposite directions. The size, shape, and degree of rotation of the experimental and theoretical cross-polarization component of LG beams are all directly comparable and are in reasonable agreement within the error associated with mode generation and image capture. Finally, we mention that although the experiments confirmed the detailed beam intensity profiles and their evolution with propagation away from the waist predicted by the theory, the power carried by the cross-polarization component was measured to be substantially higher than predicted by the theory. This discrepancy is not fully understood and merits further study of the polarization and spectral content of laser background fluorescence and spectral response of the polarizer itself.

5.2 Future work

An immediately applicable use of knowing the structure of the cross-polarization component of Laguerre-Gaussian beams is to determine the radial index p and azimuthal index ℓ , also known as the topological charge of the beam. A determination of these indices, especially of the azimuthal index, requires a Mach Zehnder type of interferometer, which can be a laborious undertaking [15]. Our work suggests a method for determining these indices. The value of the index p is readily determined by counting the number of rings present in the intensity profile of the dominant component in an LG beam ($p - 1 = \text{number of rings}$). Determining the value and sign of ℓ is not as straightforward. The intensity profiles of LG beams with the same p value but different ℓ values appear similar. Since the direction of rotation of the cross-polarization intensity profiles with propagation for different charges is in opposite directions, observation of the cross-polarization intensity profiles near the waist immediately gives the sign of charge of the beam. Since the rate of rotation of the cross-polarization intensity pattern is different for different azimuthal orders of LG beams, analysis of the rate of rotation of the cross-polarization intensity profiles can give the order of the beam. In practice, this is likely to work for low values of ℓ .

There are several related investigations, which would be interesting to carry out. In the experiments described here only the dominant and cross-polarization components of laser beams were observed. Observation of the longitudinal-polarization component of the field was beyond the scope of available instrumentation for this project. Longitudinal component of a laser plays an important role in particle accelerators based on focused laser beams. There have been a number of investigations of the longitudinal component using nano structures [24, 71, 81]. By appropriately orienting a collection of nano-crystals, their response can be tailored to respond to a particular polarization component. This has been used to record the spatial profile of the longitudinal component of a focused laser beam. A knowledge of the longitudinal component of laser beam is useful in laser tweezers where highly focused laser beams with spot size comparable to laser wavelength

are used [16,68]. Since the strength of longitudinal component relative to the dominant component is of order $(\lambda/w_o)^2$ [12], the longitudinal components will be a significant presence in such applications. Other applications involving highly focused beam include confocal and super resolution microscopy.

In this thesis we have confined our attention to linearly polarized beams. It would be of interest to investigate other states of polarizations such as circular, radial, and azimuthal polarizations. There are no straight forward methods to directly observe these states of polarization or the corresponding cross-polarization components analogous to those used in this thesis to observe the dominant and cross-polarization component of linearly polarized beams. Determining a method to experimentally investigate the dominant as well cross-polarization component of other states of polarizations directly is an open and intriguing problem.

Investigations similar to those described in this thesis can also be extended to other types of beams. In addition to Cartesian and circular cylindrical coordinates, the paraxial wave equation has separable transverse beam profiles in parabolic and elliptical cylindrical coordinates. These beams have been discussed in the paraxial approximation [54]. Description of these beams consistent with Maxwell's equations for different polarizations would add to the diversity of beam like solutions of Maxwell's equation. In addition to the theoretical description, new methods for generating these beams would also be of interest from an application point of view. We have used an astigmatic mode converter for transforming HG beams into LG beams and mentioned the use of holography and spatial light modulators (SLMs). Other methods to generate these modes directly in a laser could be explored. Such methods have the potential for generating higher powers and better beam quality as both the holographic and SLM methods are limited by power and efficiency considerations [63,64]. For example, due to its potential simplicity, an attractive option for LG beam generation is to insert an opaque spot in the laser cavity that would act similar to the fibers used in HG beam generation. The non-transparent spot would force the laser to operate in a higher order LG mode with a dark center to minimize losses. This has the same principle as the previously

reported method of using laser cavity mirrors with a spot defect [66] but has the advantage of not destroying costly mirrors. A key difference of LG modes generated in this way compared to ones generated via the AMC is that the output of the laser will be an interference pattern of the plus and minus topological charge ($\pm\ell$). Polarization and propagation investigations on these beams should also prove fascinating. Furthermore, with minor modifications, the experimental setup used to investigate polarization properties of linearly polarized LG beams similar properties of Ince-Gauss beams could also be investigated [43]. Other types of laser beams should similarly be researched.

Polarization, like phase, is an intrinsic property of electromagnetic waves. Evolution of phase in propagation is well known and is what is normally emphasized. Indeed in free-space propagation of laser beams we assume that polarization remains unchanged and we rarely talk about the evolution of polarization. This in fact is the basis of scalar description. Our investigations demonstrate that like phase, polarization can and does evolve even in free-space. Without this complete description the outcome of a simple experiment involving crossed-linear polarization cannot be correctly predicted. A description of laser beams consistent with Maxwell's equations has practical implications too. Non-uniform polarization and its variation in propagation will be specially important in the focal region. In applications of laser beams that involve highly focused beams such as microscopy, optical tweezers, and nonlinear optics, therefore, a careful analysis of polarization and its evolution may reveal novel phenomena.

Bibliography

- [1] M. Lax, W. H. Louisell, and W. B. McKnight, *Phys. Rev. A* **11**, 1365–1370 (1975)
- [2] L. W. Davis, *Phys. Rev. A* **19**, 1177–1179 (1979).
- [3] L. W. Davis and G. Patsakos, *Opt. Lett.* **6**, 22–23 Jan (1981).
- [4] G. P. Agrawal and D. N. Pattanayak, *J. Opt. Soc. Am.* **69**, 575–578 (1979).
- [5] M. Couture and P. Belanger, *Phys. Rev. A* **24**, 355–359 (1981).
- [6] G. P. Agrawal, and M. Lax, *Phys. Rev. A* **27**, 1693–1695 (1983).
- [7] R. Simon, E. C. G. Sudarshan, and N. Mukunda, *Appl. Opt.* **26**, 1589–1593 May (1987).
- [8] , N. Mukunda, R. Simon, and E. C. G. Sudarshan, *Phys. Rev. A* **28**, 2933–2942 (1983).
- [9] L. W. Davis, *Phys. Rev. A* **30**, 3092–3096 (1984).
- [10] L. Cicchitelli, H. Hora, and R. Postle, *Phys. Rev. A* **41**, 3727–3732 (1990).
- [11] D. G. Hall, *Opt. Lett.* **21**, 9–11 (1996).
- [12] W. L. Erikson, and S. Singh, *Phys. Rev. E* **49**, 5778–5786 (1994).
- [13] J. Conry, R. Vyas, and S. Singh, *J. Opt. Soc. Am. A* **29**, 579–584 Apr (2012).
- [14] J. Conry, R. Vyas, and S. Singh, Submitted for publication (2012).
- [15] J. Vickers, M. Burch, R. Vyas, and S. Singh, *J. Opt. Soc. Am. A* **25**, 823–827 (2008).
- [16] S. H. Simpson, and S. Hanna, *J. Opt. Soc. Am. A* **26**, 625–638 (2009).
- [17] Z. Guo-Quan, C. Liang, and C. Xiu-Xiang, *Chin. Phys* **16**, 2709–2715 (2007).

- [18] H.-C. Kim and Y. H. Lee, *Optics Commun.* **169**, 9–16 (1999).
- [19] J. X. Wang, W. Scheid, M. Hoelss, and Y. K. Ho, *Phys. Rev. E* **64**, 066612–066618 (2001).
- [20] A. Cerjan and C. J. Cerjan, *Opt. Soc. Am. A* **28**, 2253–2260 (2011).
- [21] E. J. Bochove, G. T. Moore, and M. O. Scully, *Phys. Rev. A* **46**, 6640–6653 (1992).
- [22] C. Varin, M. Piché, and M. A. Porrás, *Phys. Rev. E* **71**, 26603–26613 (2005).
- [23] Z. Zhi-Guo and L. Bai-Da, *Chin. Phys* **15**, 1022–1027 (2006).
- [24] M. O. Scully and M. S. Zubairy, *Phys. Rev. A* **44**, 2656–2663 (1991).
- [25] E. Esarey, P. Sprangle, and J. Krall, *Phys. Rev. E* **52**, 5443–5453 (1995).
- [26] M. O. Scully, *Appl. Phys. B.* **51**, 238–241 (1990).
- [27] E. J. Bochove, G. T. Moore, and M. O. Scully, *Phys. Rev. A* **46**, 6640–6653 (1992).
- [28] W. D. Kimura, G. H. Kim, R. D. Romea, L. C. Steinhauer, I. V. Pogorelsky, K. P. Kusche, R. C. Fernow, X. Wang, and Y. Liu, *Phys. Rev. Lett.* **74**, 546–549 (1995).
- [29] A. Bahari, and H. Shahriari, *Phys. Scr.* **81**, 035403–035408 (2010).
- [30] J. H. Poynting, *Proceedings of the Royal Society of London. Series A, Containing Papers of a Mathematical and Physical Character* **82**, pp. 560–567 (1909).
- [31] R. A. Beth, *Phys. Rev.* **50**, 115–125 (1936).
- [32] M. W. Beijersbergen, L. Allen, H. E. L. O. van der Veen, and J. P. Woerdman, *Optics Commun.* **96**, 123–132 (1993).
- [33] A. Aiello, C. Marquardt, and G. Leuchs, *Phys. Rev. A* **81**, 53838–52847 (2010).
- [34] M. Padgett, J. Courtial, and L. Allen, *Phys. Today* **57**, 35–40 (2004).
- [35] G. Gibson, J. Courtial, M. Padgett, M. Vasnetsov, V. Pas’ko, S. Barnett, and S. Franke-Arnold, *Opt. Express* **12**, 5448–5456 (2004).
- [36] R. Kompfner, *Appl. Opt.* **11**, 2412–2425 (1972).
- [37] A. Mair, A. Vaziri, G. Weihs, and A. Zeilinger, *Nature* **412**, 313–316 (2001).
- [38] S. Franke-Arnold, L. Allen, and M. Padgett *Laser and Photon. Rev.* **2**, 299–313 (2008).

- [39] S. A. Kennedy, M. J. Szabo, H. Teslow, J. Z. Porterfield, and E. R. I. Abraham, *Phys. Rev. A* **66**, 043801 (2002).
- [40] D. Grier, *Nature* **424**, 21–27 (2003).
- [41] T. Meyrath, F. Schreck, J. Hanssen, C. Chuu, and M. Raizen, *Opt. Express* **13**, 2843–2851 (2005).
- [42] N. B. Simpson, D. McGloin, K. Dholakia, L. Allen, and M. J. Padgett, *J. Mod. Opt.* **45**, 1943–1949 (1998).
- [43] T. Ohtomo, S.-C. Chu, and K. Otsuka, *Opt. Express* **16**, 5082–5094 (2008).
- [44] H. He, M. E. J. Friese, N. R. Heckenberg, and H. Rubinsztein-Dunlop, *Phys. Rev. Lett.* **75**, 826–829 (1995).
- [45] A. E. Siegman, *Lasers*. University Science Books, Sausalito California, (1986).
- [46] H. Kogelnik, and Li T., *Appl. Opt.* **5**, 1550–1567 (1966).
- [47] E. G. Abramochkin and V. G. Volostnikov, *J. Opt. A: Pure Appl. Opt.* **6**, S157–S161 (2004).
- [48] E. G. Abramochkin, and V. Volostnikov, *Phys. Wave Phenom.* **18**, 14–22 (2010).
- [49] E. G. Abramochkin, and V. Volostnikov, *Optics Commun.* **102**, 336 – 350 (1993).
- [50] E. G. Abramochkin, and V. Volostnikov, V. G. *Physics-Uspeski* **47**, 1177–1203 (2004).
- [51] M. A. Bandres, and J. C. Guti´errez-Vega, *Opt. Express* **15**, 16719–16728 (2007).
- [52] G. A. Siviloglou, and D. N. Christodoulides, *Opt. Lett.* **32**, 979–981 (2007).
- [53] E. Karimi, G. Zito, B. Piccirillo, L. Marrucci, and E. Santamato, *Opt. Lett.* **32**, 3053–3055 (2007).
- [54] M. A. Bandres and J. Guti´errez-Vega, *Opt. Lett.* **29**, 144–146 (2004).
- [55] M. A. Bandres and J. C. Guti´errez-Vega *J. Opt. Soc. Am. A* **21**, 873–880 (2004).
- [56] U. T. Schwarz, M. A. Bandres and J. C. Guti´errez-Vega *Opt. Lett.* **29**, 1870–1872 (2004).

- [57] K.Otsuka, K. Nemoto, K. Kamikariya, Y. Miyasaka, and S.-C. Chu, *Jpn. J. Appl. Phys.* **46**, 5865–5867 (2007).
- [58] E. J. Galvez, P. R. Crawford, H. I. Sztul, M. J. Pysher, P. J. Haglin, and R. E. Williams, *Phys. Rev. Lett.* **90**, 203901–203905 (2003).
- [59] A. T. O’Neil and J. Courtial, *Optics Commun.* **181**, 35–45 (2000).
- [60] L. Allen, J. Courtial, M. J. Padgett, *Phys. Rev. E* **60**, 7497–7503 (1999).
- [61] N. R. Heckenberg, R. McDuff, C. P. Smith, and A. G. White, *Opt. Lett.* **17**, 221–223 (1992).
- [62] M. Clifford, J. Arlt, J. Courtial, and K. Dholakia, *Optics Commun.* **156**, 300–306 (1998).
- [63] N. Matsumoto, T. Ando, T. Inoue, Y. Ohtake, N. Fukuchi, and T. Hara, *J. Opt. Soc. Am. A* **25**, 1642–1651 (2008).
- [64] Y. Ohtake, T. Ando, N. Fukuchi, N. Matsumoto, H. Ito, and T. Hara, *Opt. Lett.* **32**, 1411–413 (2007).
- [65] J. Courtial, and M. Padgett, *Optics Commun.* **159**, 13–16 (1999).
- [66] A. Ito, Y. Kozawa, and S. Sato, *J Opt. Soc. Am. A* **27**, 2072–2077 (2010).
- [67] K. Kano, Y. Kozawa, and S. Sato, *Int. J. Optics* **2012**, 221–223 (2012).
- [68] B. Sick, B. Hecht, and L. Novotny, *Phys. Rev. Lett.* **85**, 4482–4485 (2000).
- [69] A. Bouhelier, M. R. Beversluis, and L. Novotny, *Appl. Phys. Lett.* **82**, 4596–4599 (2003).
- [70] B. Hao and J. Leger, *Opt. Express* **15**, 3550–3556 (2007).
- [71] L. Novotny, M. R. Beversluis, K. S. Youngworth, and T. G. Brown, *Phys. Rev. Lett.* **86**, 5251–5254 (2001).
- [72] R. Vyas. and S. Singh, In *Conference on Coherence and Quantum Optics IX*, Bigelow, N. P., Eberly, J. H., and Stroud, C. R., editors, 344–345 (AIP, New York, 2008).
- [73] M. Abramowitz and I. A. Stegun, *Handbook of Mathematical Functions with Formulas, Graphs, and Mathematical Tables*. Dover, New York, ninth Dover printing edition, (1964).
- [74] S. Feng and H. G. Winful, *Opt. Lett.* **26**, 485 (2001).
- [75] R. Vyas and S. Singh, In *Frontiers in Optics*, FWT3. Optical Society of America, (2005).
- [76] A. G. Fox and T. Li, *Bell Sys, Tech. J.* **40**, 452–458 (2003).

- [77] E. Abramochkin and V. Volostnikov, *Optics Commun.* **83**, 123–135 (1991).
- [78] I. Kimel and L. Elias, *IEEE Journal of Quantum Electronics* **29**, 2562–2567 (1993).
- [79] M. Padgett, J. Arlt, N. Simpson, and L. Allen., *Am. J. Phys.* **64**, 77–82 (1996).
- [80] D. V. Petrov, F. Canal, and L. Torner, *Optics Commun.* **143**, 265–267 (1997).
- [81] Y. Kozawa and S. Sato, *J. Opt. Soc. Am. B* **25**, 175–179 (2008).

Appendix A

subtract.m

```
%Name:    Jessica Conry
%Prog. Name:  SUBTRACT
%Date: 2-14-12
%Notes:
%Use: Rescales intensity and size of an image (with even index) to
%that of another image (stored with an odd index), finds the
%difference of the two and saves the result as a new image.
clear;                % clear variables form memory
clf;
% Initialize Variables
n=10;                % n is the total number of images
filename = {zeros(n,1)}; % empty filename vector (strings)
MinPerMat = zeros(n/2,1); %
MaxPerMat= zeros(n/2,1);

% Read Data In and Processing
for i=1:1:n
    i
    filename(i,1) = {[ num2str(i) '.png']};
    % loop creates filenames for images
    I_i = imread(cell2mat(filename(i,1)));
    % fill vector images with filenames

    imcrop(I_i) % Select crop area in figure, select "copy location"
    % then "crop", first crop selects a general region of interest
    reply = input('Crop Boundaries?');
    %paste crop area and location at prompt
M=reply;
I_i=imcrop(I_i,M);% save cropped image
J=imshow(I_i); %shows cropped image
attrs = imattributes(J)% shows the attributes of the cropped image
MaxI = input('Max Intensity?');
    % input the max intensity from the attribute output
MinI = input('Min Intensity?');
    %input the min intensity from the attribute output
```

```

MinPer= MinI/252; %finds the percentage of 252 of the min intensity
MaxPer = MaxI/252; %finds the percentage of 252 of the max intensity
v= (MinPer+MaxPer)/2 ;
    %calculates the threshold to be used in converting the image to
    binary
bw=im2bw(I_i,v);
    %converts image to binary with the above calculated threshold
imshow(bw);
if mod(i,2)==1
    % for odd i, The experimental images are saved
    %with odd numbered indexes
    m=(i+1)/2;
    MaxPerMat(m,1) = MaxPer;
    MinPerMat(m,1) = MinPer;
end
reply =input('Threshold ok? [1=yes, 2=more, 3=less]');
    % ask if the threshold is ok or if it should be more or less
E= reply;
if (E==1)
%if the threshold of the binary image is satisfactory then enter '1'
    v= (MinPer+MaxPer)/2 ;
    bw=im2bw(I_i,v);
elseif (E==2)
    % If the threshold is too low then enter '2', will start loop
    %to get a satisfactory threshold
    while(E==2)
        reply=input('How much do you want to change? [0..0.1]');
        t=reply;
        v= (MinPer+MaxPer)/2-t ;
        bw=im2bw(I_i,v);
        imshow(bw)
        reply =input('Threshold ok? [1=yes, 2=more, 3=less]');
        %ask if the threshold is ok or if it should be more or less
E= reply;
        end
elseif (E==3) % If the threshold is too high then enter '3', will
                % start loop to get a satisfactory threshold
    while (E==3)
        reply=input('How much do you want to change? [0..0.1]');
        t=reply;
        v= (MinPer+MaxPer)/2+t ;
        bw=im2bw(I_i,v);
        imshow(bw)
        reply =input('Threshold ok? [1=yes, 2=more, 3=less]');
        %ask if the threshold is ok or if it should be more or less

```

```

E= reply;
    end
end

bw1= edge(bw);%finds edges of the binary image
[r,c]=find(bw1);
fun=[r,c];
allx=fun(:,2);
ally=fun(:,1);
minx= min(allx); % smallest x pixel location for a '1' in image
maxx= max(allx); % largest x pixel location for a '1' in image
miny= min(ally);% smallest y pixel location for a '1' in image
maxy=max(ally); % Largest y pixel location for a '1' in image
width=maxx-minx; %width of image
length=maxy-miny; % lenght of image
bw=imcrop(bw, [minx miny width length]);
    %crops edge of binary image
I_i=imcrop(I_i, [minx miny width length]);
    % Crops the original image with the same boundaries
    % as the binary image
if mod(i,2)==1
A_i=size(I_i); %finds size of the experimental image
x_i=A_i(1);
y_i=A_i(2);
end

if mod(i,2)==1 %if i is odd
imwrite(I_i,['Io' num2str(i) '.bmp']); %rename image
else
    I_i = rgb2gray(I_i);
    I_i=imresize(I_i, [x_i y_i]);
    %resizes the even indexed images (theory)
p=i/2;
I_i = imadjust(I_i,[0 1],[MinPerMat(p,1) MaxPerMat(p,1)]);
imwrite(I_i, ['Ie' num2str(i) '.bmp']);
    %adjust theoretical image to have same intensity range as the
    %experimental images
end

    if mod(i,2)==1
        Io= imread(['Io' num2str(i) '.bmp']);
            %rename experimental images
            eval(['Io_' num2str(i) '=Io;']);
        else
            Ie= imread(['Ie' num2str(i) '.bmp']);

```

```

        % rename scaled and intensity adjusted theoretical images
        eval(['Ie_' num2str(i) '=Ie;']);

end

end

for i=1:2:n
    eval(['Io = Io_' num2str(i)]);
    s=i+1;
    eval(['Ie = Ie_' num2str(s)]);
    IS=Io-Ie; % Subtract theory and experiment
    imwrite(IS, ['Is' num2str(i) '.bmp']);
    %saves the difference of exp and theory image as ISi.bmp
end

```

Appendix B

figureofmerit.m

```
%Name: Jessica Conry
%Prog. Name: LG rotation
%Date: 2-16-12
%
%
%
%Notes:
%
%
%Use: Calculates figure of merit of experemental images
%
clf; %clear functions
clear; % Initialize Variables%
n=10; %n is the total number of images
filename1 = {zeros(n,1)}; % empty filename vector (strings)
filename2 = {zeros(n,1)};
SUM=zeros(n/2,1);
for i=1:2:n
    filename1(i,1) = {[ 'Is' num2str(i) '.bmp' ]};
    % loop creates filenames for images
    I1 = imread(cell2mat(filename1(i,1)));
    filename2(i,1) = {[ 'Io' num2str(i) '.bmp' ]};
    % loop creates filenames for images
    I2 = imread(cell2mat(filename2(i,1)));

    m1=max(max(I1)); % Finds max pixel intensity of difference image
    size2=size(I2); % Size of excremental image
    m2=max(max(I2)); % Finds max pixel intensity of experimental image
    TotPix= size2(1)*size2(2); % total number of pixels in the
                                %experimental image

    NumPix= zeros(m1,1);
    %vector filled with same number of elements as
    % the max pixel value in the experimental image
    NumPixScale= zeros(m1,1);
    PixVal=zeros(m1,1);
    RelPix=zeros(m1,1);
```

```

for t=1:m1
    PixVal(t,:)=t;
    % vector with integers 1 through max pixel value
end

%this for loop counts how many of each pixel values there
% are in difference image
for q=1:m1
    l=find(I1==q);
    [r,c] = size(l);
    NumPix(q,:)=r;

end
NumPixscale=NumPix./TotPix;
    %scales pixel values with total number of pixels
MAX=double(m2);
RelPix=PixVal./MAX;
    % scales value of pixel with the max pixel value
Total=NumPixscale.*RelPix;
p=(i+1)/2;
SUM(p,1)=sum(Total); %Figure of merit

xlswrite('dataanaly.xls',NumPix,'A2');
    %writes data in exel file

end

```


Appendix C

LGrot.m

```
%Name:    Jessica Conry
%Prog. Name:  LG rotation
%Date: 8-30-11
%
%
%
%Notes:
%
%
%Use:    Takes experimental or theoretical the cross-polarization
%component of linearly polarized Laguerre-Gauss laser beam profile
%images, finds the angle from the center of the profile and the
%center of each of the lobes of the profile.
%

clear;           % clear variables form memory
clf;             % clear figures
clc;             % clear command window
workspace;      % display workspace window

% Constants
%bmpext = '.ext';           % .bmp extension string

% Initialize Variables
n=5;                      %n is the total number of images
filename = {zeros(n,1)};  % empty filename vector (strings)
theta = zeros(n,1);
thetad = zeros(n,1);
thetad2 = zeros(n,1);
thetad3 = zeros(n,1);
thetad4 = zeros(n,1);
centroidlist = zeros(n,1);
center= zeros(n,2);
```

```

centroidslist=zeros(4,2*n);

% Read Data In and Processing
for i=1:1:n
    i
    filename(i,1) = {[ num2str(i) '.jpg']};
    % loop creates filenames for images
    I_i = imread(cell2mat(filename(i,1)));
    % fill vector images with filenames

imcrop(I_i)
    % Select crop area in figure, select "copy location" then "crop"
    reply = input('Crop Boundaries?'); %paste location at prompt
    M=reply;
    I_i=imcrop(I_i,M);% save cropped image
    J=imshow(I_i);
    attrs = imattributes(J)
    % shows the attributes of the cropped image
    MaxI = input('Max Intensity?');
    % input the max intensity from the attribute output
    MinI = input('Min Intensity?');
    %input the min intensity from the attribute output
    MinPer= MinI/255;
    %finds the percentage of 255 of the min intensity
    MaxPer = MaxI/255;
    %finds the percentage of 255 of the max intensity
    v= (MinPer+MaxPer)/2 ;
    %calculates the threshold to be used in
    %converting the image to binary
    bw=im2bw(I_i,v);
    %converts image to binary with the above calculated threshold
    imshow(bw)
    reply =input('Threshold ok? [1=yes, 2=more, 3=less]');
    %ask if the threshold is ok or if it should be more or less
    E= reply;
    if (E==1)
        v= (MinPer+MaxPer)/2 ;
        bw=im2bw(I_i,v);
    elseif (E==2)
        while(E==2)
            reply=input('How much do you want to change? [0..0.1]');
            t=reply;
            v= (MinPer+MaxPer)/2-t ;
            bw=im2bw(I_i,v);
            imshow(bw)

```

```

        reply =input('Threshold ok? [1=yes, 2=more, 3=less]');
        %ask if the threshold is ok or if it should be more or less
E= reply;
    end
elseif (E==3)
    while (E==3)
        reply=input('How much do you want to change? [0..0.1]');
        t=reply;
        v= (MinPer+MaxPer)/2+t ;
        bw=im2bw(I_i,v);
        imshow(bw)
        reply =input('Threshold ok? [1=yes, 2=more, 3=less]');
        %ask if the threshold is ok or if it should be more or less
E= reply;
    end
end

bw1= edge(bw);%finds edges of the binary image
[r,c]=find(bw1);
fun=[r,c];
allx=fun(:,2);
ally=fun(:,1);
minx= min(allx);
maxx= max(allx);
miny= min(ally);
maxy=max(ally);
width=maxx-minx;
length=maxy-miny;
bw=imcrop(bw, [minx miny width length]);
I_i=imcrop(I_i, [minx miny width length]);
    %bw=im2bw(I); %%converts grey scale image to bianary

s= regionprops(bw,'centroid');
    %finds the center of each bright spot (the "blades")
    %and the center of the image
centroids_i= cat(1,s.Centroid);
    %gives vetors describing the the location of the centers
%locate the center
[y,x,planes]= size(bw);
%gives number of pixels in the x and y directions
nx= x/2; %gives the center pixel in x direction
ny= y/2 ; % gives the center pixel in the y direction
%[min_diff, array_pos]=min(abs(nx-centroids(:,1)));
%gives the array position of the centroid in the middle
center_i=[nx, ny]; % gives the location of the center

```

```

    center(i,:)= center_i;
    %find the upper left centroid
    [L,W] = size(centroids_i);
    [q,p]=size(centroids_i);
    clear x1 %initializing variables
    clear y1 %initializing variables
    %for loop finds the upper left centroid
    centx=centroids_i(:,1);
    %writes all of the x coordinates of the centroid to centx
    minx=min(centx); % finds minimum x coordinate
    centy=centroids_i(:,2);
    %writes all of the y coordinates of the centroid to centy
    miny=min(centy); % finds minimum y coordinate
    maxx=max(centx); % finds maximum x coordinate
    maxy=max(centy); % finds maximum y coordinate
    centroidslist(1:q,2*i-1)=centx;
    centroidslist(1:q,2*i)=centy;
    for k=1:L
        if (centroidslist(k,2*i-1) == minx)
            x1 = centroidslist(k,2*i-1);
            %x1 is the x coordinate of the most left lobe
            y1 = centroidslist(k,2*i);
        end
    end
    for k=1:L
        if (centroidslist(k,2*i) == miny)
            x2 = centroidslist(k,2*i-1);
            y2 = centroidslist(k,2*i);
            %y2 is the y coordinate of the uppermost lobe
        end
    end
    for k=1:L
        if (centroidslist(k,2*i-1) == maxx)
            x3 = centroidslist(k,2*i-1);
            %x3 is the x coordinate of the right most lobe
            y3 = centroidslist(k,2*i);
        end
    end
    for k=1:L
        if (centroids_i(k,2) == maxy)
            x4 = centroids_i(k,1);
            y4 = centroids_i(k,2);
            % y4 is the y coordinate of the lobe
            %closest to the bottom of the figure
        end
    end

```

```

end

a1=abs(y1-center(i,2));
%gives the length of the "opposite" side of the triangle
a2=abs(x1-center(i,1));
% gives the length of the "adjacent" side of the triangle
theta(i)= atan(a1/a2);
% gives angle of the upper left lobe from
% the center of the image.
thetad(i)= radtodeg(theta(i));
% converts angle to degrees.

a3=abs(center(i,2)-y2);
a4=abs(x2-center(i,1));
theta2(i)= atan(a3/a4);
% gives angle of the upper right lobe from
% the center of the image.
thetad2(i)= radtodeg(theta2(i));
%converts angle to degrees.
a5=abs(y3-center(i,2));
a6=abs(x3-center(i,1));
theta3(i)= atan(a5/a6);
% gives angle of the lower left lobe from the
%center of the image.
thetad3(i)= radtodeg(theta3(i));
% converts angle to degrees.

a7=abs(y4-center(i,2));
a8=abs(x4-center(i,1));
theta4(i)= atan(a7/a8);
% gives angle of the upper left lobe from the center
%of the image.
thetad4(i)= radtodeg(theta4(i)); % converts angle to degrees.

imwrite(I_i, [ 'LG20y' num2str(i) 'crop.bmp' ]);
%writes image I_i to file NOTE change file name
%for different orders!
imwrite(bw, [ 'LG20y' num2str(i) 'cropbw.bmp' ]);
close all

end

%the Following plots all cropped images on one figure with blue
%stars indicating the centroids used and red stars on the center
%of the image. Note subplot(n,m,i) gives the number of rows and

```

```

%columns of images... this can be changed according to how many
%images there are.
for i=1:2:n
I_i=imread([ 'LG20y' num2str(i) 'crop.bmp']);
subplot(6,6,i)
    subimage(I_i)
    hold on
        plot(centroidslist(:,2*i-1), centroidslist(:,2*i), 'b*');
        %plots the centroids on the original image.;
        plot(center(i,1), center(i,2), 'r*')
        axis off
        hold off

end
figure
for i=1:2:n
bw_i=imread([ 'LG20y' num2str(i) 'cropbw.bmp']);
subplot(6,6,i)
    subimage(bw_i)
    hold on
        plot(centroidslist(:,2*i-1), centroidslist(:,2*i), 'b*');
        %plots the centroids on the original image.;
        plot(center(i,1), center(i,2), 'r*')
        axis off
        hold off

end

%Write data to excel files
xlswrite('data10a.xls',center,'center');
xlswrite('data10a.xls',centroidslist,'centroid');
xlswrite('data10a.xls',thetad,'theta','A1');
xlswrite('data10a.xls',thetad2,'theta','B1');
xlswrite('data10a.xls',thetad3,'theta','c1');
xlswrite('data10a.xls',thetad4,'theta','d1');

```